MAGNETO-OPTICAL PLASMONIC NANOSTRUCTURES AND DEVICES USING COMPOSITE MATERIALS

by

HOANG MAI LUONG

(Under the Direction of Tho Nguyen and Yiping Zhao)

ABSTRACT

Recently, extensive studies have been accomplished on investigating multifunctional materials and structures with both plasmonic and magnetic properties. For these materials and structures, external magnetic fields can be employed to actively control the optical responses of the systems, and vice versa, the plasmonic effect can be manipulated to optimize the magneto-optical (MO) performance. This kind of system is usually known as magneto-plasmonic (MOP) system and has been normally constructed by combining multi-layers of magnetic materials and noble metals. In this Dissertation, we investigate a novel MOP platform consisting of composite materials and nanostructures, with significantly tunable MOP performances in the visible and near infrared wavelength region.

Metal nano-lattices such as nano-hole arrays and nano-triangle arrays are prototypical plasmonic nanostructures. These two nano-lattices made from Ag-Co composite are created by using a combination of shadow nanosphere lithography and electron beam co-evaporation technique. A systematical study on their MOP properties shows strong MO constant dependences on the Co concentration, and both experimental and numerical results reveal that the MO responses of these MOP systems behave differently, depending

on the nature of the plasmon resonance that the system supports. By adjusting the Co content, their MOP performances can be maximized. It is also shown that by using non-normal vapor incident angles for metal co-evaporation, an active Ag-Co composite chiral nano-hole array with a plasmonic-enhanced intrinsic chirality and a large magnetic modulation amplitude can be achieved.

Finally, a $Pd_{80}Co_{20}$ composite nano-patchy particle array is developed to serve as a hydrogen gas sensor through MO signal readout. Such the Co content and sensor structure are chosen to remarkably increase the hydrogen sorption kinetics at the catalytic Pd sites, while the MO constant of the composite remains significantly strong. By incorporating with appropriate polymer coating, the sensing performances of this sensor platform can be further enhanced to surpass the state-of-the-art optical hydrogen sensors reported the literature, with a sub-0.5-second response time and ppb-level limit of detection. Notably, the results open a promising development of hydrogen based on MOP structures and composite materials such as ternary Ag-Pd-Co composite, with even more impressive sensing metrics.

INDEX WORDS: Plasmonics, Magneto-optics, Magneto-plasmonics, Faraday effect, Magneto-optical Kerr effect, Magnetic circular dichroism, Composite materials, Metal hydride, Hydrogen sensing

MAGNETO-OPTICAL PLASMONIC NANOSTRUCTURES AND DEVICES USING COMPOSITE MATERIALS

by

HOANG MAI LUONG

B.S., University of Science and Technology of Hanoi, Vietnam, 2014

M.S., École Normale Supérieure Paris-Saclay, France, 2016

A Dissertation Submitted to the Graduate Faculty of The University of Georgia in Partial Fulfillment of the Requirements for the Degree

DOCTOR OF PHILOSOPHY

ATHENS, GEORGIA

2021

MAGNETO-OPTICAL PLASMONIC NANOSTRUCTURES AND DEVICES USING COMPOSITE MATERIALS

by

HOANG MAI LUONG

Major Professor:	Tho Nguyen
	Yiping Zhao
Committee:	Yohannes Abate
	Susanne Ullrich

Electronic Version Approved:

Ron Walcott
Vice Provost for Graduate Education and Dean of the Graduate School
The University of Georgia
August 2021

DEDICATION

For my Grandparents.

ACKNOWLEDGEMENTS

Time has passed so quickly, and here I am at the end of my PhD journey. All of the works presented in this Dissertation cannot be accomplished without the supports from many wonderful individuals around me, and I would like to thank all of them.

First, I would like to thank Dr. Tho Nguyen, for several years of support, encouragement, and guidance. Thank you for all inspiring, amazing, but (ultra-) challenging research ideas that you have been sharing with me (sorry, I could only make a fraction of them worked!). You always encourage me to think outside-of-the-box and try out new research topics, and I will certainly take those mindsets with me. You have taught me how to handle the research problems and gave me plenty of freedom to think and to be creative. I am deeply grateful to be your graduate student.

I would like to thank Dr. Yiping Zhao, for his enormous dedications to students' development. Your work ethics, leadership, and management are so inspiring. Thank you for your valuable guidance, encouragement, and always being available to discuss about research no matter where and when. I am deeply appreciative for that.

I also would like to express my sincere gratitude to Dr. Yohannes Abate and Dr. Susanne Ullrich for spending their precious times serving on my advisory committee. I am deeply grateful to Dr. Inseok Song for his tremendous help on getting GRSA.

I am greatly indebted to Dr. Ngoc-Diep Lai and Dr. Manh-Huong Phan, for their recommendations, constant support and guidance in both science and everyday life. They have been inspiring me being a better scientist and a better human-being day-by-day.

Additionally, I would like to thank my past and present collaborators for their irreplaceable support. Thank you so much, Dr. George Larsen, for bringing me a chance to work in the hydrogen project. I owe a special thanks to several colleagues who train me on the research techniques: Dr. Kun Yao (cleanroom), Dr. Rugang Geng, Dr. Jagannath Devkota, Dr. Minh Pham (Nguyen's lab), Dr. Bin Ai, Dr. Steven Larson, Mr. Layne Bradley, Dr. Lu Zhu, Dr. Chunyuan Song (Zhao's lab), Dr. Eric Formo (GEM). Thank you, Dr. Tyler Guin and Dr. Richa Madhogaria, for helping with hydrogen sensor. Thank you all, Yanjun, Mona, Zilan, Yanfeng, Shasank, Jie, Ali, Neda, Dung, Huong, Tu Anh, Kevin, Marshall, Terry, Ying, Xingyang.

Finally, I would like to say thank to my family: Dad, Mom, and my Brother, for their unconditionally support, patience, love, and several years of moral and emotional encouragement. Thank you, Ked, for so many reasons. I could write them down as thick as this Dissertation.

TABLE OF CONTENTS

Page

LIST OF FIGURES

Page

CHAPTER 1

INTRODUCTION

1.1. Magneto-optical Effects – Discovery and Phenomena

1.1.1. Faraday Effect

In 1845, Michael Faraday discovered that when a plane-polarized light passed through a block of lead borosilicate glass in the direction parallel to the applied external magnetic field, the plane of incident was rotated.[1] The angle of rotation, θ, is proportional to the thickness of sample L, the magnitude of external field H, and an intrinsic coefficient of the materials, V, called Verdet constant (**Figure 1.1.**):

$$\theta = VHL \tag{1.1}$$

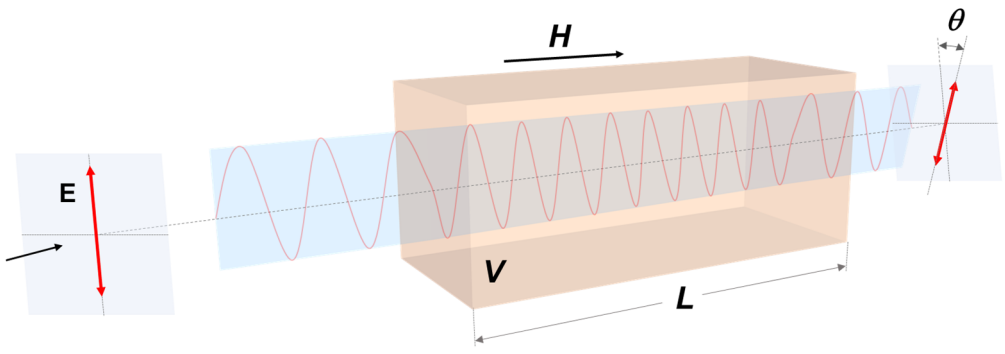

Figure 1.1. Polarization rotation due to the Faraday effect. Modified from Ref. [2].

The Faraday effect is originated by the circular anisotropy of the magnetized medium, *i.e.* the difference between the refractive indices ($\Delta n = n_+ - n_-$) of the medium under a right-handed circular polarized light σ^+(RCP, refractive index n_+) and a left-handed circular polarized light σ^- (LCP, refractive index n_-) .[3-5] Indeed, a linear polarized light that is seen to rotate in the Faraday effect can be treated as a superposition of $\sigma^\pm$ with the same amplitude. During the transmission through the transparent magnetic medium, these two modes $\sigma^\pm$ propagate with slightly different velocities of $\frac{c}{n_\pm}$, respectively (a property known as circular birefringence), resulting in a phase retardation between them at the exit. Consequently, the transmitted light has the polarization axis rotated by an angle θ as following,

$$\theta = \frac{\omega}{2c}(n_+ - n_-)L, \tag{1.2}$$

where ω is the angular frequency, c is the velocity of light. The rotated angle θ, so called Faraday rotation (FR), whose sign depends on the direction of *H, i.e.,* reflecting a rotated beam back through the same Faraday rotator would double the rotation instead of canceling the rotation.[4] This makes Faraday rotation an rare example of non-reciprocal optical rotation, which is unlike the rotation induced by natural optical activity of an optically active medium such as a sugar solution.[4]

1.1.2. Magneto-optic Kerr Effects

A few decades later than the discovery of Faraday effect, in 1877 a Scottish physicist John Kerr discovered an analogous phenomenon to the Faraday effect; however, this magneto-optics (MO) effect happens in the reflection mode. He observed that when a plane-polarized beam was reflected from a polished pole of an electromagnet, the polarization axis of reflected beam was rotated and the polarization became elliptically polarized.[4, 6] These phenomena later on became to be known as magneto-optical Kerr effect (MOKE). In practice, MOKE-based devices have been developed for many crucial applications such as magnetic imaging and data storage.[4, 7]

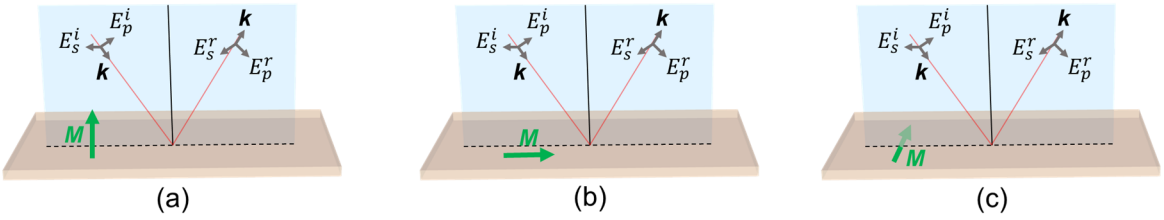

Figure 1.2. Three geometries for MOKE, showing the orientation of the magnetization vector ***M*** in respect of the plane of incident light: (a) PMOKE, (b) LMOKE, and TMOKE. Modified from Ref. [4].

Depending on the orientation of the magnetization vector ***M*** in respect of the plane of incident light, MOKE can be categorized into three different geometries: (i) polar-MOKE (PMOKE), where ***M*** is perpendicular to the reflective surface; (ii) longitudinal-MOKE (LMOKE), where ***M*** is parallel to both the plane of incident/reflected beams and the

reflection surface; and (iii) transverse-MOKE (TMOKE), where ***M*** is perpendicular to the plane of incident/reflected beams and parallel to the reflection surface (**Figure 1.2**).

1.1.3. Magnetic Circular Dichroism

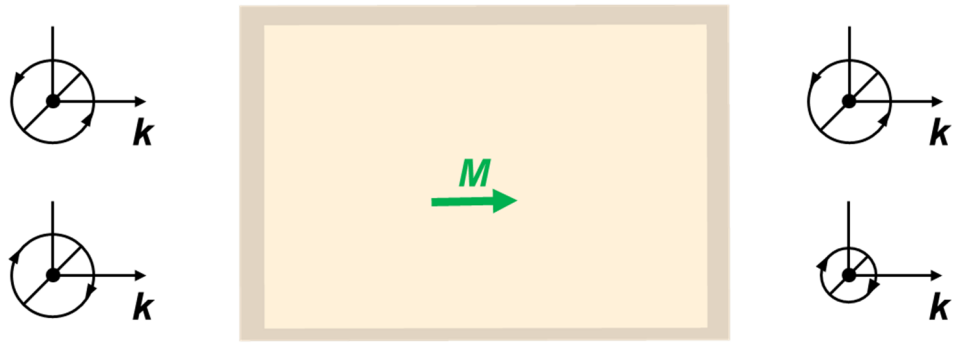

Figure 1.3. MO effect resulting from the magnetic circular dichroism (MCD). Modified from Ref. [4].

Similar to the Faraday effect, magnetic circular dichroism (MCD) is a MO effect that emerges in transmitted mode "Faraday geometry" where the light travels along the field direction. However, in contrast with the Faraday effect where $\sigma^{\pm}$ modes travel with different velocities due to the difference in refractive indices $n_{\pm}$, MCD is brought by the difference between the absorptions of medium ($\Delta k = k_{+} - k_{-}$) (**Figure 1.3**).[8] The difference absorption, or dichroism, is defined as,

$$\Delta A = A_{+} - A_{-}, \tag{1.3}$$

where A_+ and A_- are the RCP and LCP absorption, respectively. We note that the measured quantity ΔA of MCD is similar to that of natural circular dichroism (CD), which is the dichroism widely observed in chiral molecules or nanostructures.[8] However, their origins are quite different: while CD is induced by the molecular structure or nano-architecture that supports helical handedness, MCD is caused by the interaction between electronic charge and external magnetic field and no intrinsic chirality is required for MCD.[8] In addition, similar to Faraday effect, MCD is also a non-reciprocal MO effect, where the nature CD effect does not possess this characteristic.

1.2. The Optical Principles of MO Effects

Figure 1.4 shows a general picture of the MO effects, from the microscopic level (with initial electron band states, energy band splitting due external magnetic field, and the interaction between light and material) to the macroscopic level (with permittivity tensor and how they relate to the MO observables). In this Section, we will discuss throughout the microscopic origin of MO effects and macroscopic parameters of magnetic materials, their relations, and how these parameters can be extracted from the measured MO signals.

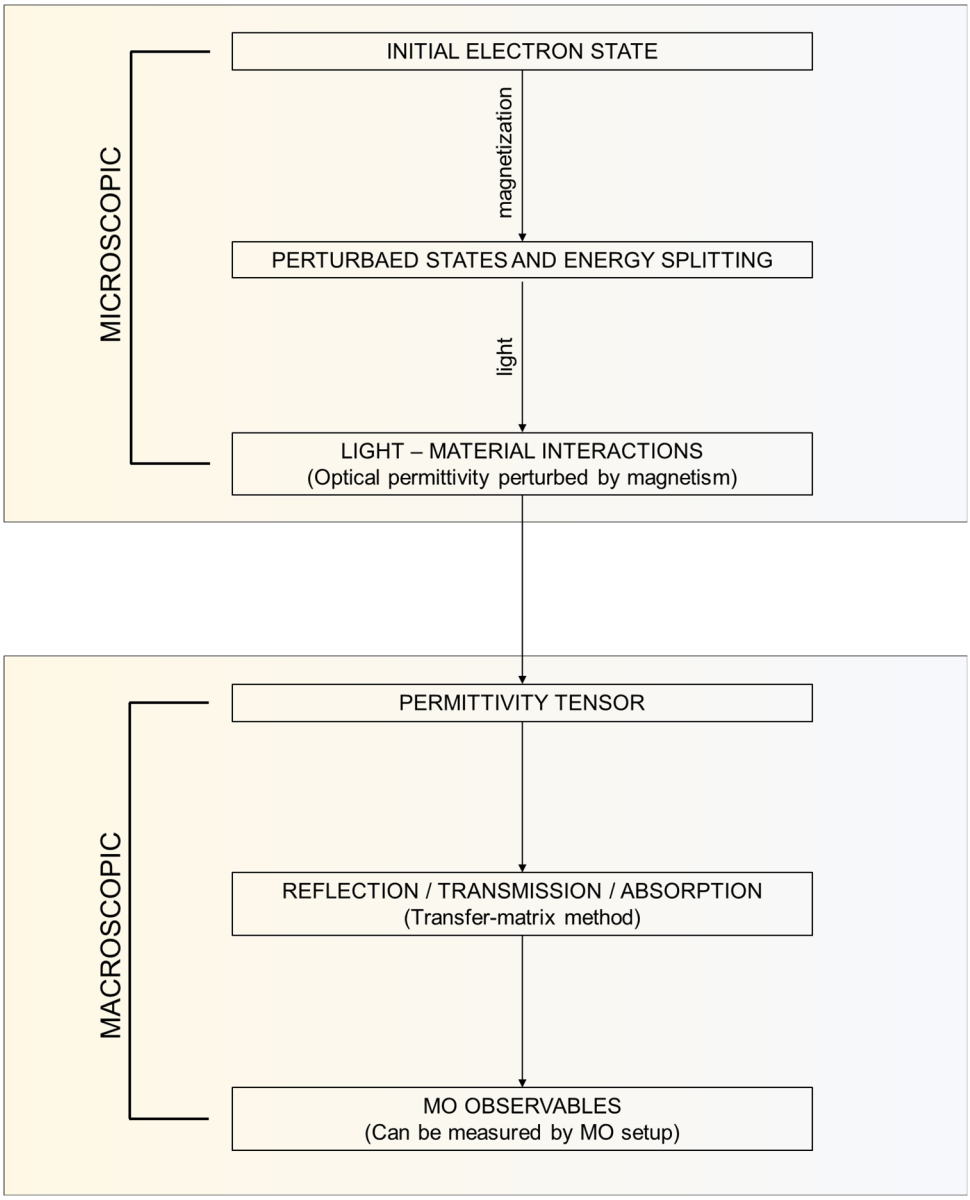

Figure 1.4. A schematic showing the relation between microscopic parameters, macroscopic parameters, and MO observables. Modified from Ref. [9].

1.2.1. Microscopic Origin of the MO Effects

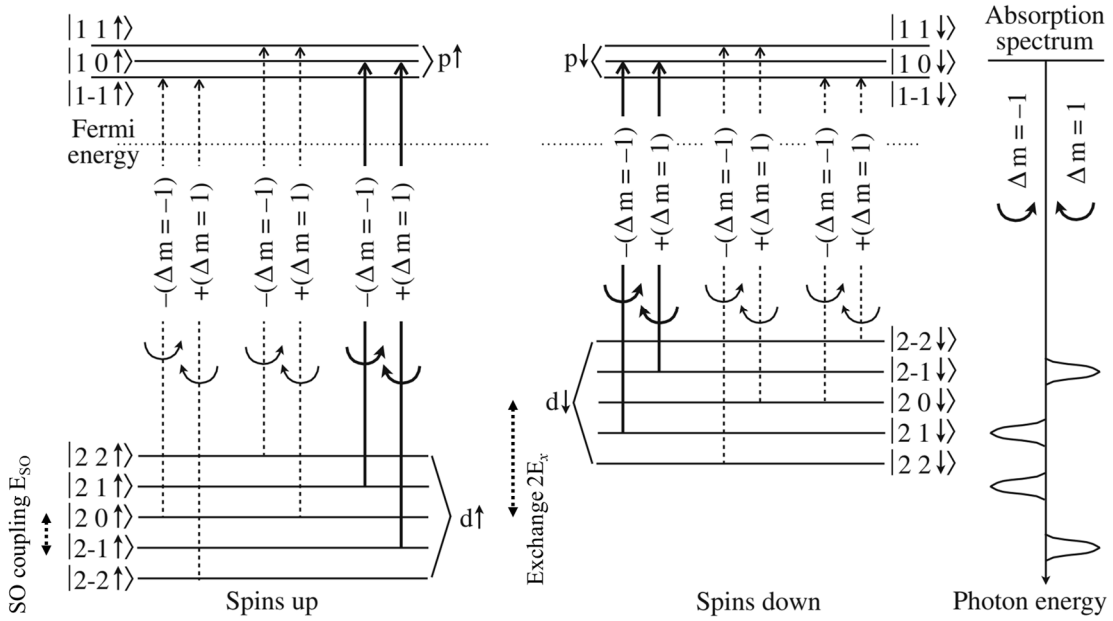

Figure 1.5. A schematic showing electronic structure of *p* and *d* states in a ferromagnetic solid, including exchange splitting of the occupied d states and spin–orbit splitting of *p* and *d* states. The labels $|\, l\ m \uparrow\rangle$ or $|\, l\ m \downarrow\rangle$ are the energy level based on the orbital quantum number, magnetic quantum number, and spins. Long vertical arrows denote dipole-allowed transitions for RCP light ($\Delta m = +1$) and LCP light ($\Delta m = -1$). The scheme on the right-hand side portrays absorption spectra for the transition from $|\, 2\ \pm 1 \uparrow\rangle$ states. Adapted from Ref. [9-10].

The microscopic origin of the MO effects can be followed back from optical transitions in the valence-band energy regime, for example, in *d* states of a bulk ferromagnet. In **Figure 1.5**, we present an explanation for the different absorption spectra for LCP and RCP light,

in a simplified case where the ferromagnet is magnetized in the Faraday configuration and normal incident light.[9-10] The initial states *d* and final states *p* are represented by horizontal lines, and they are denoted by nomenclature $| l\ m\ s >$ where *l*, *m*, and *s* are orbital quantum number, magnetic quantum number, and spins, respectively. We note that the energy levels for spin up (↑) and spin down (↓) in *d* states are separated by exchange splitting. On the other hand, spin-orbit splitting contributes to the smaller energy splitting due to the different *m*.

The $d \rightarrow p$ transitions denoted by vertical arrows in "spin up" and "spin down" columns in **Figure 1.5** follow the dipole selection rules for both RCP and LCP lights (*i.e.* $\Delta m = +1$ and $\Delta m = -1$, respectively), while the spin *s* is conserved. Clearly, we can observe a dichroism in the helical light absorption, as different absorbed photon energies represented by different lengths of the arrows. In the column on the right-hand side ("absorption spectrum" column) of **Figure 1.5**, the absorption spectrum for the case of the transition from $| 2\ \pm 1 >$ state is illustrated. For RCP light ($\Delta m = +1$) only transitions from $| 2\ 1\ \uparrow\downarrow >$ are allowed, while for LCP light ($\Delta m = -1$) only transitions from $| 2\ -1\ \uparrow\downarrow >$ are allowed, which results in different peaks in the absorption spectra shown in the "absorption spectrum" column.

We note that from the electron transitions, the macroscopic parameters such as diagonal (σ_{xx}) and off-diagonal (σ_{xy}) components of conductivity tensors can be calculated using the Kubo formula,[11-12] which allows us to obtains the optical permittivity tensor

components such as diagonal (ε_{xx}) and off-diagonal (ε_{xy}) components using Maxwell equations.[9] From the macroscopic optical parameters such as ε_{xx} and ε_{xy}, one can obtain all MO observables, as discussed in the next part. Therefore, Kubo's formular and Maxwell equations can be considered as a bridge between the microscopic origin and macroscopic parameter of MO effects, as presented in **Figure 1.4**.

1.2.2. The Macroscopic Optical Parameters of MO Effect

In this part, we discuss about the characteristic of MO materials with their associated permittivity tensor, which contains magnetic field induced anti-symmetric off-diagonal components, and how they give rises to the rotation (in Faraday effect and MOKE) as well as circular dichroism (in MCD) after light-material interaction processes. The derivation in this section is based on the following references [4-5, 13-16].

- *Wave equation*

We start off with the electromagnetic filed in a medium, which can be described by the Maxwell equations,

$$\boldsymbol{\nabla} \times \mathbf{E} + \frac{\partial \mathbf{B}}{\partial t} = 0 \tag{1.4}$$

$$\boldsymbol{\nabla} \times \mathbf{H} - \frac{\partial \mathbf{D}}{\partial t} = \mathbf{J} \tag{1.5}$$

$$\boldsymbol{\nabla} \cdot \mathbf{B} = \mathbf{0} \tag{1.6}$$

$$\boldsymbol{\nabla} \cdot \mathbf{D} = \rho \tag{1.7}$$

along with the constitutive equations

$$\mathbf{D} = \varepsilon_0 \mathbf{E} + \mathbf{P} \tag{1.8}$$

$$\mathbf{H} = \frac{1}{\mu_0}\mathbf{B} - \mathbf{M} \tag{1.9}$$

Assuming that no sources are present (*i.e.* $\mathbf{J} = \mathbf{0}$ and $\rho = 0$), applying the time-harmonic ansatz

$$\Psi(\mathbf{r}, t) = \Psi(\mathbf{r})\boldsymbol{e}^{-i\omega t} \tag{1.10}$$

where $\Psi = \mathbf{E}, \mathbf{B}, \mathbf{D}, \mathbf{H}$, the equations (1.4)–(1.9) become

$$\boldsymbol{\nabla} \times \mathbf{E}(\mathbf{r}) - \mathbf{i}\omega \mathbf{B}(\mathbf{r}) = 0 \tag{1.11}$$

$$\boldsymbol{\nabla} \times \mathbf{H}(\mathbf{r}) + \mathbf{i}\omega \mathbf{D}(\mathbf{r}) = \mathbf{0} \tag{1.12}$$

$$\boldsymbol{\nabla} \cdot \mathbf{B}(\mathbf{r}) = \mathbf{0} \tag{1.13}$$

$$\boldsymbol{\nabla} \cdot \mathbf{D}(\mathbf{r}) = 0 \tag{1.14}$$

along with the constitutive equations

$$\mathbf{D}(\mathbf{r}) = \varepsilon_0 \varepsilon(\omega)\mathbf{E}(\mathbf{r}) \tag{1.15}$$

$$\mathbf{B}(\mathbf{r}) = \mu_0 \mu(\omega)\mathbf{H}(\mathbf{r}) \tag{1.16}$$

At optical frequencies, we assume that $\mu = 1$. By applying the operator $\boldsymbol{\nabla} \times$ to equation (1.11), using $\boldsymbol{\nabla} \times (\boldsymbol{\nabla} \times \mathbf{E}) = \boldsymbol{\nabla}(\boldsymbol{\nabla} \cdot \mathbf{E}) - \Delta\mathbf{E}$ and equation (1.14), we obtained the well-known Helmholtz wave equation

$$\Delta\mathbf{E}(\mathbf{r}) + \frac{\omega^2}{c_0^2}\varepsilon(\omega)\mathbf{E}(\mathbf{r}) = 0 \tag{1.17}$$

We note that the dielectric tensor $\varepsilon(\omega)$ is a tensorial quantity and frequency dependent.

- *Faraday effect*

We consider a light beam with *x*-polarization, normally incidents to a magnetic material thin film. In this case, the dielectric tensor ε of the material is assumed as an optically isotropic medium, and when no magnetic field is present it can be written as,

$$\varepsilon = \begin{pmatrix} \varepsilon_{xx} & 0 & 0 \\ 0 & \varepsilon_{xx} & 0 \\ 0 & 0 & \varepsilon_{xx} \end{pmatrix}. \tag{1.18a}$$

Under the presence of a magnetic field, ε becomes non-diagonal and adopts the following form,[7]

$$\varepsilon = \begin{pmatrix} \varepsilon_{xx} & 0 & 0 \\ 0 & \varepsilon_{xx} & 0 \\ 0 & 0 & \varepsilon_{xx} \end{pmatrix} + \begin{pmatrix} 0 & -i\varepsilon_{xy} & -i\varepsilon_{xz} \\ i\varepsilon_{xy} & 0 & -i\varepsilon_{yz} \\ i\varepsilon_{xz} & i\varepsilon_{yz} & 0 \end{pmatrix}. \tag{1.18b}$$

For the Faraday effect or PMOKE, the magnetic field are aligned perpendicular to the sample plane (xy-plane). In this case, only the *x*- and *y*-components of electromagnetic field will be coupled, and ε is therefore simplified to the following form,[7]

$$\varepsilon = \begin{pmatrix} \varepsilon_{xx} & 0 & 0 \\ 0 & \varepsilon_{xx} & 0 \\ 0 & 0 & \varepsilon_{xx} \end{pmatrix} + \begin{pmatrix} 0 & -i\varepsilon_{xy} & 0 \\ i\varepsilon_{xy} & 0 & 0 \\ 0 & 0 & 0 \end{pmatrix}. \tag{1.18c}$$

In order to solve the wave equation (1.17), we use the ansatz for a plane wave propagating in *z*-direction:

$$\mathbf{E}(\mathbf{r}) = E\mathrm{e}^{i\mathbf{k}\cdot\mathbf{z}}\hat{\boldsymbol{z}} \tag{1.19}$$

where $k = \frac{n\omega}{c}$ is the wave vector amplitude.

Inserting equation (1.18c) and (1.19) into wave equation (1.17) and solving it, we achieve the non-zero solutions for the electric vector of light $\varepsilon_0 n_{\pm}^2(E_x \pm iE_y)$, *i.e.* a RCP and a LCP light with complex indices of

$$n_{\pm}^2 = \varepsilon_{xx} \pm \varepsilon_{xy} \tag{1.20}$$

As mentioned previously, the linear polarized incident light can be decomposed into two circularly polarized beams: RCP beam with $\sigma = +1$ and LCP beam with $\sigma = -1$. Therefore, at the exit of a linear polarized light traveling through a transparent magnetic medium with magnetic-induced permittivity ε and travel length L, the output wave can be described by

$$\mathbf{E} = (\mathbf{E}_+ \mathrm{e}^{\frac{\mathrm{i}\omega n_+ L}{c}} + \mathbf{E}_- \mathrm{e}^{\frac{\mathrm{i}\omega n_- L}{c}})\mathrm{e}^{\frac{\mathrm{i}\omega z}{c} - \mathrm{i}\omega t} \tag{1.21}$$

If the imaginary parts of complex refractive indices $n_{\pm}$ are different, the output beam is elliptically polarized. As a result, the Faraday rotation (FR) and Faraday ellipticity (FE) can be written as,[15]

$$FR = \frac{\omega}{2c}\mathrm{Re}(n_+ - n_-)L \approx \mathrm{Re}(\frac{\pi L \varepsilon_{xy}}{\lambda \varepsilon_{xy}^{1/2}}) \tag{1.22}$$

$$FE = tanh[-\frac{\omega}{2c} Im(n_+ - n_-)L] \tag{1.23}$$

Since the absorption difference is usually small in transparent materials, we can approximate *FE* as,

$$FE \approx -\frac{\omega}{2c}\mathrm{Im}(n_+ - n_-)L \approx -\mathrm{Im}(\frac{\pi L \varepsilon_{xy}}{\lambda \varepsilon_{xy}^{1/2}}) \tag{1.24}$$

- *Kerr effect*

For the PMOKE configuration, the external magnetic field is parallel to the wave vector as in Faraday configuration, and therefore the tensorial optical permittivity ε still can be described by equation (1.18). From these refractive indices of $n_{\pm}$, we obtained the complex Fresnel amplitude of reflection coefficients for $\sigma^{\pm}$ reflection modes:

$$r_{\pm} = -\frac{n_{\pm}-1}{n_{\pm}+1} = \left|r_{\pm}\right| e^{i\phi_{\pm}} \tag{1.25}$$

Then, the polar Kerr rotation and polar Kerr ellipticity can be written as

$$KR = -\frac{\phi_{+}-\phi_{-}}{2} \approx -Im\left(\frac{n_{+}-n_{-}}{n_{+}n_{-}-1}\right) \tag{1.26}$$

$$KE = -\frac{|r_{+}|-|r_{-}|}{|r_{+}|+|r_{-}|} \approx -Re\left(\frac{n_{+}-n_{-}}{n_{+}n_{-}-1}\right) \tag{1.27}$$

The solution for other Kerr-effect geometries can be found in references [4, 16].

- *MCD effect*

From equation (1.3), the MCD can be furtherly written as:

$$\begin{aligned}\Delta A = A_{+} - A_{-} &= -\log_{10}\left(\frac{I_{+}}{I_0}\right) + \log_{10}\left(\frac{I_{-}}{I_0}\right) \\ &= -\log_{10} e^{-\frac{2\omega L}{c}\mathrm{Im}(n_{+})} + \log_{10} e^{-\frac{2\omega L}{c}\mathrm{Im}(n_{-})} \\ &= 2(\log_{10} e)\frac{\omega L}{c}\mathrm{Im}(n_{+} - n_{-})\end{aligned} \tag{1.28}$$

where I_0 and $I_{\pm}$ are the initial intensity and transmitted of the light intensity (with $\sigma = +1$ and $\sigma = -1$ modes) after passing through a transparent magnetic material, respectively.

1.3. Composite Materials and Effective Medium Theory (MO Effects)

1.3.1. Composite Materials

In a broad context, a material which is produced from two or more constituent materials is considered as a composite material. Composite consists of at least two components: (i) the matrix/host as the continuous phase; and (ii) the reinforcement/inclusion as the discontinuous or dispersed phase.[17] In nature, composite materials exist abundantly; for example, wood is a fibrous composite of cellulose fibers and lignin matrix, bone is a composite of soft collagen fibers and apatite matrix,[18] etc. Artificially, humans have been learning to create composite materials, from a very primitive form such as a composite brick of mud and straw (circa 1500 BC, by Egyptians and Mesopotamian),[17] to a highly complex composite form such as fiber reinforced composites employed in aircraft and astronomical applications.[18] Whilst an uncountable amount of composite materials has been created and utilized for numerous of different applications, they generally have two common features with the later one is highly desirable: (i) a combination of characteristics found in each constituent materials, and (ii) characteristics that are not presented in any of constituent materials in isolation.[18-20] Composite materials is not only limitedly employed in the macro worlds, the utilization of composite in nanostructures and nanodevices has also made a tremendous impact in the advancement of nanosciences such as nanocatalyst,[21] energy storage,[22] biomaterial,[23] photonics,[24] etc.

1.3.2. Effective Medium Theory of Composite Materials (MO Effects)

For composite or mixed materials, the effective medium theory (EMT) is one of the most common theoretical approach that describes the macroscopic properties of the system. EMT is developed based on the mean-field theory to account for the physical properties of all constitutes and their associated composition ratios, and has been used to generate adequate approximations for optical, MO, electrical, magnetic, thermal and mechanical properties of composite material systems.[25] In this thesis, we only concern the optical and MO coefficients of composite materials, *i.e.* the diagonal optical permittivity coefficient ε_{xx} and the off-diagonal coefficient ε_{xy}. Some modified EMT models for MO materials based on Maxwell-Garnett EMT, Bruggeman EMT, and others will be discussed in the next part.

- *Modified Maxwell-Garnett model (based on the derivation of Hui et al.[26])*

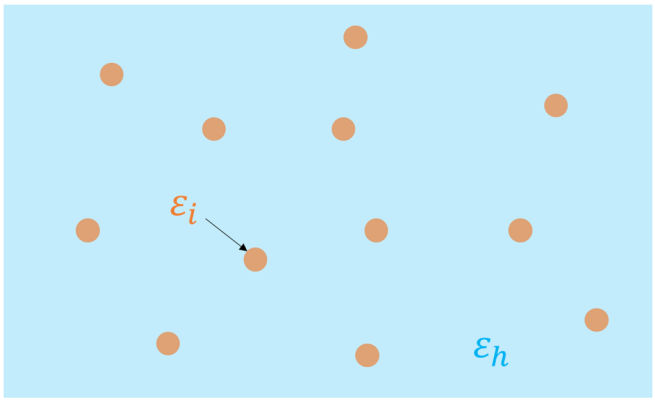

Figure 1.6. Maxell-Garnett composite model. Modified from Ref. [26].

Maxwell-Garnett EMT is one of the most widely applied EMT for experimental data.[27] The basic geometry consists of a suspension of identical magnetic spherical particles of dielectric tensor ε_i in a host of the scalar dielectric function ε_h, as depicted in **Figure 1.6**.[26] Assume that the inclusion is optically isotropic ferromagnet medium, in Faraday configuration, the dielectric tensor ε_i can be written as,

$$\varepsilon_i = \begin{pmatrix} \varepsilon_{xx}^i & 0 & 0 \\ 0 & \varepsilon_{xx}^i & 0 \\ 0 & 0 & \varepsilon_{xx}^i \end{pmatrix} + \begin{pmatrix} 0 & -i\varepsilon_{xy} & 0 \\ i\varepsilon_{xy} & 0 & 0 \\ 0 & 0 & 0 \end{pmatrix}, \tag{1.29}$$

In the case volume fraction limit f of the inclusion is small ($f \ll 1$), the effective dielectric tensor of the composite is approximate by the following equation,[26]

$$\varepsilon_{eff} = \begin{pmatrix} \varepsilon_{xx}^{eff} & 0 & 0 \\ 0 & \varepsilon_{xx}^{eff} & 0 \\ 0 & 0 & \varepsilon_{zz}^{eff} \end{pmatrix} + \begin{pmatrix} 0 & -iA_e & 0 \\ iA_e & 0 & 0 \\ 0 & 0 & 0 \end{pmatrix} \tag{1.30}$$

with

$$\varepsilon_{xx}^{eff} = \varepsilon_h + 3f\varepsilon_h \frac{(\varepsilon_{xx}^i - \varepsilon_h)(2\varepsilon_h + \varepsilon_{xx}^i) - \varepsilon_{xy}^2}{(2\varepsilon_h + \varepsilon_{xx}^i + \varepsilon_{xy})(2\varepsilon_h + \varepsilon_{xx}^i - \varepsilon_{xy})}, \tag{1.31}$$

$$A_e = \frac{9f\varepsilon_h^2 \varepsilon_{xy}}{(2\varepsilon_h + \varepsilon_{xx}^i + \varepsilon_{xy})(2\varepsilon_h + \varepsilon_{xx}^i - \varepsilon_{xy})}, \tag{1.32}$$

$$\varepsilon_{zz}^{eff} = \varepsilon_h + 3f\varepsilon_h \frac{(\varepsilon_{xx}^i - \varepsilon_h)}{(2\varepsilon_h + \varepsilon_{xx}^i)}. \tag{1.33}$$

We note that, in the low magnetic field limit, ε_{xy} becomes negligible and equations (1.31) and (1.33) become identical, as they reduce to the standard Maxwell-Garnet formula.[26-27]

- *Modified Bruggeman model (based on the derivation of You et al.[28])*

The main issue with Maxwell-Garnett EMT is that it only applies when the volume fraction of the inclusions is small, typically $f < 10\%$. The Bruggeman EMT, avoids this problem by considering a binary system of ellipsoids of two materials that are randomly interspersed, as shown in **Figure 1.7**. The structure is composed of ellipsoids whose dielectric tensor are ε_M (or ε_N) with probability f (or $1 - f$), and they are embedded in an effective medium whose dielectric tensor is ε_{eff}. Again, we assume that constituent M is optically isotropic ferromagnet medium and magnetized in Faraday configuration, and constituent N is nonmagnetic medium, their dielectric tensors are written by,

$$\varepsilon_M = \begin{pmatrix} \varepsilon_{xx}^M & 0 & 0 \\ 0 & \varepsilon_{xx}^M & 0 \\ 0 & 0 & \varepsilon_{xx}^M \end{pmatrix} + \begin{pmatrix} 0 & -i\varepsilon_{xy} & 0 \\ i\varepsilon_{xy} & 0 & 0 \\ 0 & 0 & 0 \end{pmatrix}, \tag{1.34}$$

$$\varepsilon_N = \begin{pmatrix} \varepsilon_{xx}^N & 0 & 0 \\ 0 & \varepsilon_{xx}^N & 0 \\ 0 & 0 & \varepsilon_{xx}^N \end{pmatrix}, \tag{1.35}$$

$$\varepsilon_{eff} = \begin{pmatrix} \varepsilon_{xx}^{eff} & 0 & 0 \\ 0 & \varepsilon_{xx}^{eff} & 0 \\ 0 & 0 & \varepsilon_{xx}^{eff} \end{pmatrix} + \begin{pmatrix} 0 & -iA_e & 0 \\ iA_e & 0 & 0 \\ 0 & 0 & 0 \end{pmatrix}, \tag{1.36}$$

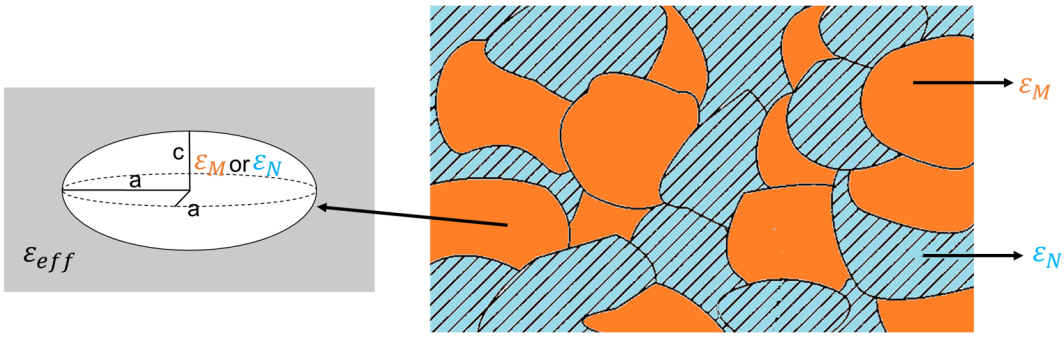

Figure 1.7. Bruggeman composite model. Modified from Ref. [28].

The induced polarization $\overrightarrow{P_{M,N}}$ of medium M, N embedded in effective medium ε_{eff}, under external electric field $\overrightarrow{E_0}$ applied along *x*-direction can be approximated by,

$$\overrightarrow{P_{M,N}} = (\varepsilon_{M,N} - \varepsilon_{eff}) \cdot [\varepsilon_{eff} + \overleftrightarrow{L} \cdot (\varepsilon_{M,N} - \varepsilon_{eff})]^{-1} \cdot \varepsilon_{eff} \cdot \overrightarrow{E_0}, \tag{1.37}$$

where $\overleftrightarrow{L}$ is a depolarization tensor. Assuming the ellipsoid takes a spherical shape, the tensor $\overleftrightarrow{L}$ reduces to a scalar value of 1/3. On the other hand, from the definition of EMT, the total polarization of the medium must be zero,

$$f\overrightarrow{P_M} + (1-f)\overrightarrow{P_N} = 0. \tag{1.38}$$

Combining (1.37) and (1.38) and using L = 1/3, we obtain:

$$(\varepsilon_{xx}^{eff})^2 + (\tfrac{1-3f}{2}\varepsilon_{xx}^M + \tfrac{3f-2}{2}\varepsilon_{xx}^N)\varepsilon_{xx}^{eff} - \tfrac{1}{2}\varepsilon_{xx}^M\varepsilon_{xx}^N = 0. \tag{1.39}$$

Solving equation (1.39) to obtain ε_{xx}^{eff}, we can calculate the off-diagonal component A_e as follows:

$$A_e = \frac{(f-1/3)\varepsilon_{xx}^{eff}+\varepsilon_{xx}^{N}/3}{4\varepsilon_{xx}^{eff}/3+(1/3-f)\varepsilon_{xx}^{M}+(f-2/3)\varepsilon_{xx}^{N}}\varepsilon_{xy}. \quad (1.40)$$

- *Symmetrized Maxwell-Garnett model (based on the derivation of Granovsky et al.[29])*

In order to work with an arbitrary values of ferromagnetic volume fraction, Granovsky *et al.* developed the symmetrized Maxewll-Garnett (SMG) theory,[29] which is the modified version of both Maxwell-Garnett and Bruggerman EMT and shows the advantages over these theories. Again, we consider a composite of magnetic medium M and nonmagnetic medium N, and we assume that constituent M (with volume fraction *f*) is optically isotropic ferromagnet medium and magnetized in Faraday configuration, and constituent N is nonmagnetic medium, their dielectric tensors are written as in equations (1.34)–(1.36).

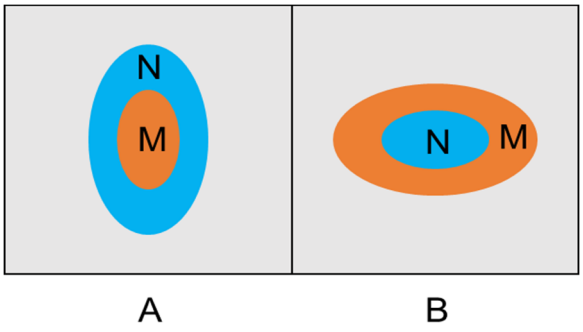

Figure 1.8. Random unit A and B in the SMG approximation. Modified from Ref. [29].

Two random unit A and B are introduced: unit A – an inclusion of M coated by a shell of N; unit B – an inclusion of N coated by a shell of M (**Figure 1.8**). The probabilities to find these unit in the composites are

$$P_A = u_1/(u_1 + u_2);\ P_B = u_2/(u_1 + u_2), \tag{1.41}$$

where $u_1 = (1 - f^{1/3})^3;\ u_1 = [1 - (1 - f^{1/3})]^3$.

Using Maxwell-Garnett approximation, we can estimate the dielectric function of both type A and B, using equations

$$\frac{\varepsilon_{\mathrm{A}}^{MG} - \varepsilon_{xx}^{N}}{\varepsilon_{xx}^{N} + (\varepsilon_{\mathrm{A}}^{MG} - \varepsilon_{xx}^{N})/3} - f\frac{\varepsilon_{xx}^{M} - \varepsilon_{xx}^{N}}{\varepsilon_{xx}^{N} + (\varepsilon_{xx}^{M} - \varepsilon_{xx}^{N})/3} = 0, \tag{1.42}$$

$$\frac{\gamma_{\mathrm{A}}^{MG}}{[\varepsilon_{xx}^{N} + (\varepsilon_{\mathrm{A}}^{MG} - \varepsilon_{xx}^{N})/3]^2} - f\frac{\gamma_{\mathrm{A}}^{MG}}{[\varepsilon_{xx}^{N} + (\varepsilon_{xx}^{M} - \varepsilon_{xx}^{N})/3]^2} = 0, \tag{1.43}$$

$$\frac{\varepsilon_{\mathrm{B}}^{MG} - \varepsilon_{xx}^{N}}{\varepsilon_{xx}^{N} + (\varepsilon_{\mathrm{B}}^{MG} - \varepsilon_{xx}^{N})/3} - f\frac{\varepsilon_{xx}^{M} - \varepsilon_{xx}^{N}}{\varepsilon_{xx}^{N} + (\varepsilon_{xx}^{M} - \varepsilon_{xx}^{N})/3} = 0, \tag{1.44}$$

$$\frac{\gamma_{\mathrm{B}}^{MG}}{[\varepsilon_{xx}^{N} + (\varepsilon_{\mathrm{B}}^{MG} - \varepsilon_{xx}^{N})/3]^2} - f\frac{\gamma_{\mathrm{B}}^{MG}}{[\varepsilon_{xx}^{N} + (\varepsilon_{xx}^{M} - \varepsilon_{xx}^{N})/3]^2} = 0, \tag{1.45}$$

where γ_{A}^{MG} and γ_{B}^{MG} are off-diagonal component of the effective dielectric function of type A and B, respectively.

Using Bruggeman approximations for unit A and B, we obtain the effective dielectric function for the composite by solving these equations,

$$\frac{P_A(\varepsilon_{\mathrm{A}}^{MG} - \varepsilon_{xx}^{eff})}{\varepsilon_{xx}^{eff} + (\varepsilon_{\mathrm{A}}^{MG} - \varepsilon_{xx}^{eff})/3} + \frac{P_B(\varepsilon_{\mathrm{B}}^{MG} - \varepsilon_{xx}^{eff})}{\varepsilon_{xx}^{eff} + (\varepsilon_{\mathrm{B}}^{MG} - \varepsilon_{xx}^{eff})/3} = 0, \tag{1.46}$$

$$\frac{P_A(A_e - \gamma_{\mathrm{A}}^{MG})}{[\varepsilon_{xx}^{eff} + (\varepsilon_{\mathrm{A}}^{MG} - \varepsilon_{xx}^{eff})/3]^2} + \frac{P_B(A_e - \gamma_{\mathrm{B}}^{MG})}{[\varepsilon_{xx}^{eff} + (\varepsilon_{\mathrm{B}}^{MG} - \varepsilon_{xx}^{eff})/3]^2} = 0, \tag{1.47}$$

1.4. The Magneto-optical Plasmonic Effects

1.4.1. Surface Plasmon Resonance

Surface plasmon resonance (SPR) is a physical phenomenon arisen by the light-material interaction at the interface of metallic materials (especially in noble metals such as Au, Ag) and dielectric materials.[30] Under the excitation of an electromagnetic wave, the free electrons in metal are driven to oscillate; and at some specific frequencies where the resonance conditions are met, the amplitude of the oscillation reaches maximum and electric field strength at the interface is significantly enhanced. Plasmonic materials have shown a great promise in multiple domains: physics, chemistry, biology, etc.[30-33]

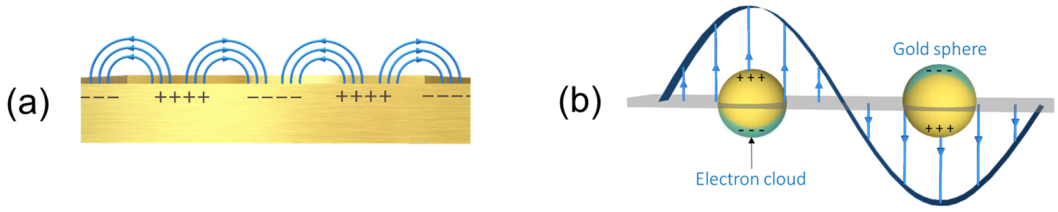

Figure 1.9. Plasmonic effects in different metallic nano-structure: (a) surface plasmon polariton (SPP) and (b) localized surface plasmon resonance (LSPR). Modified from Ref. [7].

SPR can be supported in a wide range of metallic nanoarchitectures such as thin film, nanoparticles, nanowires, etc., and the plasmonic resonance condition depends on several factor affecting the electron charge density on the metal surface, such as size, shape, materials, surrounding medium, composition, etc.[3] They are typically classified into two categories, depending on the dimensionality of the supporting structure (**Figure 1.9**): (i)

surface plasmon polariton (SPP) or propagating surface plasmon (**Figure 1.9a**); and (ii) localized surface plasmon resonance (LSPR) (**Figure 1.9b**).

- *Surface plasmon polariton (SPP)*

SPPs are electromagnetic excitation propagating at the planar metal-dielectric interfaces, which are stimulated via the coupling between incident electromagnetic wave and the conductor electron plasma. Deriving from Maxwell's equations, the dispersion relationship for a typical SPP in a single, flat metal-dielectric interfaces can be written as,

$$\beta_{SPP} = \frac{\omega}{c}\sqrt{\frac{\varepsilon_d \varepsilon_m}{\varepsilon_d + \varepsilon_m}}, \tag{1.48}$$

where β_{SPP} is the wave vector of the SPP, and ε_d and ε_m are the complex optical permittivity of the dielectric and metal, respectively.

Due to the non-zero absorption of metal, SPP can only propagate for a finite distance along the interface. On the other hand, evanescent electric field drop exponentially in the perpendicular direction to the interface, and it can only penetrate into the metal by a certain tiny distance of "skin depth". SPP is well-known to be very sensitive to any disturbance within the skin depth, and has been used in commercialized ultrasensitive chemical and biosensor.[30, 34]

- *Localized surface plasmon resonance (LSPR)*

In contrast to SPP, LSPR happens where the collective oscillation of electron is trapped in a confined volume, whose dimension is smaller than the wavelength of the exciting light.[35] For example, considering a small spherical nanoparticle (NP, with a radius of *R*) excited

by an electromagnetic wave (R/λ < 0.1), the coherent oscillation of conduction electrons leads to an accumulation of polarization charge on the surface of NP, and the cross-section extinction spectrum of the NP can be estimated by the well-known Mie's solution of Maxwell's equations,[35]

$$C_{ext} = \frac{24\pi^2 R^3 \varepsilon_d^{3/2} N}{\lambda ln(10)} \frac{\varepsilon_i}{(\varepsilon_r + 2\varepsilon_d)^2 + \varepsilon_i^2}, \quad (1.49)$$

where $\varepsilon_m = \varepsilon_r + i\varepsilon_i$ is the complex dielectric constant of metal, and N is the electron density. From the relation above, it is seen that any change in the size and metal/surrounding medium can induce an LSPR wavelength shift.

1.4.2. Magneto-optical Plasmonics

The plasmonic structure and plasmonic materials have been intensively investigated in the last few decades, however, their potential is still far from being fully employed. A significant advance for the plasmonic functionality in this sense can be made by augmenting the ability of being actively controlled by an external stimulus, such as using electrical, magnetic, temperature, mechanical stimulus, etc.[3] Among all of these possible controls externally for active plasmonic system, magnetic field is one of the most prominent candidates: the magnetic tuning based on MO effects is fully reversible, non-contacting, robust upon cycling, and ultrafast.[36-37] As a result, the study of the interaction between the plasmonic effect and MO effect has been attracting a considerable attention for the last ten years, and it has become a well-defined research area which is commonly

referred as magneto-optical plasmonics (MOP), or magnetoplasmonics for short (**Figure 1.10a**).

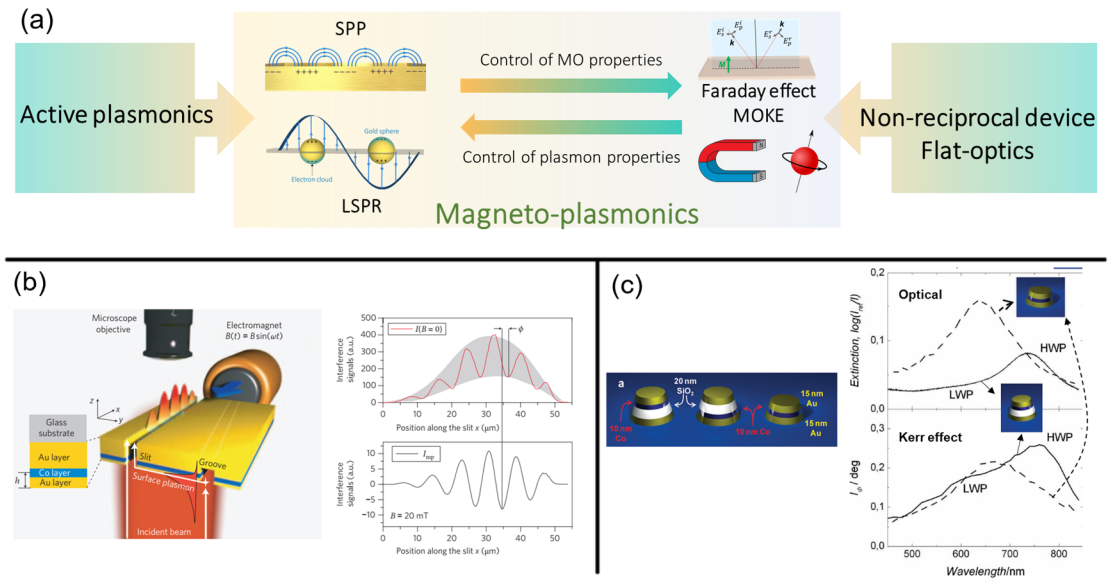

Figure 1.10. (a) Magneto-optical plasmonic (MOP) system. (b) An Au/Co/Au multilayer active magneto-plasmonic interferometry: the SPR are launched by the groove, propagate to the left, interfere with the directly transmitted light, and results in the interference pattern which can be recorded by the microscope objective (left). A phase shift of ϕ in the interference pattern can be seen when applying external magnetic field (right). Modified from Ref. [38]. (c) Metal-dielectric Au/Co/SiO_2/Au and Au/Co/Au MOP nanodisks: by removing/changing the position of dielectric SiO_2 layer (left), the LSPR peak can be tuned and consequently shifts and amplifies MO signal maxima. Modified from Ref. [39].

In a MOP system, plasmonic and magnetic properties co-exist and interact with each other: the external magnetic fields can be used to control or even enhance the optical properties of the system. For example, Temnov *et al.* demonstrated that an oscillating magnetic field can switch the magnetization in the thin Co layer and modify the SPP waves propagating on the Au/Co/Au-air interface, which results in a sizable phase shift in the interference pattern (**Figure 1.10b**).[38] Conversely, the plasmonic effect can also be used to optimize magnetic-optical performance. For instance, Banthi *et al.* show that the amplitude of MO activity and the peak position can be optimized via LSPR, by manipulating the structure design (**Figure 1.10c**).[39]

MOP system and has been normally constructed by combining magnetic materials (Co, Ni, Fe, garnet, etc.) and noble metals (Ag, Au, etc.) to be in an unique entity.[40-41] Transition metals such as Co, Ni, or Fe possess large off-diagonal elements of dielectric tensor (ε_{xy}) at room temperature at a relatively low external magnetic field,[4] due to their spin-orbit coupling and exchange splitting (as presented in **Figure 1.5**) are very large in comparison to those of other metals.[42] Therefore, the MO effects as well as MO coefficients in ferromagnetic metals are a few orders of magnitude larger than those of noble metals. As an example shown in **Figure 1.11a** and **b**, Au show a very small in magnitude of ε_{xy} in the visible wavelength range even at a very high applied magnetic field of 1 Tesla, which is approximately three orders of magnitude smaller than those of Co regardless of wavelength. However, the plasmonic properties of ferromagnetic metals are relatively

weak since their large optical absorptions significantly damp the plasmonic wave.[43-45] In fact, the SPP can barely propagate on the ferromagnetic-air interface (**Figure 1.11c**) and the nanospheres made by ferromagnetic metals do not show any obvious resonance peak (**Figure 1.11d**). On the other hand, noble metals such as Au or Ag are well-known for strong plasmonic effects in the visible/near-infrared region,[46-47] which can be seen through relatively long SPP propagation distances and strong/sharp resonance peaks (**Figure 1.11c** and **d**).

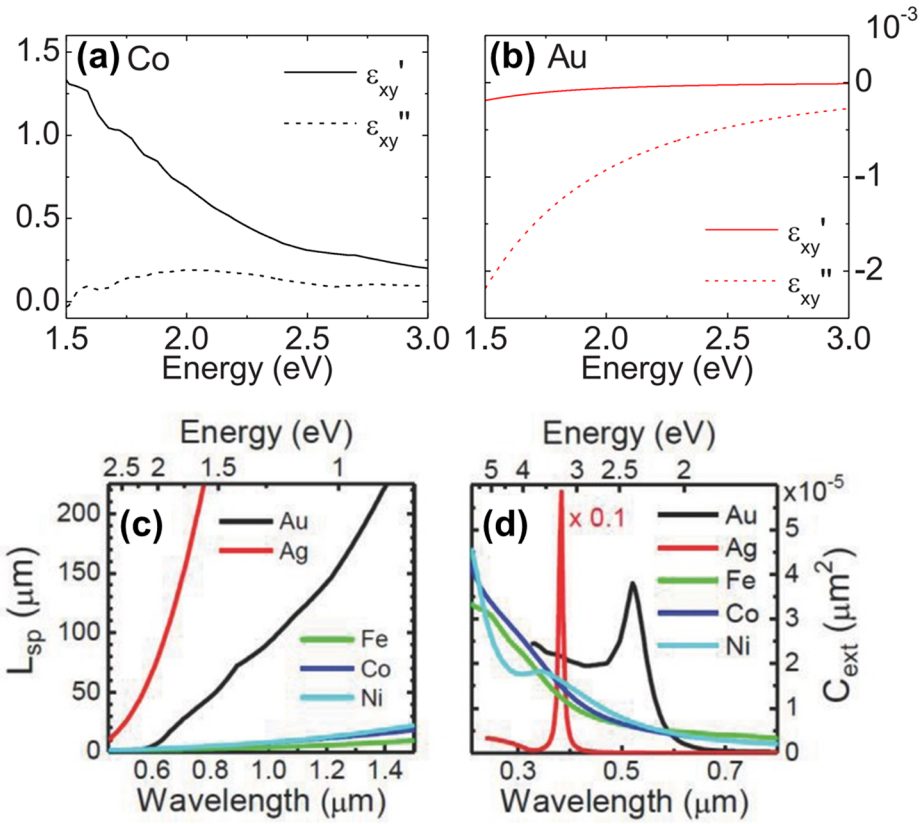

Figure 1.11. Real and imaginary parts of the off-diagonal dielectric components (ε_{xy}) of (a) cobalt and (b) gold. (a-b) are taken from Ref. [48]. (c) Calculated SPP propagating distances (L_{sp}) for some noble and ferromagnetic metals. (d) Calculated extinction cross-section spectra of nanosphere particles made from noble and ferromagnetic metals, in water (*diameter* = 10 nm). (c-d) are taken from Ref. [7].

In order to intertwine the plasmonic effect of noble metals and MO effect of ferromagnetic metals, numerous strategies have been proposed. Among the bottom up-chemical method, core-shell heterodimeric nanoparticle made by the colloidal chemistry synthesis is one of the most noticeable MOP architectures.[3, 49-50] Besides, several other nanoparticles with different shapes (nano-triangle,[51] nano-rod,[52] nanosphere,[53-56] etc.), sizes, and compositions have been synthesized and the evidences of magnetic-plasmonic hybridizations in these systems have been demonstrated. On the other hand, the top-down fabrication approach has been shown to be more flexible on preparing all types of MOP structures such as multilayer/doped thin film,[57-58] nano-dot/anti-dot arrays,[59-73] photonics crystal,[74-75] and others.[62, 76] In all of these works, **multilayer structures** has been usually used, and the multilayer-based MOP devices have shown enhanced MO activities in comparison to identical structures fabricated by pure magnetic material.[7] A different possible configuration is using composites or alloys, however, these composite based MOP system are surprisingly under-investigated.

1.5. Organization of the Dissertation

This dissertation presents a new platform of MOP nanostructures and devices using **composite materials** and their applications for hydrogen sensing. **Chapter 1** covers the basic concept of MO, SPR, and magnetoplasmonics materials. In **Chapter 2**, specialized experimental technique used for sample fabrication, optical/MO characterization, and hydrogen sensing in this dissertation are described. **Chapter 3** introduces the fabrication of composite Ag-Co nanohole arrays and shows MOP properties of the system where the SPP is supported. On the other hand, in **Chapter 4**, we investigate the MOP of Ag-Co composite nano-triangle arrays, where the LSPR mode is supported. In **Chapter 5**, the magneto-chiroptical response of an active Ag-Co chiral nanohole array is studied. **Chapter 6** presents the MO activity of Pd-Co composite nano-patchy structure and its application for hydrogen sensing. Lastly, in **Chapter 7**, we provide some overall conclusions and outlook for composite MOP platform.

CHAPTER 2

METHODS

2.1. Sample Fabrications

2.1.1. The Formation of Self-assembled Monolayers

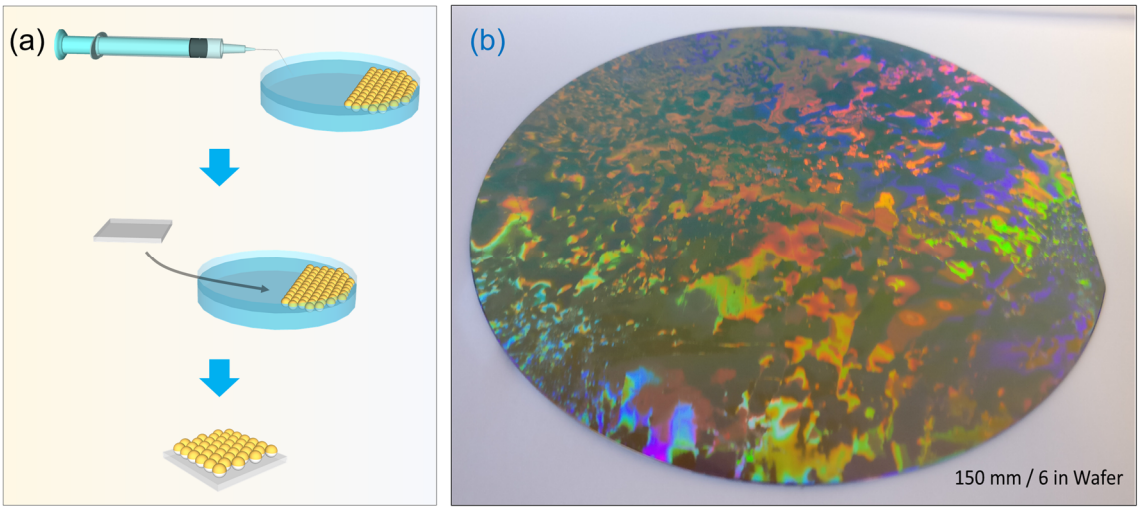

Figure 2.1. (a) A cartoon of the ethanol assisted air-water interface method and images of a wafer scale monolayer fabrication using this method. Cartoon modified from Ref. [77]. (b) An example of the large scale monolayer fabrication, the wafer is Si with a diameter of 150 mm. Photo taken from Ref. [77].

Figure 2.1a depicts the formation procedure of polystyrene (PS) nanosphere monolayer using ethanol assisted air-water interface method.[78-83] The 0.01 %w/v% solution of the PS

nanosphere was washed several times by centrifugating, and diluted with ethanol to a 2:1 volume ratio. The solution was then dispensed onto a Petri dish (filled with 2-mm depth of water) at a rate of 0.009 ml/min. The monolayer was slowly formed on the water surface as the process was carried on. After this process finished, the glass and Si substrates were carefully placed under the monolayer, and the water level was lowered until dry. The achieved monolayer has low defect, large domain, and can be created in a wafer scale monolayer, as an example is shown in **Figure 2.1b**.

2.1.2. Electron Beam Co-evaporation and Nanosphere Lithography

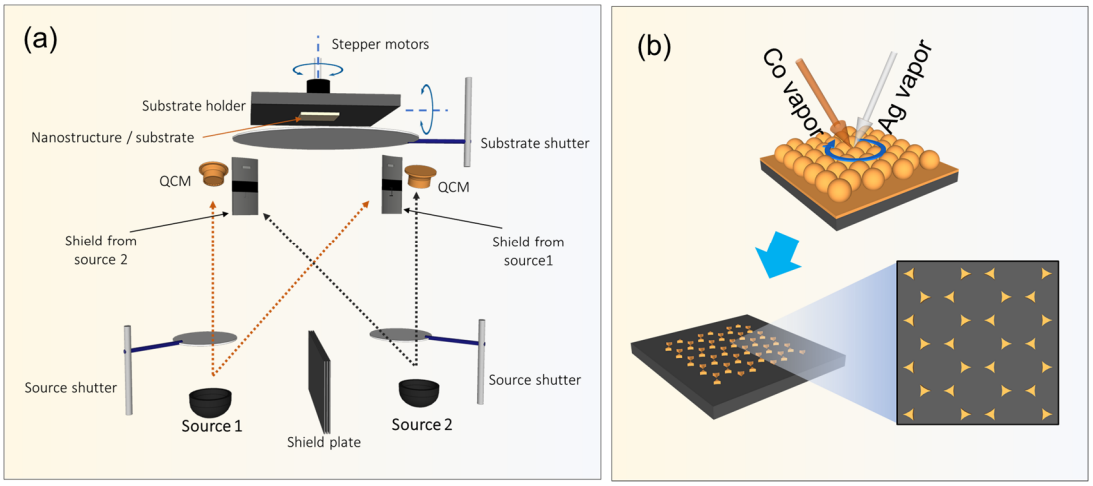

Figure 2.2. (a) A schematic of electron beam co-evaporation. (b) An example of using nanosphere lithography and electron beam co-evaporation for the fabrication of Ag-Co composite nano-triangle arrays.

Electron beam evaporation is one of the most popular physical vapor depositions (PVD) for thin film processing and nanostructure fabrication.[84] In this process, the target material

is heated by a high energy electron beam, vaporized, transported, and condensed on a desired substrate. Based on conventional electron beam evaporation method, we develop electron beam co-evaporation method which allows us to evaporate two different materials simultaneously (**Figure 2.2a**). In this technique, two different materials to form a composite are loaded into two separated crucibles placed in two sides of the high-vacuum chamber, and their thicknesses and deposition rates are measured independently by two separated quartz crystal microbalances (QCMs). By controlling the evaporating rate of each source materials, a composite layer with a desired composition is then formed. We note that as two sources cannot be in the exact same location and potential gradient in the composition might appear, we therefore rotate the substrate azimuthally with an angular velocity of about 30 rpm to remove this effect.[77]

In order to realize the composite nanostructure presented in this dissertation, we combine the electron beam co-evaporation with shadow nanosphere lithography (SNL) technique. In SNL, the self-assembled PS nanosphere monolayers are employed as a template for deposition. An example of Ag-Co composite nano-triangle fabrication using PS nanosphere monolayer as a template is depicted in **Figure 2.2b**: Ag and Co are deposited simultaneously to a colloid monolayer on a clean glass substrate; the monolayer mask is then removed by scotch tape, results in the desired nano-triangle pattern on the glass substrate. In the literature, SNL has been used to realize several nanostructures for catalyst and plasmonic applications, such as nanorod, nano-spring, nanofan, etc.[85-86]

2.2. Magneto-optical Characterizations

2.2.1. Faraday Rotation Spectroscopy

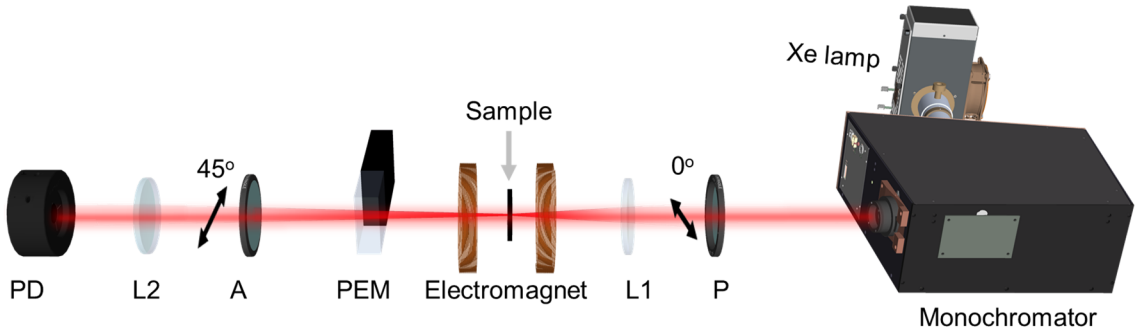

Figure 2.3. Faraday rotation spectroscopy setup.

The schematic of the FR spectroscopy experimental setup is illustrated in **Figure 2.3**.[45, 87] A Xenon lamp is used as a broad band light source, its light beam was collimated and passed a monochromator. The sample is placed between poles of an electromagnet that can generate magnetic field up to 1.77 T that is parallel to the incident monochromatic collimated beam. The FR/FE are measured using photoelastic modulation (PEM) phase sensitive technique with retardation of 2.405 radian. The recorded signal by a lock-in amplifier with modulation frequency of 2f = 100 kHz (V_{2f}) provides the FR angle, while it is FE for signal with modulation frequency of f = 50 kHz (V_f). A rigorous mathematical derivation for this technique can be found in Ref. [5, 87].

We note that by keeping the order of optics and modifying the experimental setup in the transmitted side to collect the reflected light beam, a MOKE spectroscopy experimental

setup can be obtained.[88] Different MOKE configurations (*i.e.* PMOKE, LMOKE, and TMOKE) can be achieved by varying the relative orientation between the magnetic field and the plane of incident light beam.

2.2.2. Magnetic Circular Dichroism (MCD) Spectroscopy

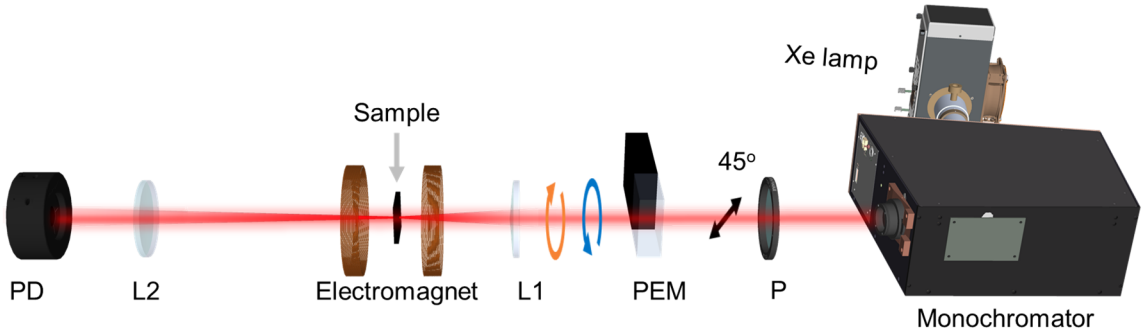

Figure 2.4. Magnetic circular dichroism (MCD) spectroscopy setup.

The schematic of the MCD spectroscopy experimental setup is portrayed in **Figure 2.4**. We utilize the same light source of Xenon lamp and monochromator as in FR spectroscopy setup, however, in this case the monochromatic light is first passed through a polarizer with the polarization axis forming a 45° with the horizontal axis. The light then passes through the PEM with the retardation of 90° to generate the LCP/RCP alternatively with a modulation frequency of f = 50 kHz. Transmitted optical signal is then collected by a photodetector. The dichroism signal with modulation frequency of f = 50 kHz (V_f) is then recorded by a lock-in amplifier. A rigorous mathematical derivation for this technique can be found in Ref. [8, 89].

2.3. Hydrogen Sensing Characterizations

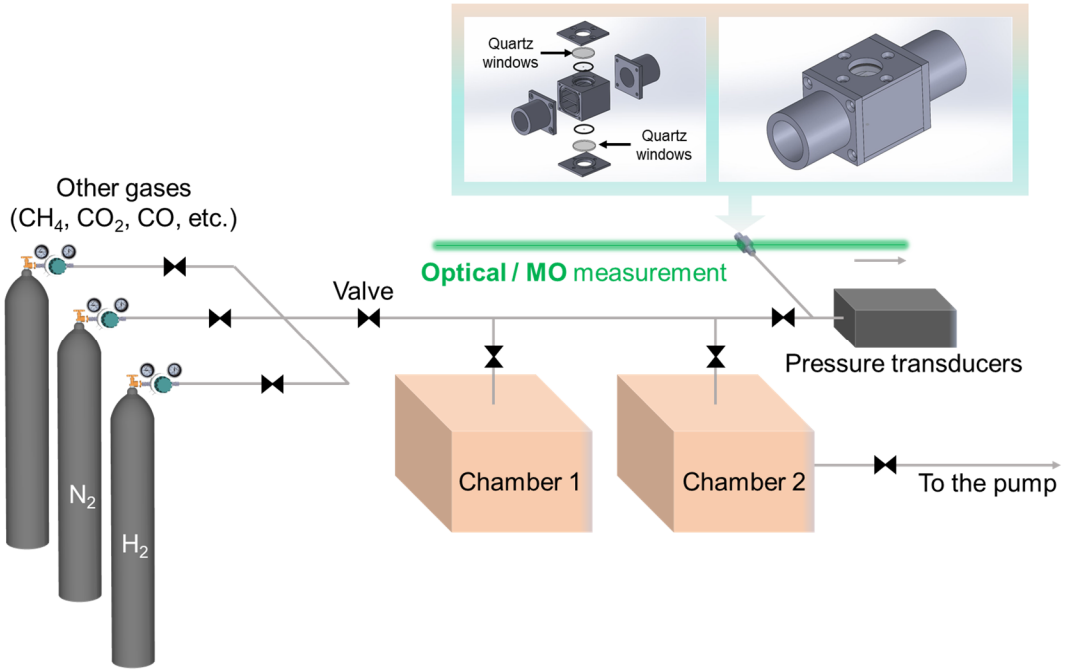

Figure 2.5. Vacuum-mode hydrogen gas sensing experimental setup. The small gas cell with two transparent quartz windows is designed by UGA instrument shop.

Figure 2.5 illustrates the scheme of our home-built vacuum-mode gas sensing experimental setup. The different gases (hydrogen, nitrogen, and toxic gases such as CH_4, CO_2, CO, etc.) are regulated and controlled by several valves before being guided into chamber 1. By recurring diluting the gas in chamber 1 by chamber 2 and pump, we can achieve any arbitrary hydrogen pressure in the pressure range of 10^{-6} to 1.1 bar, which measured by three pressure transducers. The samples are placed inside a custom-made gas cell with two transparent quartz windows, which allows to perform any optical/MO measurements with gas pressure dependence.

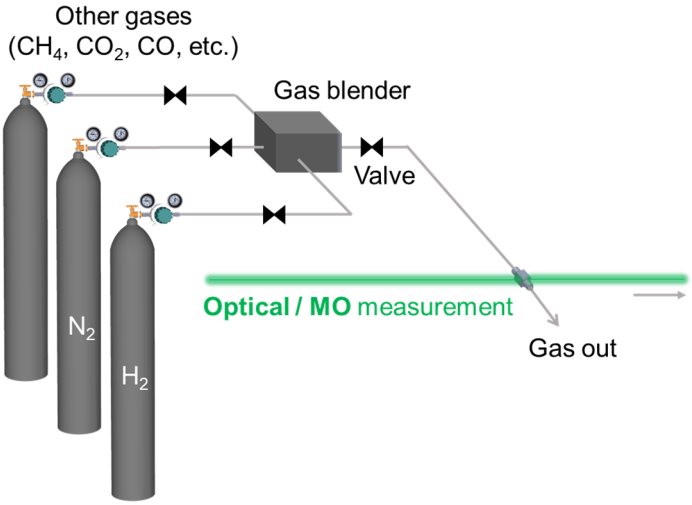

Figure 2.6. Flow-mode hydrogen gas sensing experimental setup.

In addition to vacuum-mode gas sensing setup, we also built a flow-mode characterization setup whose scheme is plotted in **Figure 2.6**. In this setup, hydrogen can be diluted in nitrogen gas or synthetic gas air carrier to part-per-million (ppm) concentration. The setup also allows to blend the hydrogen mixture gas with interference gases such as CH_4, CO_2, CO, etc., which can be used to test the effect of poisonous gas on the hydrogen sensing performance of the sensor.

CHAPTER 3

MAGNETO-PLASMONICS COMPOSITE NANOHOLE ARRAYS

3.1. Introduction

As introduced in **Chapter 1**, the MOP system is a multifunctional materials-based system that support both plasmonic and magnetic properties.[7, 19, 90] This magneto-plasmonic system has been usually realized via **multilayer structures**, where magnetic materials (Co, Ni, Fe, garnet, etc.) and noble metals (Ag, Au, etc.) have been often combined.[7] Clearly, an alternative material system is a **composite material**. The composite of ferromagnetic/plasmonic metal materials (we call composite magneto-plasmonic (CMP) material) could simultaneously have both magnetic and plasmonic properties, which could open another dimension in design of MOP systems and related devices.

Up to now, there was only a limited experimental works on the CMP thin films.[44, 58, 91-94] For example, Yang *et al.* studied the composite film of Co and Au with different Co:Au composition ratios and fabrication temperatures, where they noticed that the MO activities increased with increasing Co composition.[44] A recent study by David *et al.* showed an improvement in magneto-optical surface plasmon resonance (MOSPR) responses and signal-to-noise ratio in a MOSPR sensor using a layer of Au-Co alloy instead of a single layer of Au or a tri-layer sandwiched Au/Co/Au structure.[92] These studies have attempted

to use the CMP materials to improve the MO performances in different applications. However, they have been focusing solely on thin film structures, and the properties of nanostructured CMP materials are generally not considered. Therefore, it would be of great interest to explore the MP properties and potential applications of CMP nanostructures.

In this Chapter, we investigated the MO performance of Ag-Co CMP nanohole array (CNA) structures. The composition dependent optical transmission, PMOKE, FR, and FE of CNAs in the visible to near infrared wavelength region were studied. Finite-difference time domain (FDTD) calculations were performed to confirm the experimental results and to give an insight to the relationship between MO properties of CNA structures and their compositions.

3.2. Fabrications and Characterizations

CNAs were prepared by a combination of the SNL method and the electron beam co-evaporation as presented in **Figure 3.1a**.[95-96] The polystyrene (PS) nanosphere (diameter D = 500 nm) monolayers were firstly assembled onto the pre-cleaned glass substrates by an air/water interface method.[86, 96-97] An oxygen reactive-ion etching (RIE) was carried out to reduced the size of PS nanospheres to about d = 350 nm. The etched PS nanosphere monolayer substrates were loaded into a custom-built dual-source electron deposition system (Pascal Technology) and the vacuum chamber was pumped down under a base pressure of $<10^{-6}$ Torr. In order to enhance the adhesion between the glass substrate and composite thin films, a thin layer of Ti (thickness t_{Ti} = 3 nm, deposition rate 0.05 nm/s)

was firstly evaporated. Then Ag and Co were deposited simultaneously to form a layer of composite materials. Two crucibles with Ag and Co were placed on two sides of the chamber, and the vapor incident angles to substrate normal were 10° and -10°, respectively. Two separated quartz crystal microbalances were used to monitor the deposition rates and thicknesses of Ag and Co independently. By controlling the deposition rates of Ag and Co, Ag-Co composite thin films with varied volumic composition of Co (C_{Co} = 0, 10, 30, 50, 60, 70, 80, 90, and 100 (%V)) were realized. During the co-deposition, the substrates were rotated azimuthally with a constant rotation rate of 30 rpm in order to better mix Ag and Co. The total thickness of composite film ($t_C = t_{Ag} + t_{Co}$) was kept at 50 nm and the total deposition rate from Ag and Co vapor sources was fixed to be 0.6 nm/s. After the codeposition, PS nanospheres were removed by scotch tapes and the samples were washed subsequently by toluene, isopropyl alcohol, and deionized water, which results in CNA structures as showed in **Figure 3.1b**. The control samples, the Ag-Co composite thin films with the same thicknesses and compositions, were also fabricated simultaneously on cleaned glass substrates under identical conditions. Before any characterizations, the CNAs and thin film samples were kept inside a M. Braun glovebox system filled with N_2 (the concentrations of O_2 and H_2O are less than 0.1 ppm) to minize the potential oxidation effects.

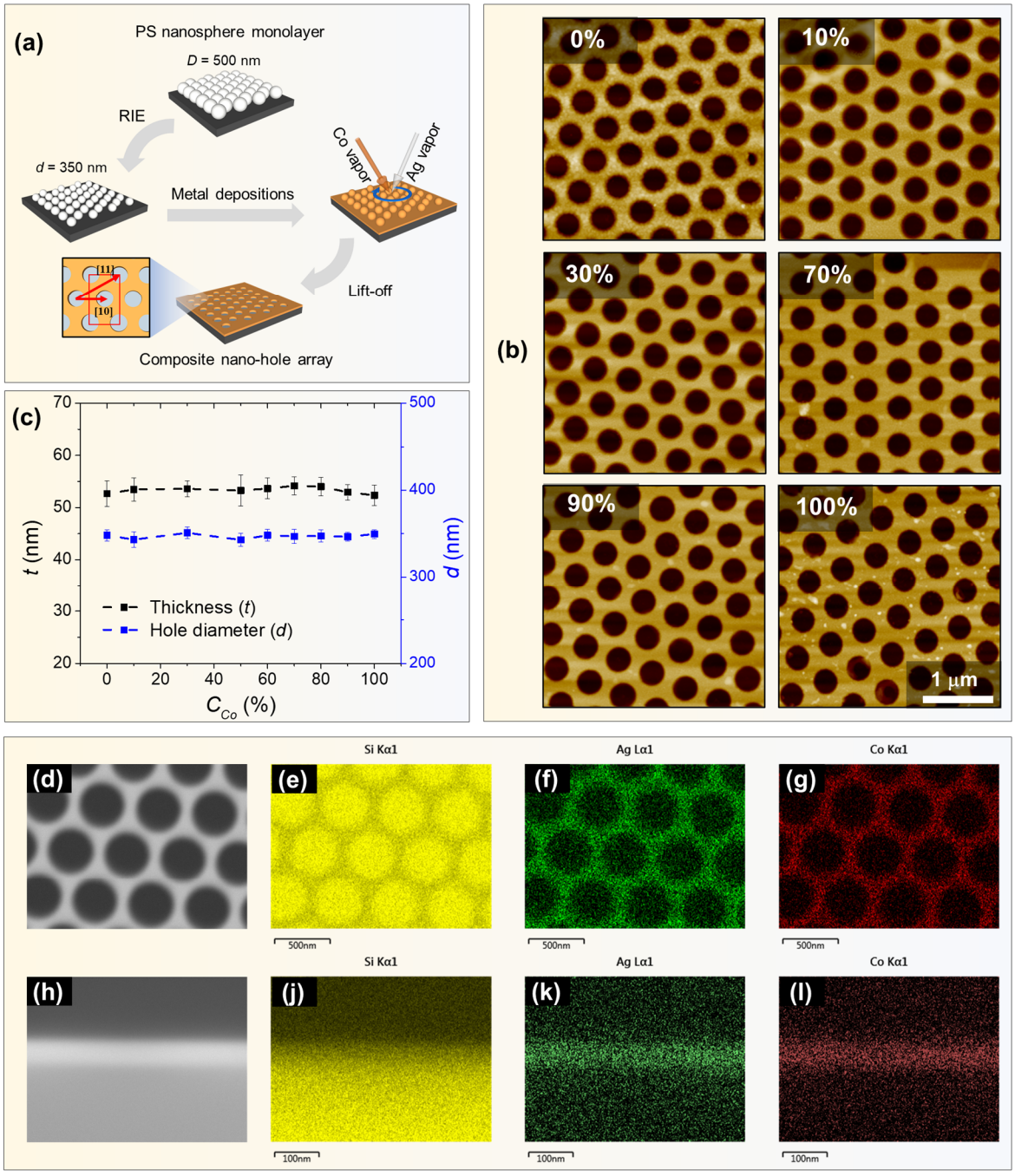

Figure 3.1. (a) The fabrication process of the CNAs and (b) representative AFM images of the CNAs with C_{Co} = 0, 10, 30, 70, 90, and 100%V, respectively. (c) The

extracted thickness (t) and hole diameter (d) of CNAs with different C_{Co} (%V). The measured thickness t = 53 ± 3 nm and hole diameter d = 350 ± 10 nm. (d) Top-view and (h) cross-sectional SEM micrograph of CNA with C_{Co} = 50 %V, and their composition mappings of (e)-(j) Si, (f)-(k) Ag, and (g)-(l) Co. The extracted volumic percentage of Ag, Co, and Ti are 48.7%, 49.2%, and 2.1%, respectively (Si is excluded).

Figure 3.1b shows several representative atomic force microscopy (AFM) images of the hexagonal lattice of nanohole arrays perforated on Ag-Co composite thin films with different C_{Co}. The measured thickness t_C = 53 ± 3 nm and hole diameter d = 350 ± 10 nm (measured at the top surface) are consistent with the values designed in experiment (**Figure 3.1c**). In addition, due to the codeposition configuration, both Ag and Co should be mixed uniformly across the entire substrate. For example, a composition mapping of CNA with C_{Co} = 50 %V can be found in **Figure 3.1d-l**. From both the top view and cross-section view mapping, both Ag and Co are distributed uniformly.

Figure 3.2a compares the C_{Co} experimentally determined by energy-dispersive x-ray spectroscopy (EDS) (C_{Co}^{EDS}) with the C_{Co} calculated based on the deposition rates of Ag and Co (C_{Co}^{cal}). The solid line in **Figure 3.2a** presents $C_{Co}^{EDS} = C_{Co}^{cal}$. Clearly, in all CMP thin films, C_{Co}^{EDS} and C_{Co}^{cal} are consistently matched with each other, which shows the ability of fully controlled C_{Co} by tuning the relative ratio of Ag and Co deposition rates. Given that C_{Co}^{EDS} is approximately equal to C_{Co}^{cal}, from now on all C_{Co}^{cal} will be referred to as C_{Co} to

avoid confusion. Also, CNA samples with a specific Co composition will now be referred to as CNA$_x$, where x = 0, 10, …, 100, respectively, represents the percentage of Co.

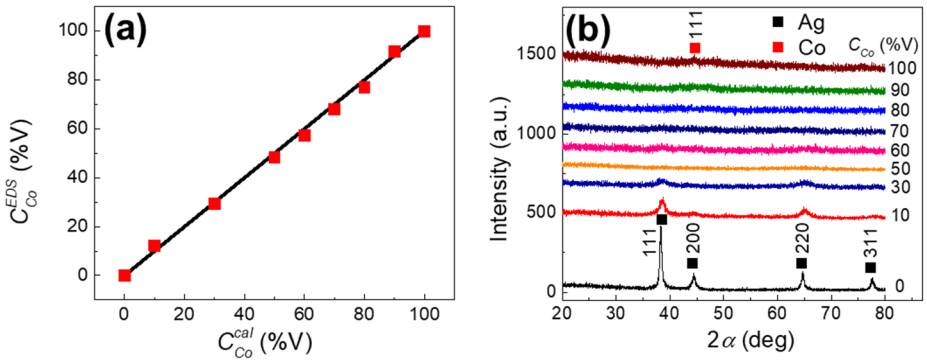

Figure 3.2. (a) The plot of C_{Co}^{EDS} (measured by EDS) versus C_{Co}^{cal} (calculated from deposition rates). The ideal case when $C_{Co}^{EDS} = C_{Co}^{cal}$ is presented as a black solid line. (b) XRD profiles of control magnetic thin films with different C_{Co}.

The x-ray diffraction (XRD) profiles of composite thin films are analyzed and presented in **Figure 3.2b**. Four prominent peaks can be found at the diffraction angles 2α = 38, 44, 64, and 78° for the pure Ag thin film (C_{Co} = 0%V), which correspond to cubic Ag (111), (200), (220), and (311) planes (JCPDS Ref. No. 01-071-3762), respectively. With the introduction of more and more Co, all these peaks become smaller. Only the Ag (111) and (220) peaks are visible at C_{Co} < 50 %V, and when $C_{Co} \geq$ 50 %V, they vanish. On the other hand, a very weak peak at 2α = 44°, which corresponds to the diffraction of fcc Co (111) plane (JCPDS Ref. No. 01-1259), is visible at C_{Co} = 100 %V. For CMP thin films with C_{Co} = 50 to 90 %V, no prominent Co peak is observed, which implies that the

crystallinity states of Co in these composite films are amorphous (or beyond detection limit).

3.3. Optical Properties of CNAs

Figure 3.3a shows the optical transmission spectra ($T(\lambda)$) of CNAs with different C_{Co}. Several transmission peaks/dips can be identified. The prominent features are two transmission dips **AR1** at $\lambda_1^T \approx 440$ nm and **AR2** at $\lambda_2^T \approx 660$ nm, and one transmission peak **R3** at $\lambda_3^T \approx 850$ nm, which are marked by the dash curves in **Figure 3.3a** (and **b**). For CNA_0, the transmission at **R3** (≈ 80 %) is significantly larger than the hole coverage (≈ 56 %). This enhanced transmission at **R3** is well-known as the extraordinary optical transmission (EOT), which has been reported in plasmonic hole lattices made of Ag or Au.[98] At a glance, the magnitude of this EOT peak (**R3**) decreases as C_{Co} increases to 30 %V. When C_{Co} > 30 %V, $T(\lambda)$ at **R3** remains almost a constant with C_{Co}. The change in transmission dips **AR1** and **AR2** are less significant. However, a close investigation shows that even the magnitude and position of these three features are changing with C_{Co}, the overall transmission spectra shapes are similar regardless of the composition.

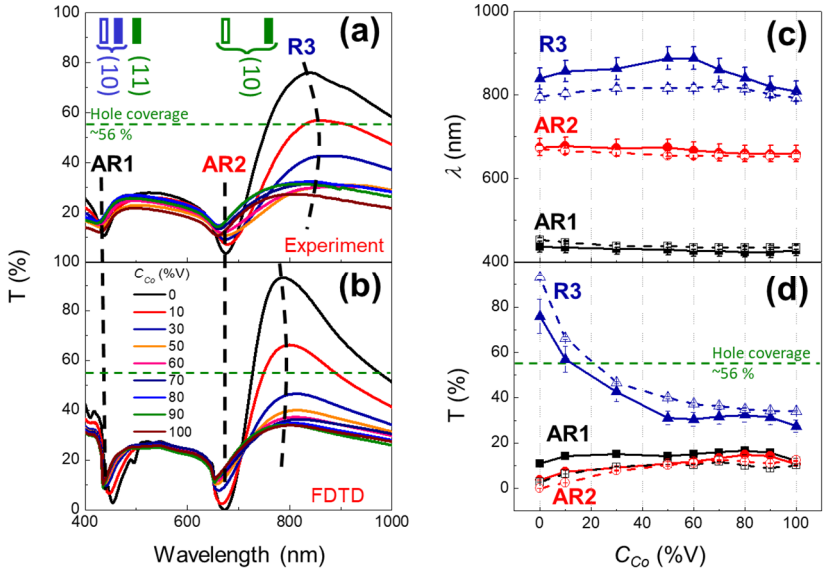

Figure 3.3. (a) The experimental and (b) FDTD calculated transmission spectra $T(\lambda)$ of CNAs. The prominent features of optical transmission (**AR1**, **AR2**, and **R3**) were denoted. The vertical blocks indicate the positions of resonances (solid symbol) and anti-resonance (open symbol) at the film-glass interface (green) and film-air interface (blue), calculated from equation (3.1) and (3.2). (c) The plots of experimental (solid symbol, solid line) and FDTD calculated (open symbol, dash line) λ_1^T, λ_2^T, and λ_3^T *versus* C_{Co}. (d) The plots of experimental (solid symbol, solid line) and FDTD calculated (open symbol, dash line) transmission magnitude at **AR1**, **AR2**, and **R3** *versus* C_{Co}.

These features are resulted from the coupling effects of light at different material interfaces and surface plasmonic (SP) wave.[7, 99] Thanks to the present of arrays of air hole on the film, it compensates the momentum mismatches of a free-space photon and an SP

wave at the metal-dielectric interfaces,[59] produces the transmission resonance or anti-resonance at wavelengths λ_R and λ_{AR}. For hexagonal crystalline structure, at the transmission peak λ_R, the surface plasmon polariton Bloch wave condition is satisfied and λ_R can be estimated by the following equation,[59, 100]

$$\lambda_R = a_0\left[\frac{4}{3}(i^2+ij+j^2)\right]^{-\frac{1}{2}}\sqrt{\frac{\varepsilon_1\varepsilon_d}{\varepsilon_1+\varepsilon_d}}. \quad (3.1)$$

At the transmission dip λ_{AR}, the Wood – Rayleigh anomaly condition is satisfied and λ_{AR} can be approximated as,[101]

$$\lambda_{AR} = a_0\left[\frac{4}{3}(i^2+ij+j^2)\right]^{-\frac{1}{2}}\sqrt{\varepsilon_d}, \quad (3.2)$$

where the integers *i* and *j* denote the order of the SP resonances, ε_1 and ε_d are the real parts of the dielectric constants of the metal and the dielectric, respectively, and $a_0 = D = 500$ nm is the period of the CNAs. From these equations, the positions of λ_R and λ_{AR} were calculated for the case of $\varepsilon_d = 1$ (air) and ε_d of glass, and the results are marked by blocks in **Figure 3.3a**. The vertical blocks indicate the positions of resonances (solid symbol) and anti-resonance (AR) (open symbol) at the film-glass interface (green) and film-air interface (blue). Clearly, the two transmission dips at $\lambda_1^T \approx 440$ nm (**AR1**) and $\lambda_2^T \approx 660$ nm (**AR2**) correspond to the AR (or Wood's anomalies) (1,0) modes of film-air and film-glass interfaces, respectively, while the transmission peak at $\lambda_3^T \approx 850$ nm (**R3**) is the (1,0) resonance mode at film-glass interface. In addition, the local transmission peak between

AR1 and **AR2** could also be assigned as the higher mode resonance (1,1) at film-glass interface.

The FDTD calculated optical transmission spectra of CNAs are shown in **Figure 3.3b** and they agree qualitatively well with the experimental results. Similar three distinct features, a transmission peak **R3** and two transmission dips **AR1**, **AR2**, are also found. The EOT peak **R3** is seen the largest for CNA_0 and it reduces gradually when more Co is added to CNAs. The transmission peak **R3** is observed at $\lambda_3^T \approx 800$ nm, which is slightly blue-shifted in compared to the experimental one. In addition, the two transmission dips **AR1** and **AR2** are observed at similar wavelengths $\lambda_1^T \approx 440$ nm and $\lambda_2^T \approx 660$ nm in compare to the features from experimental spectra. For better comparison between experiment and FDTD calculations, the wavelength positions λ_1^T, λ_2^T, and λ_3^T and transmission magnitude (T) of **AR1**, **AR2**, and **R3** are summarized and plotted in **Figure 3.3c** and **d**. Clearly, λ_1^T and λ_2^T from **Figure 3.3a** and **b** are overlapped and show the consistency between experiment and FDTD calculation. In addition, λ_1^T and λ_2^T from both experiment and calculation show insignificant changes when C_{Co} increases, which follows well with the Wood – Rayleigh anomaly theory since the Wood's anomalies are purely geometric and the corresponding wavelength position does not depend on the optical permittivity of metal film as stated in equation (3.2).[102] The EOT wavelength λ_3^T, though it follows similar trend against C_{Co}, shows larger discrepancy between experiment and FDTD calculation. This can be explained by the fact that λ_3^T has been demonstrated to be dependent on several

parameters other than ε_m as stated in equation (3.1), such as film thickness,[103-104] hole diameter,[104] hole shape,[105] etc., which makes the **R3** peak to be more sensitive to the imperfection of nanostructure than that of **AR1** and **AR2**.

The experimental and FDTD calculated transmission at **AR1**, **AR2**, and **R3** versus C_{Co} shown in **Figure 3.3d** also show similar trends. In particular, at the EOT peak **R3**, the transmission rises slowly when C_{Co} decreases from 100 %V (pure Co) to 50 %V and increases rapidly when C_{Co} decreases from 50 %V to 0 %V (pure Ag). This shows that when C_{Co} is between 100 %V to 50 %V, there is negligible EOT effect, and the plasmonic effect occurs only when $C_{Co} \leq 50$ %V. This result agrees with the negligible crystal formation of Ag, observed in **Figure 3.2b** when $C_{Co} \geq 50$ %V. On the other hand, at the dips **AR1** and **AR2**, transmissions were observed to be reduced when less Co was added to the composite film. In CNA_{100}, only a weak transmission peak **R3** is induced. This is due to the large absorption of Co film, which can be seen in large imaginary part ε_2 of optical permittivity of Co (from experiment ellipsometry data, **Figure A1** in **Appendix A**). By adding less Co (*i.e.*, C_{Co} decreases), ε_2 decreases, while the real part ε_1 of optical permittivity becomes more negative and approaches to that of the pure Ag, which allows surface plasmon polariton (SPP) propagates a greater length at metal-dielectric interface in compare to pure Co case (C_{Co} = 100 %V)[106] and eventually boosts up the transmission at **R3**. Therefore, the plasmonic properties of CNAs are improved significantly at low C_{Co}. In addition, stronger plasmonic properties in composite materials also enhances the local electric field at the Wood's anomalies **AR1** and **AR2**, resulting in stronger

absorption/deeper dips in transmission spectra. Similar trends can be observed in the FDTD results (dash lines), and the composition dependent behaviors of transmission at **AR1**, **AR2**, and **R3** agree very well with the experimental results, which shows the stronger plasmonic properties when the composite film contains more Ag. Furthermore, the time-averaged local intensity maps of different CNAs at C_{Co} = 0, 10, 30, 50, and 100%V at λ_1^T, λ_2^T, and λ_3^T calculated by FDTD have been extracted and are presented in **Figure 3.4a-b**. In all samples, strong local electrical field at **AR1** and **AR2** can be observed around the rim of the nanoholes at the film-air and film-glass interfaces, respectively, as show in **Figure 3.4a** (**AR1** and **AR2** columns). **Figure 3.4a** (**R3** column) illustrates the enhanced asymmetric electric field around the walls and rims of the nanoholes in all the samples at **R3**, which shows that the SP waves at both film-air and film-glass interfaces of the CNAs are coupled and the light from the incident side is re-radiated from other side, which is the origin of EOT.[98] Those observations confirm the prediction of the origins of dips **AR1**, **AR2**, and peaks **R3** as shown in equation (3.1) and (3.2). In addition, the ratio of the local electric fields E to the incident field E_0 ($|E/E_0|$) of CNAs for different C_{Co} at the walls of the holes (as indicated by white dotted lines in **Figure 3.4a**) are summarized in **Figure 3.4c-g**. As the C_{Co} in the CNA decreases, the local field ratio at **AR1**, **AR2**, and **R3** increase greatly. This observation confirms our statement about the improved plasmonic properties by the present of more Ag in the CMP nanostructures.

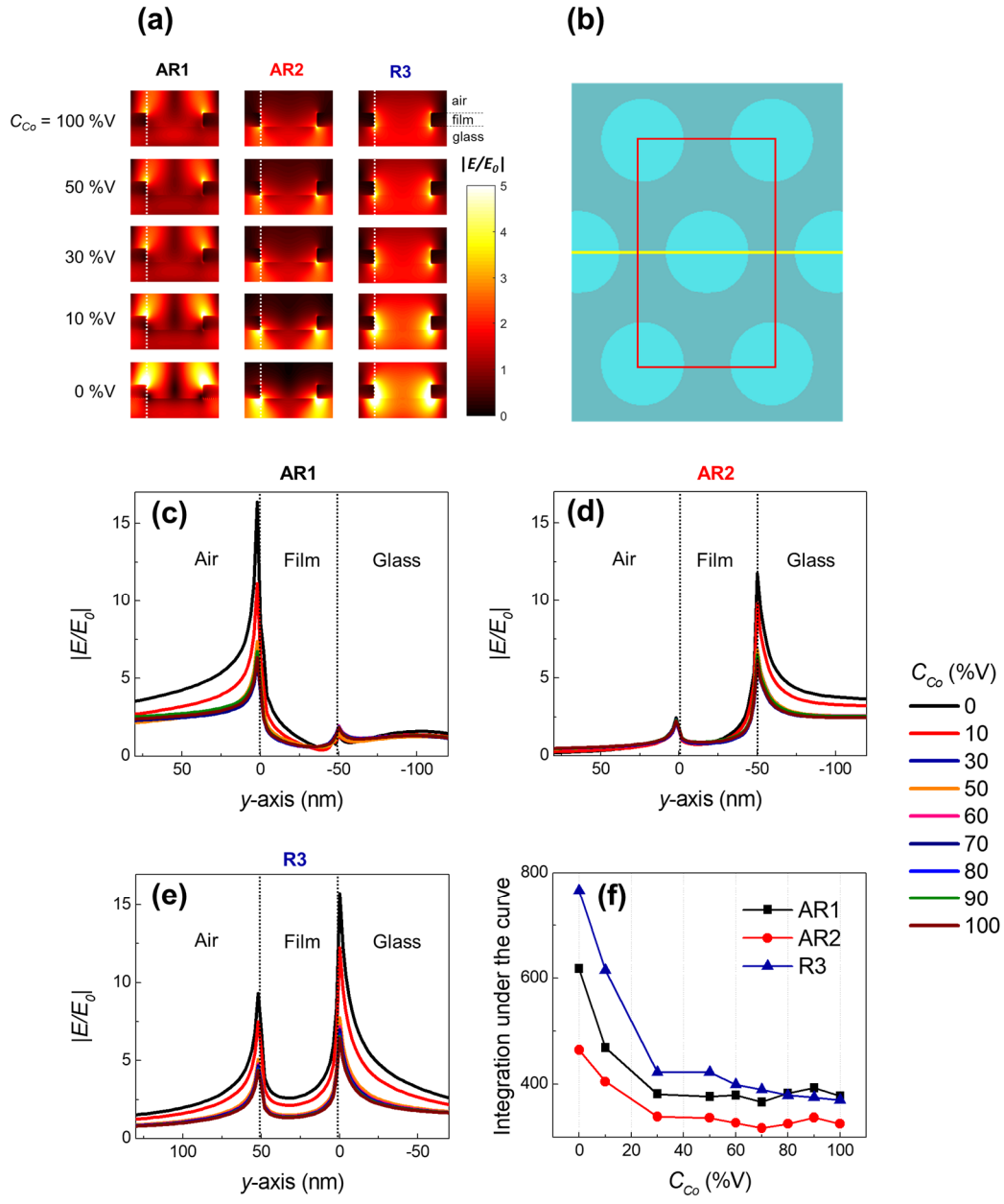

Figure 3.4. (a) Time-averaged intensity maps of the FDTD calculated local electric field at the cross-section plane denoted by the yellow line in (b), with different C_{Co} (%V). The light incidents from top to bottom. The red box in figure (b) denotes the

rectangular unit cell for FDTD calculations. (c-e) Relative electric field $|E/E_0|$ at the walls of nanoholes of CNAs with different C_{Co} (%V). The extracted positions are indicated by the white lines in the maps of (a). (f) The plots of integrated $|E/E_0|$ under the curve of figures (c-e) versus C_{Co}. The dash lines in (c-e) indicate the locations of glass-film and film-air interfaces.

3.4. Magneto-optical Properties of CNAs

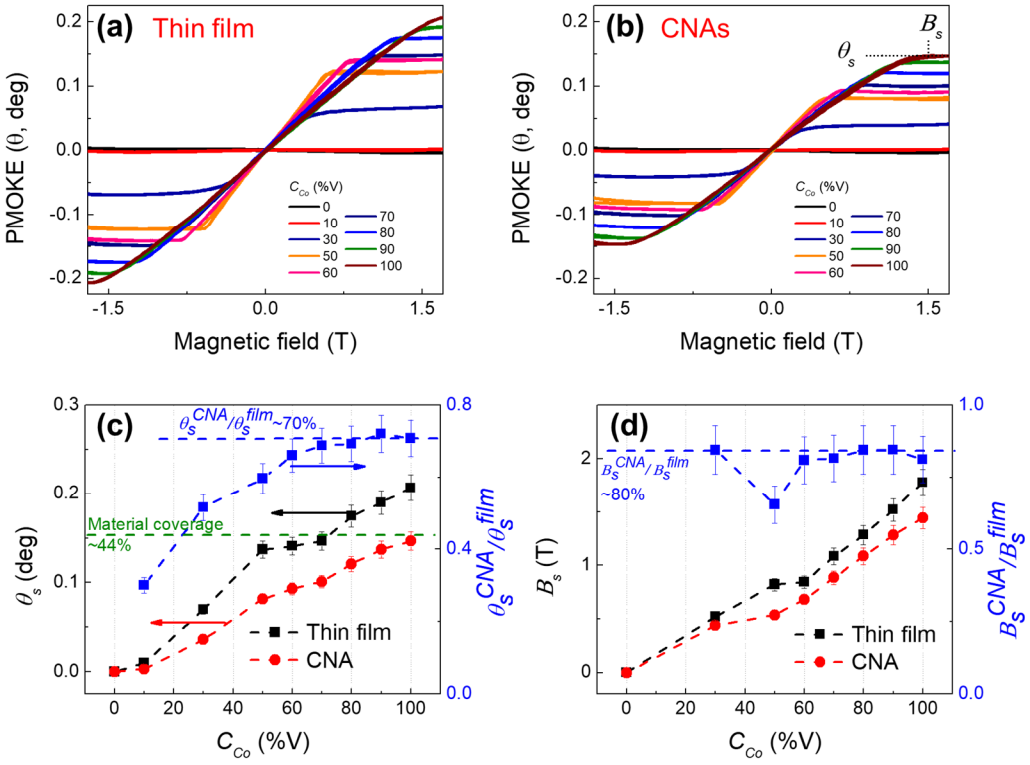

Figure 3.5. PMOKE of (a) composite thin films and (b) CNAs with different C_{Co}. (c) Saturated PMOKE (θ_s) and (d) saturation field (B_s) of composite thin film (black) and CNAs (red) for different C_{Co}.

Figure 3.5a-b show the PMOKE hysteresis curves (measured at λ = 632 nm) for the composite thin films and CNAs, respectively. For all samples, the hysteresis curves exhibit a typical hard-axis behavior with almost no remanence and saturation fields are at very strong magnetic fields (for instance, at 1.7 T for thin film with C_{Co} = 100 %V), which confirms the out-of-plane hard axis of these samples. However, the saturation field (B_s) and saturation PMOKE (θ_s) versus C_{Co} are significantly different for thin film and CNA samples as shown in **Figure 3.5c-d**. As presented in **Figure 3.5c**, for thin film sample, the sample with C_{Co} = 100 %V produces largest θ_s, and θ_s drops almost linearly with C_{Co} to null when C_{Co} = 0 %V. Similar trend is observed for CNA samples, but θ_s in CNAs is smaller than that in corresponding thin film samples due to the removal of magnetic materials. In principle, θ_s is proportional to ($\propto$) M_s, the saturation magnetization of the samples. In general, $M_s \propto \Theta uA$, where Θ is the coverage of magnetic layer on surface, A is total illuminated surface area of laser beam in MOKE measurement and u is the surface density of magnetic moment, *i.e.*, $\theta_s \propto \Theta$. If we assume that u is the same for thin film and CNA samples, then $\theta_s^{CNA}/\theta_s^{film} = \Theta_{CNA}$ should be a constant. **Figure 3.5c** also plots the experimental ratio $\theta_s^{CNA}/\theta_s^{film}$ (blue). Interestingly, even though the materials coverage is only about ~ 44 % for CNAs, the ratio $\theta_s^{CNA}/\theta_s^{film}$ are about 70 % for samples with C_{Co} > 70 %V. This ratio decreases gradually to 25 % for samples with C_{Co} = 10 %V. Clearly the $\theta_s^{CNA}/\theta_s^{film}$ ratio *versus* C_{Co} is not a constant, which might come from several possible reasons. If we consider a simple Ising model for this composite ferromagnetic/noble metal,

the introduction of hole arrays could vary the magnetic interaction at high C_{Co}, which can change the saturation magnetization of CNAs non-linearly [107] and eventually change θ_S^{CNA}. Another possibility is that the composition changes can modify the surface penetration of probing laser, which can affect both the θ_S^{CNA} and θ_S^{film}. Further theoretical efforts need to be carried out.

In addition to the saturated PMOKE, the saturation field (B_s) of CNAs and thin films are studied in **Figure 3.5d**. Basically, B_s is magnitude of applied magnetic field where the sample is fully magnetized and magnetization is aligned with external magnetic field. We first consider the composition dependences of these samples. As mentioned before, for pure Co thin film (C_{Co} = 100 %V), only a slightly remanence can be seen at very strong magnetic field of 1.7 T, due to its out-of-plane hard axis characteristic. When more Ag is added into the composite materials, the B_s decreases significantly to only about 0.5 T for thin film with C_{Co} = 30 %V. This observation implies that the introduction of Ag induces the rise to the out-of-plane components. On the other hand, the introduction of hole arrays also reduces the B_s, as seen in **Figure 3.5d**, where the B_s of CNAs is consistently about 80 % of the B_s of composite thin films with the same C_{Co}. This observation is consistent to other work of perforated hole arrays on pure Co thin film,[59] and is explained due to the rise of out-of-plane component induced by local dipolar fields which introduced by the hole edge.[59]

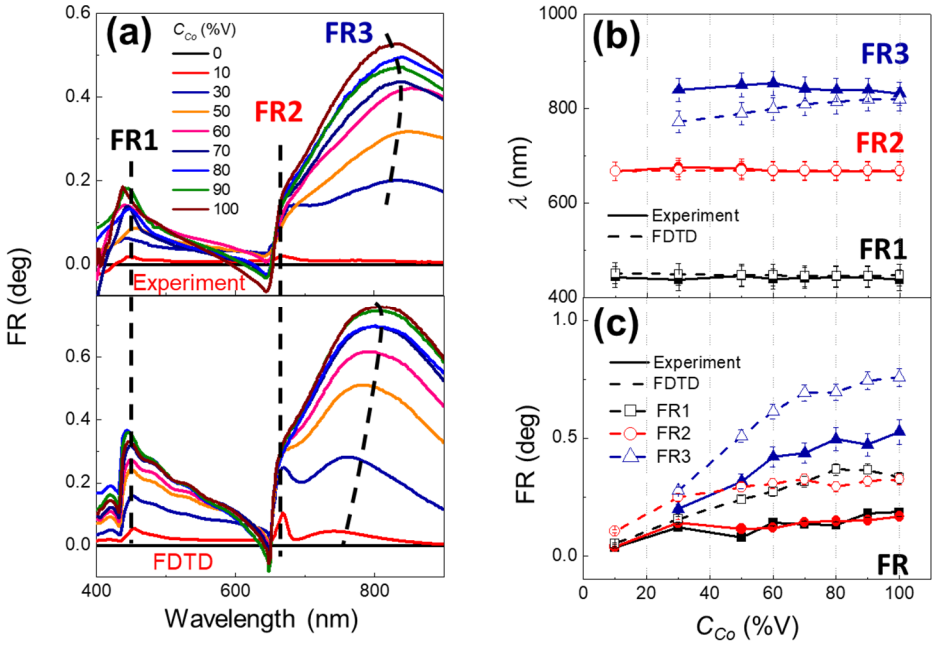

Figure 3.6. (a) The experimental and FDTD calculated FR spectra of CNAs. The prominent features of FR (**FR1**, **FR2**, and **FR3**) were indicated. (b) The plots of experimental (solid symbol, solid line) and FDTD calculated (open symbol, dash line) λ_1^F, λ_2^F, and λ_3^F of **FR1**, **FR2**, **FR3** *versus* C_{Co}. (c) The plots of experimental (solid symbol, solid line) and FDTD calculated (open symbol, dash line) FR at **FR1**, **FR2**, **FR3** *versus* C_{Co}.

As shown above, introducing nanohole arrays and adjusting the composition significantly modify the magnetic property as well as MO response of composite thin films. In order to have better understanding about this influence, the composition dependence FR of CNAs has been studied. **Figure 3.6a** presents the experimental and FDTD calculated FR spectra of CNAs. In both results, three prominent features can be observed as indicated

in **Figure 3.6a**: a peak **FR1** at $\lambda_1^{FR} \approx 440$ nm, a kink **FR2** at $\lambda_2^{FR} \approx 660$ nm, and a peak **FR3** at $\lambda_3^{FR} \approx 850$ nm. All three features show strong composition dependence. As C_{Co} decreasing, the overall magneto-optical effects of CNAs reduce as seen in the drop of FR magnitude, and the shape of spectra changes significantly. Close to the EOT wavelength λ_3^T, **FR3** is a broad and most distinct FR peak. To better understanding the C_{Co} dependent FR behavior, experimental and FDTD calculated positions and magnitudes of **FR1**, **FR2**, and **FR3** are summarized in **Figure 3.6b-c**. The positions of **FR1** and **FR2** are relatively unchanged regardless to the composition of CNAs. In term of FR magnitude, the composition dependence generally shows an increase of FR when C_{Co} increases in any FR peak (**Figure 3.6c**). When C_{Co} decreases, the location of **FR3** peak almost remains unchanged but its magnitude decreases significantly. Similar trends can be seen in the **FR1**'s peak positions and magnitude. However, **FR2** shows somewhat different behaviors: at high C_{Co} ($\geq$ 50 %V), the peak **FR2** is buried in the background and can be consider as a kink in the FR spectra. When C_{Co} < 50 %V, **FR2** starts to become a noticeable peak in FR spectra, especially at CNA_{10}. The experimental and FDTD calculated positions of FR features are also in general consistent to each other. However, there still exists some deviations, for example, the positions of **FR3** and the magnitudes of the experimental and FDTD calculated FR. These deviations might come from the fact that the imperfections of experiment structures (such as hole diameter, thickness, roughness of surface, *etc*.) have not been considered in the FDTD calculation.

Those behaviors of FR features as shown are closely related to the plasmonic behaviors of the CNA samples. Positions of the two features, **FR1** and **FR2**, occur at exact locations of two transmission dips **AR1** ($\lambda_1^T \approx 440$ nm) and **AR2** ($\lambda_1^T \approx 660$ nm), which corresponds to the AR (1,0) mode at the film-air and film-glass interfaces, respectively. Thus it is expected that the origin of these weakly enhanced FR features is from the enhanced electric fields induced by Wood's anomalies at the rims of the nanoholes as well as the long interaction time between light and magnetic layer, which has been demonstrated in an identical structure of Ni and Co nanohole arrays.[45, 70] In addition, **FR1** and **FR2** positions are observed to be independent to the C_{Co} (**Figure 3.6b**), since **AR1** and **AR2** positions does not depend on the composition of CNAs (as presented in the last section). On the other hand, the magnitude of **FR3** in CNA_{100} is the largest, and its position is coincidently in the vicinity of **R3**, the EOT peak of CNA_0. Indeed, peak **FR3** is a local FR peak brought by large transmission at the enhanced transmission peak **R3**. Since FR and optical transmittance are indirectly proportionally related,[74] the strong transmission peak **R3** at λ_3^T, which is due to SPP resonance (1,0) at Co-glass interface, suppresses the FR magnitude at λ_3^T and creates a local maximum **FR3** at slightly blue-shifted wavelength λ_3^{FR}. The origin of peak **FR3** has been described in more details in our previous work.[45]

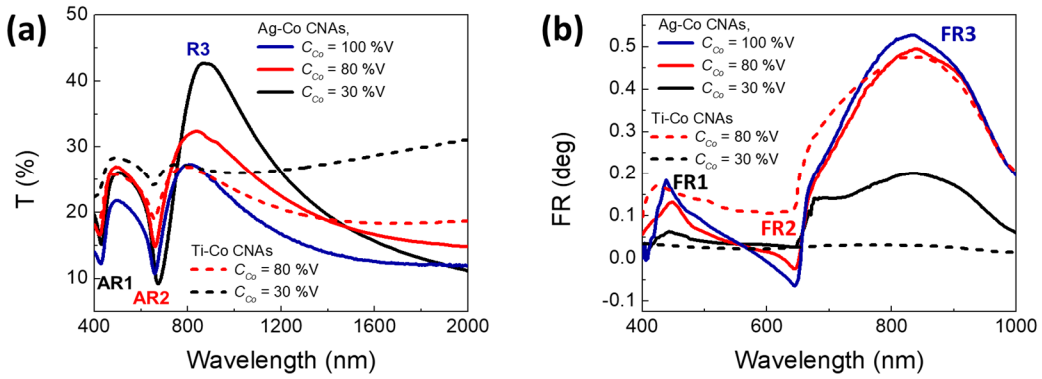

Figure 3.7. (a) Optical transmission spectra and (b) FR spectra of Ag-Co and Ti-Co CNAs with C_{Co} = 30 and 80 %V.

To isolate the plasmonic effect of Ag on MO properties, FR spectra and $T(\lambda)$ spectra of control samples of Ti-Co CNA samples with C_{Co} = 80 %V and 30 %V were further investigated. Ti is well known as a poor plasmonic material, and Ti-Co composite control sample can be useful to identify the plasmonic effects from Ag component in Ag-Co samples. The fabrication conditions and measurement conditions of Ti-Co CNA samples were kept identical to the ones of Ag-Co composite samples. The experimental results are summarized in **Figure 3.7**.

As can be seen in **Figure 3.7a**, the shapes of optical transmission spectra of Ti-Co CNAs are similar to that of Ag-Co CNAs, with three prominent features **AR1**, **AR2**, and **R3** can be found. However, the transmissions at these peaks/dips are significantly different. In Ag-Co CNA samples, the more Ag is added, the stronger the plasmonic properties of samples are as noticed by stronger transmission at extraordinary optical transmission

(EOT) **R3** peak. On the other hand, for the Ti-Co CNA samples, the optical transmission at R3 remains unchanged while more Ti are added. Also, the peak **R3** at 30 %V is blue shifted with respect to the 80 %V. The dips **AR1** and **AR2** are very shallow for the 30 %V array indicating that the plasmonics of Ti-Co composite film is poor. This observation implies that by adding more Ag into the composite nanoholes, stronger plasmonic effect will occur.

The plasmonic effect of Ag component to the magneto-optical properties can be furtherly examined by comparing the FR spectra of Ag-Co and Ti-Co CNAs (**Figure 3.7b**). For C_{Co} = 80 %V where Co is main component, the FR spectra of Ti-Co CNAs is similar to the one of Ag-Co CNAs, with three features can be seen: **FR1**, **FR2**, and **FR3**. The FR magnitude at **FR3** is equal for both samples, as the results of the same amount of magnetic materials in both films. One can only spot the major difference in FR spectra at the kink **FR2**. Nevertheless, for C_{Co} = 30 %V, the plasmonic properties of Ag component in Ag-Co CNAs show a very strong influence on the magneto-optics properties. While the FR of Ti-Co sample is significantly small, Ag-Co sample shows a clear FR spectrum with distinct feature **FR1**, **FR2**, and **FR3**. Clearly, this enhancement is closely related to the plasmonic properties which is brought by the Ag component.

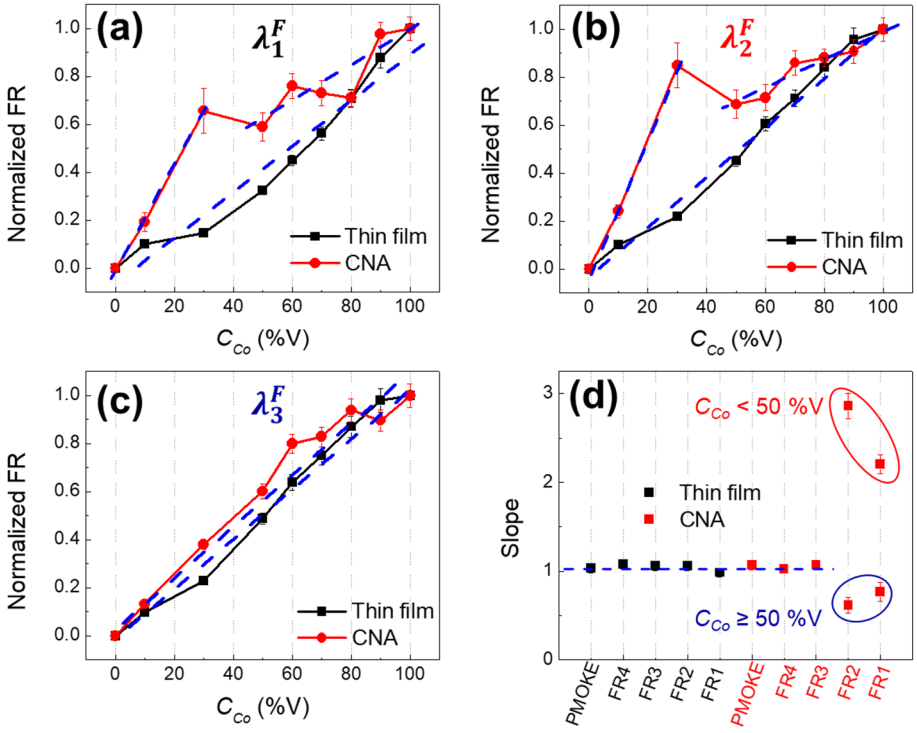

Figure 3.8. (a-c) Normalized FR of CNAs and composite thin film at λ_1^F, λ_2^F, and λ_3^F *versus* C_{Co}. (d) The plot of the slopes of normalized FR or PMOKE *versus* C_{Co}. The dashed curves show linear fitting at different wavelengths.

The influences of C_{Co} and introduction of nanohole arrays to MO responses are studied further by looking at wavelength dependent FR of thin film and CNA samples, and compare the responses at resonant and non-resonant wavelengths. **Figure 3.8** presents FR spectra of composite thin films as a function of C_{Co}. In contrast to CNAs, FRs in all thin film samples increase monotonically with C_{Co} in the wavelength range $\lambda = 400 - 900$ nm, and no prominent feature can be found. The composition dependent FR of thin film and

CNAs (normalized for FR of samples with C_{Co} = 100 %V) at λ_1^F, λ_2^F, and λ_3^F are illustrated in **Figure 3.8a-c**, respectively. At a glance, these composition dependent curves of CNAs at non-resonant wavelength are similar to thin film's curves. Though, significant differences can be observed at CNA's curves at resonant wavelengths, *i.e.* at **FR1** and **FR2**. In **Figure 3.8a-c**, for thin film samples (black curve), a linear relation can be observed regardless of wavelength. However, for CNAs (red curve), there are significant differences between the rise rate of FR when C_{Co} increases from 0 %V to 30 %V and 50 %V to 100 %V at **FR1** and **FR2** as seen in **Figure 3.8a** and **b**, respectively. In particular, FR increases rapidly when Ag is still a major composition in the film (C_{Co} = 0 to 30 %V), then increases much slower when C_{Co} = 50 to 100 %V. On the other hand, at FR3 of CNAs, we only observe a conventional linearly increase of FR against C_{Co} (**Figure 3.8c**). For a better comparison, the normalized FR of CNAs and composite thin film versus C_{Co} at λ_1^F, λ_2^F, λ_3^F, and at a non-resonant wavelength λ_4^F = 750 nm (denotes by **FR4**) are fitted with a linear function, respectively. The slopes of these fittings are summarized in **Figure 3.8d**. Except **FR1** and **FR2** of CNAs, all other fittings give the slopes ~ 1, as expected. However, FRs at the Wood's anomalies, **FR1** and **FR2**, shows much higher slopes (2.21 and 2.86) when C_{Co} < 50 %V and smaller slopes (0.77 and 0.62 < 1) when $C_{Co} \geq$ 50 %V. This observation can be explained by the enhancement of local electric field due to the plasmonic effect, which comes from high ratio of Ag component in CNAs. **Figure 3.4** shows the magnitude of FDTD calculated local electric field at **AR1** and **AR2**. When C_{Co} < 50 %V, the plasmonic effect of CNAs is still significantly strong. The FR enhancement due to local

electric field, adds to the increase of FR due to amount of magnetic material when C_{Co} increases, gives a faster rise for FR at Wood's anomalies than that at other non-resonant wavelengths. The difference for **FR1** and **FR2** are due to localized plasmonic effect, while propagation plasmon has less effect. This fast rise was not observed at **FR3**, because the fact that this feature is not raised directly from enhanced electrical field as that of the transmission **R3**, as discussed previously. Nevertheless, when $C_{Co} \geq 50$ %V, the plasmonic effect does not change as much as seen in **Figure 3.4f**, therefore the increases of FR in this range come mostly from the increase of magnetic material component in the CMP.

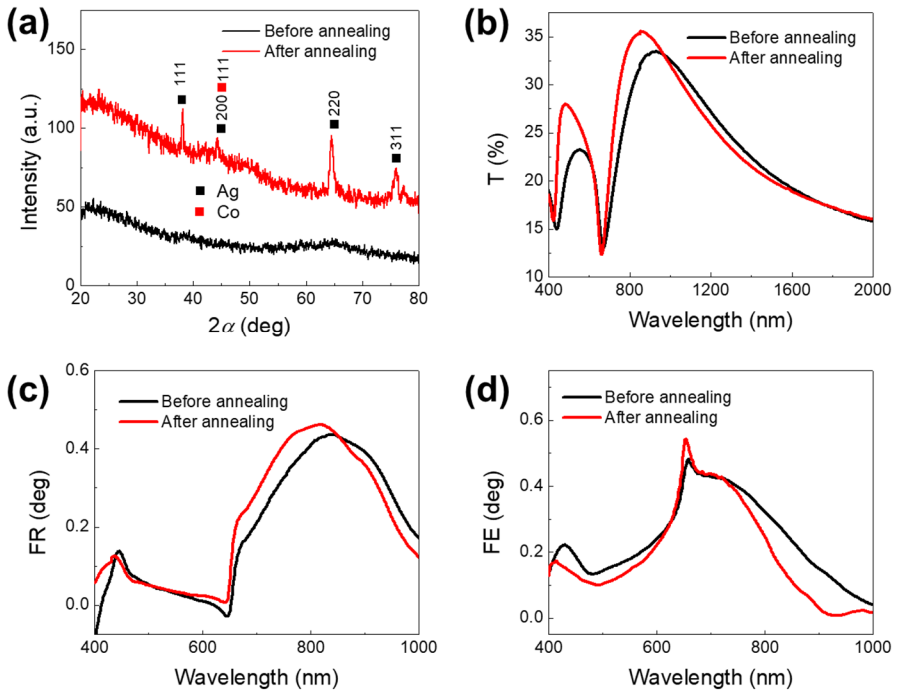

Figure 3.9. (a) XRD profile, (b) optical transmission spectra, (c) FR spectra, and (d) FE spectra of CNA_{60} sample before and after annealing.

Note that Ag and Co are insoluble in each other in the solid and liquid phases and they cannot rigorously form a binary alloy.[44] Therefore, in this work, we focus on a mixture rather than an alloy between Ag and Co. Nevertheless, the optical and MO properties of CNA samples can be modified and their MOP effect can be further enhanced by varying a sample's crystallinity, *e.g.*, annealing the sample under high temperature. To demonstrate this point, a representative CNA_{60} sample was annealed in N_2 atmosphere at 500 °C in 2 h. The XRD profile, optical transmission, FR, and FE spectra of the sample before and after the annealing process are summarized in **Figure 3.9**. From **Figure 3.9a**, while no peak can be found in XRD profile of as-deposited film, several peaks corresponding to crystalline planes of both Ag and Co can be found in the annealed sample, which are caused by the segregation of Ag and Co nanocrystals.[44] The mean crystal sizes of Ag and Co in an annealed CNA_{60} sample extracted from Scherrer's equation are approximately 28 nm and 26 nm, respectively. Due to the changes of the crystallinity and redistribution of Ag and Co in the composite film, the optical and MO properties of CNA are also modified. **Figure 3.9b** shows the transmission spectra of the annealed sample. Both the (1,0) and (1,1) EOT resonant peaks at the film-glass interface are blue-shifted. This change might come from the relocation of Ag to the film-glass interface. More significantly, the change in plasmonic properties also directly influences FR and FE spectra. As shown in **Figure 3.9b** and **c**, a stronger FR spectrum at **FR3** peak and a stronger and sharper **FE2** peak are observed in the annealed sample. This observation suggests that the crystallinity as well as the redistribution of components also plays an important role in modifying the optical and MO

properties of the composite CNA structures. Further systematic experimental efforts need to be carried out for a complete conclusion.

3.5. Composite Versus Multilayer

In order to isolate the advantages and disadvantages of the composite-based MOP structures over these of the conventional multilayer ones, in this part, MOP performances of the Ag-Co CNAs and Ag/Co multilayer nanohole arrays are directly compared. In particular, we compare the FR spectra of three nanohole array samples made from Ag-Co composite (60 %V of Co, with 30 nm of Co and 20 nm of Ag), Ag-Co multilayer (30 nm of Co and 20 nm of Ag), and pure Co (50 nm). We note that all these samples have a similar total thickness of 50 nm for a fair comparison.

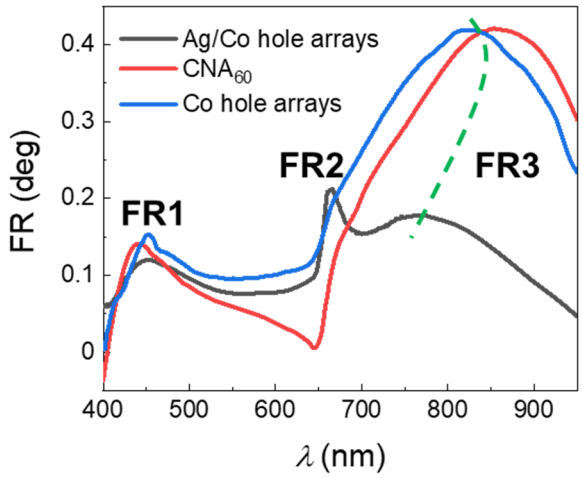

Figure 3.10. FR spectra of a CNA_{60}, a double-layer Ag-Co nanohole array, and a single layer Co nanohole array. All these samples have a similar total thickness of 50 nm.

The FR spectra of these three samples all have three distinct features: **FR1** (from (1,0) AR mode at metal-air interface), **FR2** (from (1,0) AR mode at metal-glass interface), and **FR3** as indicated in **Figure 3.10**. Noticeably, the spectral shape of CNA_{60} and Co nanohole array (red and blue curves, respectively) share various resemblances: due to the strong absorbance of Co and Ag-Co composite in comparison to Ag (see **Appendix A**), the local electric field at resonance and AR modes are relatively weak, and therefore the **FR1** appears as a blunt peak with a large spectral width, peak **FR2** can only be observed as a kink and is buried in the background of FR spectra, while **FR3** appears to be the strongest peak in the observing wavelength range.

On the other hand, by combining the bottom layer of 20-nm Ag with a top-layer of 30-nm Co to obtain the Ag-Co double-layer hole arrays, the **FR2** peak was enhanced strongly with a narrow resonant due to stronger local electric field at the Ag-glass interface. In addition, an EOT peak appears, suppresses **FR3** and pushes it to a shorter wavelength location (a detail explanation for this blue-shift of **FR3** can be found in Ref. [45, 83]). Nevertheless, the peak **FR1** is relatively unchanged in both magnitude and line width in comparison to these of Co and composite nanohole arrays, due to this peak is supported by AR mode at Co-air interface (which also does not well-support SPR). We note that Ag-Co double-layer and Ag-Co-Ag triple-layer nanohole arrays have been comprehensively studied, more detail can be found in Ref. [83].

Two major differences between MO properties of the composite and multilayer samples that we can observe: (i) the maximum of FR magnitude of composite sample is

much larger than that of multilayer one, and is comparable to that of pure Co sample even though CNA contains much less magnetic material; and (ii) the plasmonic properties is much stronger in the multilayer sample than in the composite sample, especially at the Ag-dielectric interface, as the resonance FR peak **FR2** of the multilayer sample appears to be much narrower and stronger.

From these observations, two rules for device design can be taken home: (i) for the application that requires large FR and high optical transmission (such as optical rotator, etc.), composite is a promising material of choice; and (ii) for the application that requires sharp and strong resonance (optical sensor, band-pass filter, etc.), multilayer configuration is more suitable.

3.6. Conclusions

CNAs with different Ag and Co compositions were realized by SNL and electron beam co-deposition. Optical properties of CNAs with different C_{Co} have been studied throughout, which shows strong plasmonic properties in samples with high content of Ag. By altering the relative ratio of Ag and Co in the samples, the magnetic and optical properties could be varied, which could be used to improve the MO performances of CNAs. Our experimental and FDTD calculated results have demonstrated that when C_{Co} = 30 %V, a CNA can yield better MO performance than a Ti-Co composite nanohole arrays sample, thanks to the compromise between the strong MO properties from Co component and strong plasmonic properties and large transmission provided by Ag component, or vice versa. Therefore, in

addition to the geometrical parameters (size, shape, etc.) and arrangement of the structure, the composition of MOP composite can be adjusted to obtain optimized MO properties. This tunability is promising for the designs and applications of future MOP materials and structures. This also provides new ideas on replacing the multilayers of noble metal/ferromagnetic by composite materials in many current MO devices, such as chiroptical devices, MOSPR sensors, etc., to achieve a better device performance.

3.7. Experimental Sections

Materials: Deionized water (18 MΩ.cm) was used for all experiments. PS nanospheres (Polysciences Inc., D = 500 nm) and ethanol (Sigma-Aldrich, 98%) were used to create the nanosphere monolayers. Silver (99.999%), cobalt (99.95%) and titanium (99.995%) from Kurt. J Lesker Company were utilized for e-beam codeposition.

Morphology and composition characterization: The morphologies of CNAs were characterized by an AFM (Park NX10), and all the AFM images were analyzed by XEI - Image Processing and Analysis Software. The compositions of thin film samples were characterized by an EDS of a field emission scanning electron microscopy (SEM, FEI Inspect F). Here we assume that the corresponding CNA samples and thin film samples have the same composition since they were prepared simultaneously. The crystallinities of the composite materials were investigated by XRD with a PANalytical X'Pert PRO MRD X-ray diffractometer at a fixed incident angle of 0.5°.

Optical and magneto-optical characterization: The spectral ellipsometry of composite thin films over the visible to near infrared wavelength range were studied by a spectroscopic ellipsometer (M-2000, J.A Woollam Co., Inc.), with four incident angles of 65°, 70°, 75°, and 80°, respectively. The PMOKE hysteresis curves of samples were collected by a home-built mirror-based PMOKE spectroscopy (λ = 632 nm). Details of experimental setup and data analysis can be found in Ref. [108].

FDTD calculations: To better understand the optical and MO properties of the samples, FDTD calculations were carried out using a commercial software (Lumerical FDTD Solutions).[109] The extracted film thickness (t_C), hole diameter (d), and period from AFM images were used to build the FDTD model. The FDTD simulation domain was set to cover a rectangular unit cell (red box, inset of **Figure 3.1a**). Periodic boundary conditions were used to present the two-dimensional periodicity of CNAs, and perfect matched layer (PML) boundary conditions were applied on the top and bottom sides of the rectangular cuboid simulation region. The FDTD mesh size was set as 2 nm × 2 nm × 2 nm to compromise between the calculation time and the convergence of the calculations. A frequency-domain field and power monitor was placed to collect the transmitted light, the **E** and **H** components of the electromagnetic field. The FR was calculated according to Ref. [109-110]. The refractive index of air was fixed to be 1, and the dispersive refractive index of glass was taken from Ref. [111]. The complex optical permittivities $\varepsilon = \varepsilon_1 + i\varepsilon_2$ of Ag, Co, and composite material were experimentally determined from the spectral ellipsometry data of

corresponding thin films (**Figure A1** in **Appendix A**). The MO constants used for FDTD calculations were extracted from the experimental Co thin films and composite thin films data, measured by the FR spectroscopy (**Figure A2** in **Appendix A**).[4]

CHAPTER 4

MAGNETO-PLASMONICS COMPOSITE NANO-TRIANGLE ARRAYS

In contrast to **Chapter 3** where the MOP properties of a SPP-supported nano-system (nanohole arrays) are investigated, in **Chapter 4** we explore MOP properties of a LSPR-supported nano-system, *i.e.,* composite nano-triangle arrays.

4.1. Introduction

Since the MO effect comes from the spin orbit coupling in ferromagnetic metals and can be tuned by the excitation of localized surface plasmon resonance (LSPR),[112-113] several studies have exploited the LSPR induced by nanoparticles (NP) whose constituent components made by noble metals to enhance MO effects such as in multilayer core-shell nanospheres,[50, 53-56] multilayer NPs,[48, 114-117] NP clusters,[118-119] split-ring structures,[120-121] etc. In these works, multilayer structures were mostly used. Clearly, an alternative material system is a composite material. The composite of ferromagnetic/plasmonic metal materials could simultaneously have both magnetic and plasmonic properties, which could allow another dimension in the design of MOP systems. So far, there has been a limited amount of work in composite MOP thin films[44, 58, 91-94] and nanostructures.[112] For instance, Yan et al. studied Ag/Co composite dimer nanodot arrays, where they demonstrated the

relationship between MO activity and LSPR excitation. This study attempted to use the composite MOP materials, however, the enhancement of MO activity in comparison to pure ferromagnetic structure was not clearly observed.[112] Other studies[44, 58, 91-94] have focus mainly on thin film properties. Thus, it would be promising to consider the optical and MO properties as well as potential applications of nanostructures realized with composite MOP materials. Recently, we have demonstrated enhanced MOP performance in Ag-Co composite nano-hole array at an extraordinary optical transmission peak, which was induced by the surface plasmon polariton (SPP).[80] Another enhancement can be found at the Wood's anomalies due to the enhanced local E-fields. However, this E-field enhancement might not be as large as localized field enhancement. Yet, most multilayered MOP nanostructures are based on LSPR. Thus, it is also intriguing to investigate the LSPR properties of composite nanostructures and their role in MOP materials/structure designs. In this Chapter, we have investigated the MOP performance of Ag-Co composite nano-triangle array (CNTA) structures. The composition dependent optical transmission, FR, and magnetization hysteresis curves of CNTAs in the visible to near infrared wavelength region have been studied. Finite-difference time domain (FDTD) calculations have been performed to confirm the experimental results and to give an insight to the relationship between MO properties of CNTA structures and their compositions. Both plasmonic and magneto-optics properties have been characterized for different CNTA structures, and their relationships have been investigated.

4.2. Fabrications and Characterizations

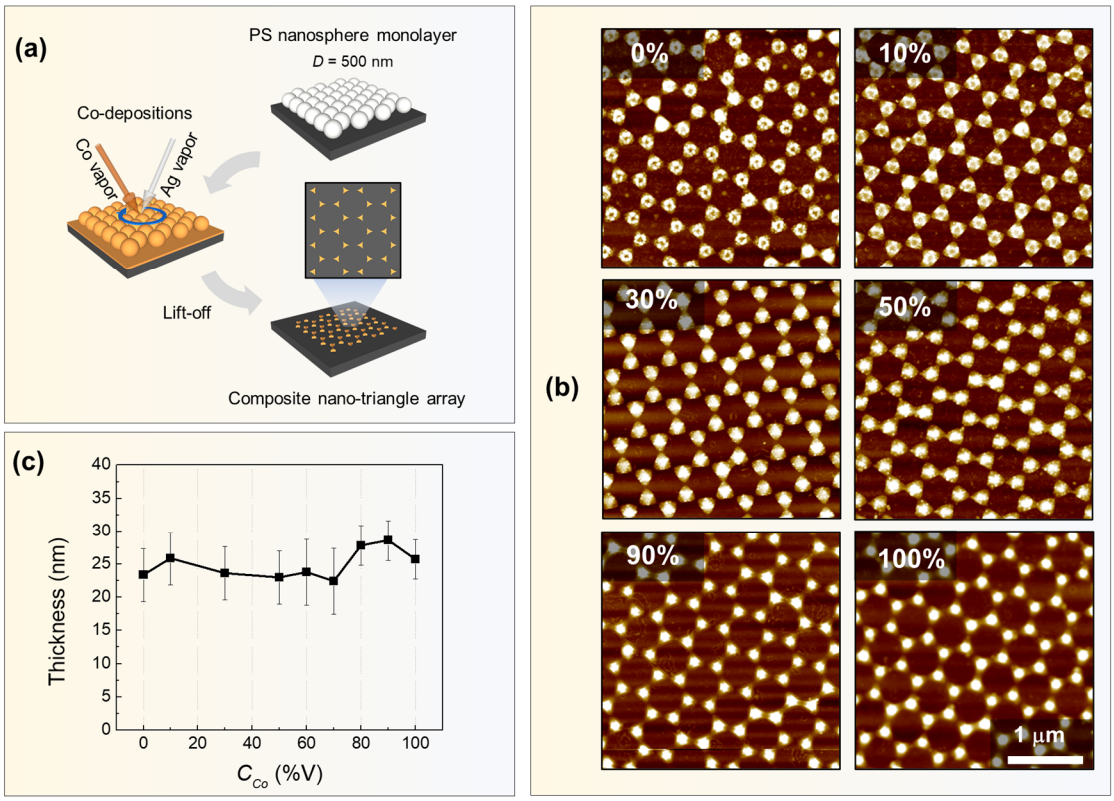

Figure 4.1. (a) The fabrication process of the CNTAs and (b) representative AFM images of the CNTAs with C_{Co} = 0, 10, 30, 50, 90, and 100 %V, respectively. The extracted thickness (t) of CNTAs with different C_{Co} (%V). The measured total thickness $t = 24 \pm 5$ nm.

CNTAs were fabricated based on shadowing nanosphere lithography (SNL) combined with electron beam co-deposition as illustrated in **Figure 4.1a**.[95-96] First, a hexagonally close-packed polystyrene (PS) nanosphere (diameter = 500 nm) monolayer was prepared on glass and Si substrates by an air-water interface method.[86, 96] The monolayer-coated

substrates were loaded into a custom-built dual-source electron deposition system (Pascal Technology) and mounted on a motor-controlled rotated holder. The metal depositions were performed when the base pressure of the chamber reached 10^{-6} Torr. A thin layer of Ti (t_{Ti} = 3 nm, deposition rate = 0.05 nm/s) was first coated in order to increase the adhesion between composite thin films and the substrates. A composite layer was then formed by depositing Ag and Co simultanously. The vapors of Ag and Co had incident angles of 10^{o} and -10°, respectively, which came from two separate crucibles placed in two sides of the chamber. The thicknesses and deposition rates of Ag and Co were measured independently by two separated quartz crystal microbalances (QCMs). The total QCM thickness (t_{QCM} = t_{Ag} + t_{Co}) was kept at 50 nm. The total deposition rate was set to be 0.6 nm/s, and the substrate holder was rotated azimulthally at a constant rate of 30 rpm to thoroughly mix Ag and Co. The volumic ratio of Co (C_{Co}) in the Ag-Co composite thin film was controlled by adjusting the deposition rate of Ag and Co, and a series of samples with different C_{Co} was fabricated (C_{Co} = 0, 10, 30, 50, 60, 70, 80, 90, and 100 (%V)). Afterward, the PS nanospheres were removed, and the substrates were subsequently washed with toluene, isopropyl alcohol, and deionized water to remove residual PS. The control samples, Ag-Co composite thin films, were also fabricated simultaneously under identical conditions. Before any characterizations, the CNTAs samples were stored inside a M. Braun glovebox system filled with N_2 (the concentrations of O_2 and H_2O are less than 0.1 ppm) to minimize potential oxidation effects.

Figure 4.1b presents some representative atomic force microscopic (AFM) images of the CNTA structures with diffrerent C_{Co} and an average measured height h = 24 ± 5 nm (see **Figure 4.1c**). The compositions of CNTAs were characterized by an energy-dispersive X-ray spectroscopy (EDS), which shows consistency between experimentally determined C_{Co} (C_{Co}^{EDS}) and the C_{Co} calculated based on the deposition rates of Ag and Co (C_{Co}^{cal}) (see **Figure 3.2**). Thus, from now all C_{Co}^{cal} will be referred as C_{Co} and CNTA samples with a specific Co composition will now be referred as $CNTA_x$, where x = 0, 10, …, 100, respectively, represents the percentage of Co.

4.3. Optical Properties of CNTAs

Due to the low reflectivity of the CNTA samples, the optical transmission spectra $T(\lambda)$ of the CNTA samples could be converted to extinction $e(\lambda)$ by the following equation: $e(\lambda) = -\ln T(\lambda)$. **Figure 4.2a** shows the extinction spectra of CNTAs with different C_{Co}. Overall, a strong LSPR extinction peak can be observed regardless of the film composition as indicated by dash curves in **Figure 4.2a**. For $CNTA_0$, the extinction at the LSPR peak is the strongest and has a narrow width. This peak is generally blue-shifted, broadened, and the extinction at the peak drops significantly when C_{Co} increases. This LSPR peak originally comes from the dipole resonance of free electrons, while the broad shoulder from 400 to 1000 nm can be explained by a weak in-plane and out-of-plane quadrupole resonances.[95-96, 122-123] No significant coupling effects can be observed from the extinction

spectra. These extinction features are typically seen for nano-triangle arrays fabricated via the SNL method.[64, 124-125]

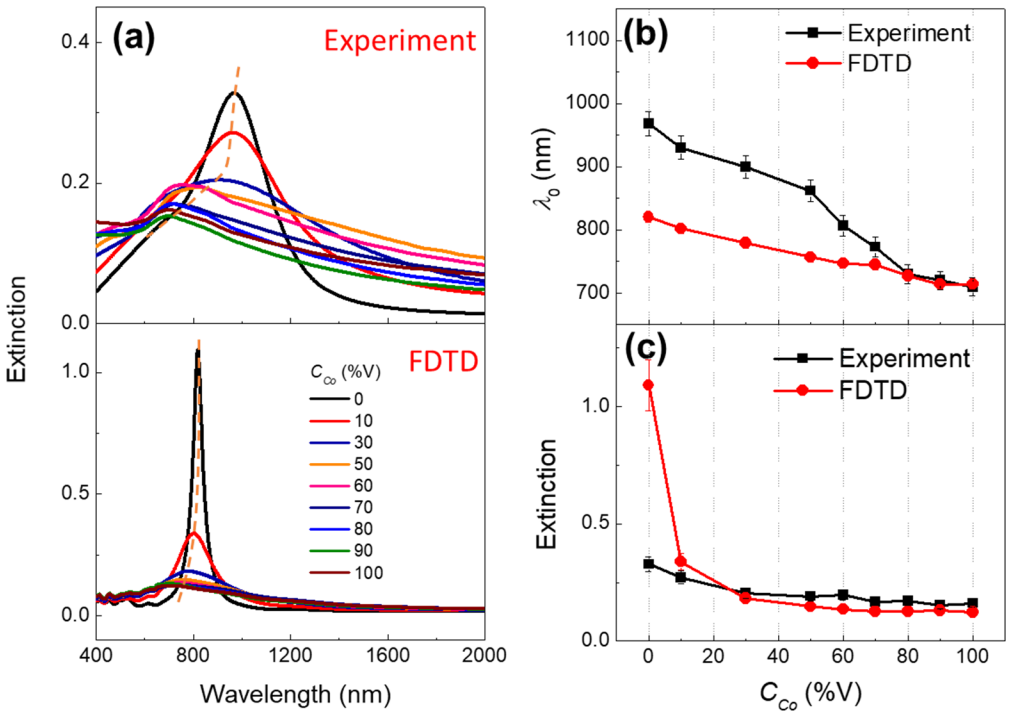

Figure 4.2. (a) Experimental and FDTD calculated extinction spectra of CNTAs. The prominent feature of extinction peak from LSPR were indicated. (b) The plots of experimental (black) and FDTD calculated (red) of LSPR extinction peak position λ_0 versus C_{Co}. (c) The plots of experimental (black) and FDTD calculated (red) extinction at LSPR peak versus C_{Co}.

FDTD calculations were performed to gain better understanding of optical properties of CNTAs (details see **Experimental Sections**). The calculated FDTD extinction spectra

of CNTAs are presented in **Figure 4.2a** (bottom), and they agree with the experimental results qualitatively (**Figure 4.2a,** top). Similar LSPR extinction peaks were also found. The extinction is also strongest in the $CNTA_0$ sample, and it decreases and blue-shifts as C_{Co} increases**.** For better comparison, the experimental and calculated positions of LSPR extinction peaks versus C_{Co} are summarized in **Figure 4.2b**. Significant red-shift of LSPR peak as more Ag was added into the composite film was observed in both experimental and calculated results with varying changing rates. Note that in the FDTD calculations, geometrical parameters of CNTAs (shape, size, and position, etc.) are fixed, and only the optical permittivities of composite materials were changed (see **Figure A1** in **Appendix A**). Thus, it is reasonable to state that the blue-shift in LSPR peaks as C_{Co} increases is mainly due to composition changes. In fact, when C_{Co} increases, the imaginary part ε_2 of the permittivity gradually increases, while the real part ε_1 becomes less negative and approaches to that of the pure Co. This change in optical permittivity of nanoparticle can damp the multipole absorption and blue-shift the resonance peaks.[126] The mismatches as seen between experimental and calculated FDTD results might come from imperfections in the experimental structures (such as thickness, sharpness of the edge and corner of nano-triangle, roughness of surface, *etc*.), which have not been considered in the FDTD calculations.[124]

Figure 4.2c shows similar trends of the LSPR extinction peak versus C_{Co} obtained in experiment and FDTD calculation. In particular, the extinction peak rises slowly when C_{Co} decreases from 100 %V to 30 %V and increases rapidly when C_{Co} varies from 30 %V to 0

%V. This observation implies that when Co is still a significant component in the composite nanostructure (C_{Co} > 30 %V), the plasmonic effects are weak. When $C_{Co} \leq 30$ %V (Ag is the dominant component), these effects become significant. This observation is consistent with our previous observation for composite nano-hole arrays.[80] The weak plasmonic effect of the composite film with C_{Co} > 30 %V is due to the strong absorption coefficient contributed by the Co component, which can be seen in the large imaginary part ε_2 of optical permittivity (see **Figure A1** in **Appendix A**).[80] Strong absorption damps the oscillation of electrons which eventually suppresses the LSPR effect and broadens the resonance peaks.[127-128] When more Ag is added and Ag becomes the dominant component (*i.e.* $C_{Co} \leq 30$ %V), the imaginary part ε_2 becomes smaller and closer to zero, while the real part ε_1 becomes more negative and approaches to that property of pure Ag. The changes in permittivity promote the interaction times between light and the materials, which results in stronger extinction and scattering at LSPR wavelengths.[129] Hence, the plasmonic properties of CNTAs are improved significantly at low C_{Co}. In addition, FDTD calculated time-averaged local E-field maps of $CNTA_0$, $CNTA_{10}$, $CNTA_{30}$, $CNTA_{50}$, and $CNTA_{100}$ samples at LSPR peak are extracted and exhibited in **Figure 4.3a**. At a glance, in all samples, strong local electric fields can be seen around the corners of the triangle nanostructures, and they are not coupled to each other as we mentioned previously. Magnitudes of enhanced local electric field also become stronger and cover larger areas when more Ag is added (*i.e.* when C_{Co} decreases). To be more quantitative, the ratios of

the local electric fields E to the incident field E_0 ($|E/E_0|$) of CNTAs at a selected point near the triangle corner (indicated in **Figure 4.3b**) versus C_{Co} are extracted and plotted in **Figure 4.3c.** As the C_{Co} decreases, the local field ratio at LSPR peak increases greatly, especially when C_{Co} is from 50 %V to 0 %V. These observations confirm our statement of improved plasmonic properties due to the presence of more Ag in CNTAs.

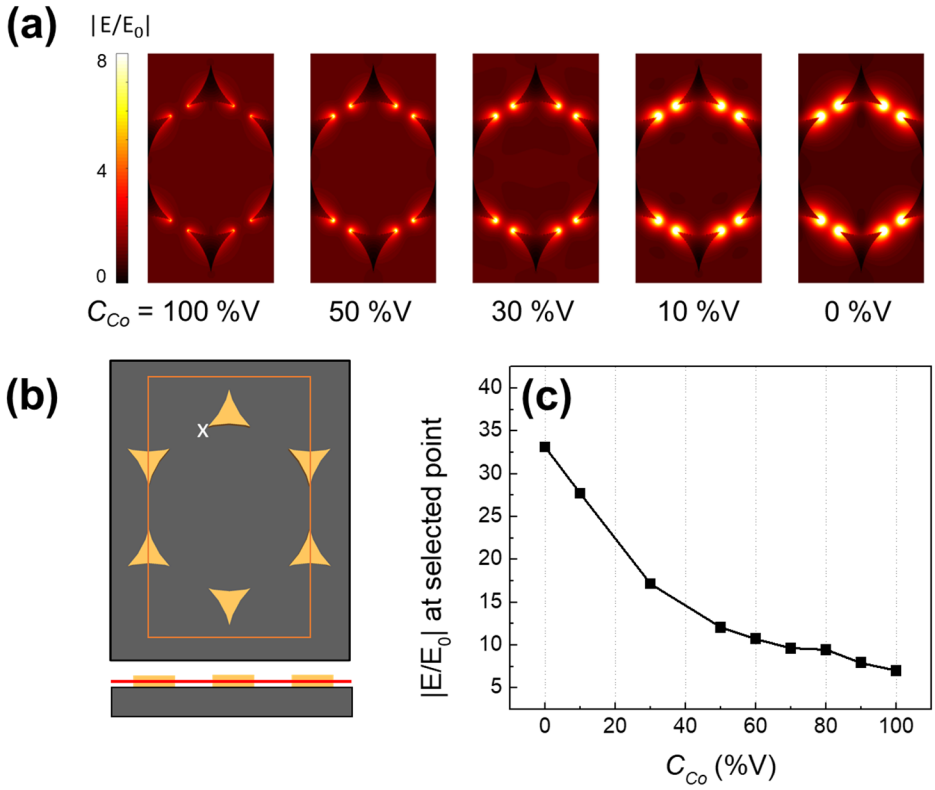

Figure 4.3. (a) Time-averaged local E-field maps calculated by FDTD at the cross-section plane (denoted by the red line in (b)) with different C_{Co} (%V). (b) Geometrical setup for FDTD calculation. The light incidents from top to bottom. The orange box in top plot denotes the rectangular unit cell for FDTD calculations. (c) Relative electric

field $|E/E_0|$ at a selected point of CNTAs with different C_{Co} (%V). The extracted positions are indicated by the white "x" mark in plot (b).

4.4. Magneto-optical Properties of CNTAs

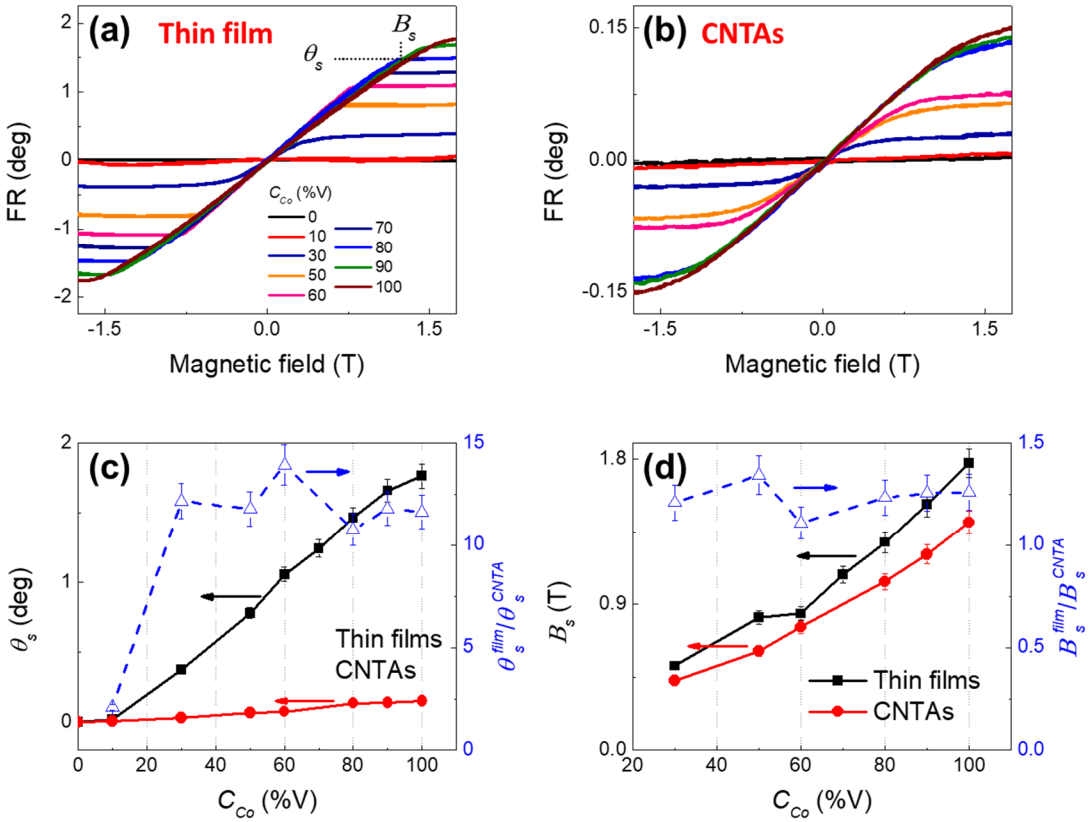

Figure 4.4. FR hysteresis curve of (a) composite thin films and (b) CNTAs with different C_{Co} (%V) (at $\lambda = 632$ nm). The plots of (c) saturated FR (θ_s) and (d) saturation field (B_s) of composite thin film (black) and CNTAs (red) for different C_{Co}.

The introduction of nano-structures on magnetic thin films have been demonstrated to significantly modify their magnetization dynamics.[59] Therefore, FR hysteresis curves

(measured at λ = 632 nm) of composite thin films and corresponding CNTAs were measured and are shown in **Figure 4.4a** and **b**. In general, typical hard-axis hysteresis curves with almost no remanence can be seen in all the samples, and the saturation field (B_s) appears at a very large value (for instance, at 1.7 T for the thin film with C_{Co} = 100 %V). This observation is the evidence of the out-of-plane hard axis of both CNTAs and composite thin films. However, the plots of the saturation field (B_s) and saturation FR (θ_s) versus C_{Co} are quite distinct between thin film and CNTA sample as shown in **Figure 4.4c**. Both CNTAs and thin film samples with C_{Co} = 100 %V produce the largest θ_s, and θ_s drops almost linearly with C_{Co} to approximately zero for samples with C_{Co} = 0 %V. However, θ_s in CNTAs is about one order of magnitude smaller than that of corresponding thin film samples. This is reasonable because of the removals of magnetic materials in CNTAs. In principle, θ_s should be proportional to Θ, the coverage of magnetic layer on surface, since both are proportional to the saturation magnetization M_s of the samples. If we assume that the surface density of magnetic moments is the same for both CNTAs and thin films, then $\theta_s^{film}/\theta_s^{CNTA} = 1/\Theta_{CNTA}$ is expected to be a constant. In fact, for CNTA sample, Θ_{CNTA} is about 9.4 % and $1/\Theta_{CTA}$ is about 10.6. This value agrees quite well with the experimental ratio, $\theta_s^{film}/\theta_s^{CNTA}$ = 12 ± 1 for samples with C_{Co} = 100 %V to 30 %V as plotted in blue in **Figure 4.4a**. However, for samples with C_{Co} = 10 %V, this ratio drops rapidly to about 2.5. This might come from the changes of the magnetic interaction at low C_{Co}, which can change the saturation magnetization of CNTAs non-linearly[107] and eventually change

θ_S^{CNTA}. Further theoretical efforts need to be carried out. On the other hand, the saturation field (B_s) of CNTAs is also influenced by the introduction of nano-triangles, as presented in **Figure 4.4b**. B_s of CNTAs (B_S^{CNTA}) is smaller than that of the thin film (B_S^{film}), and the ratio B_S^{film}/B_S^{CNTA} is almost a constant, about 1.25, for all C_{Co} samples. This observation implies that some out-of-plane components in competition with the intrinsic uniaxial anisotropy of the film were raised. These components were induced from local dipolar fields which were introduced by the nano-triangle edge.[59] Nevertheless, B_s also decreases when C_{Co} decreases for both thin film and CNTA samples, which means that the out-of-plane hard axis characteristic of Co thin films is weakened by adding more Ag. This is consistent with the observation of B_s in Ag-Co nano-hole arrays as well.[80]

The composition dependence FR of CNTAs has been further examined. **Figure 4.5a** plots the experimental (top) and FDTD calculated (bottom) FR spectra of CNTAs. In both spectra, a broad FR peak can be observed at the wavelength range of λ = 700 to 900 nm as indicated by the long dash curve in **Figure 4.5a**, which shows a strong composition dependence. Generally, all the FR spectral shapes are similar regardless of C_{Co}. However, the peak positions and magnitudes change. To better understand the C_{Co} dependent FR behavior, experimental and FDTD calculated positions and magnitudes of the FR peaks are summarized in **Figure 4.5b** and **Figure 4.5c**. In terms of peak position, the FR peak positions are plotted along with the LSPR peak position (as a reference) as shown in **Figure 4.5b**. In both results, the FR peak blue-shifts almost linearly with C_{Co}. In fact, a close

relationship between the plasmonic and MO behaviors of CNTAs can be observed. The positions of FR peaks occur at the same locations of the LSPR peaks, in both experimental and FDTD calculated results as shown in **Figure 4.3b**. Therefore, it is expected that the origin of this enhancement peak on the FR spectra comes from the enhanced electric field induced by LSPR, which has been presented in the spatial distribution of the local E field mapping in **Figure 4.4a**. Another way to explain the enhancement is that it comes from the long interaction time between light and magnetic layer at LSPR wavelengths, which has been demonstrated in multilayer Au/Co/Au–SiO_2 nano-disks and Ag/Co dimer nanodot.[112, 114] On the other hand, in our previous work of composite nano-hole arrays,[80] we have demonstrated that even though the electric field has been enhanced at both Wood's anomalies and the extraordinary optical transmission peak (which corresponds to the surface plasmon polariton), the enhancement of FR and Faraday ellipticity (FE) were only found at the Wood's anomalies, where the local electric field are strongly enhanced.[80] Current observation is a further confirmation that the enhancement of MO activity is mainly due to the local field enhancement associate with LSPR in composite nanostructures.[112] In terms of FR magnitude, it also increases at almost a linear rate with C_{Co}, as seen in **Figure 4.5c**. The positions and magnitudes of FR peaks obtained experimentally or though FDTD calculations are in general consistent with each other. However, there still exists some mismatches, for example, the positions of the peaks. These discrepancies might come from the imperfections of experimental structures (such as

variations in thickness, sharpness of the edge and corner of nano-triangles, roughness of surface, *etc*.) have not been considered in the FDTD calculations.

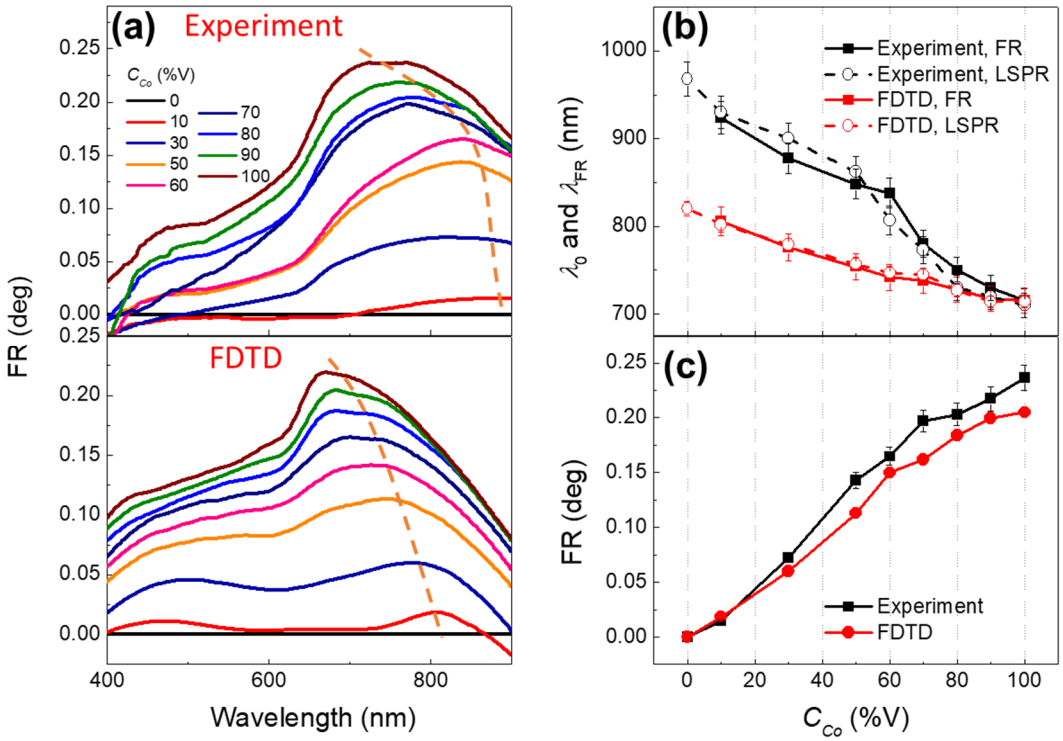

Figure 4.5. Experimental and FDTD calculated FR spectra of CNTAs. The prominent features of FR at LSPR extinction peak position were indicated. (b) The plots of experimental and FDTD calculated FR peak position λ_{FR} versus C_{Co}. (c) The plots of experimental and FDTD calculated FR at the LSPR peak λ_{FR}.

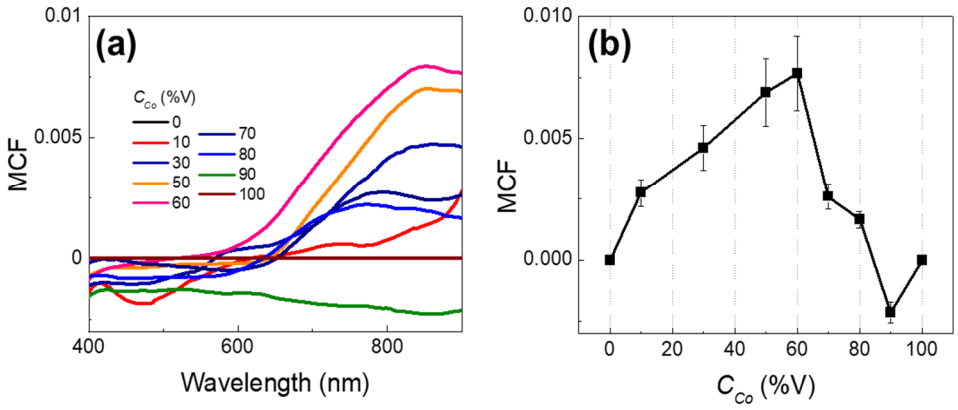

Figure 4.6. (a) The experimental MCF spectra (MCF= $\theta_F \times \Delta e(\lambda)$) of CNTAs, and (b) the MCFs at LSPR peak *versus* C_{Co}.

To illustrate the MOP response of the entire spectrum, a different characterization parameter is needed. In the research field of MO and MOP, figure of merit (FOM) is widely used to characterize the MO response of magnetic samples.[7] In particular, for structure/device that employs Faraday effect, where high transmission/low absorption are highly desired, FOM is normally defined as FOM = $\theta_F \times \sqrt{T}$, where θ_F and T are the modulus of Faraday angle and optical transmission of the sample, respectively.[74] While this definition reflect well the MO responses of magneto-plasmonic structures/devices, the plasmonic effect is not included in the equation. The main focus here is to investigate how the MOP property would be influenced by the composition of the Ag-Co composites, i.e., both the pure Ag and pure Co nanostructures were used as a reference sample, so should be their corresponding optical or MO properties. Therefore, we would like to have a different parameter to characterize the magneto-optics – plasmonic responses. Clearly,

when C_{Co} increases, the plasmonic effects of Ag-Co CNTAs become less significant while the MO performance becomes stronger. The higher the FR is, the larger the MO effect. The $CNTA_0$ (pure Ag) does not have any FR response. Therefore FR(λ) is a good parameter to characterize the MO effect. Similarly, the higher the extinction spectrum (peak) $e(\lambda)$ is, the larger the plasmonic effect. However, the $e(\lambda)$ for $CNTA_{100}$ (pure Co) is not null, which means $e(\lambda)$ does not directly reflect the plasmonic effect. Assuming that for the $CNTA_{100}$ (pure Co) sample, there is no plasmonic enhancement effect, hence, $\Delta e(\lambda) = e(\lambda) - e_{CNTA_{100}}$ (where $e_{CNTA_{100}}$ is $e(\lambda)$ of $CNTA_{100}$ sample), is a better function to characterize the plasmonic enhancement. A good MOP CNTAs should have both good plasmonic properties and reasonable MO properties for a certain C_{Co}. Therefore, to compare the MOP performance of CNTAs with the different C_{Co}, a MO-plasmonic correlation factor (MCF) spectrum of the nanostructures can be defined as MCF = $\theta_F \times \Delta e(\lambda)$, where $\theta_F = \sqrt{FR^2 + FE^2}$ is the modulus of the Faraday angle. Experimental MCF spectra for different C_{Co} are shown in **Figure 4.6a**. As expected, the MCFs for both $CNTA_0$ and $CNTA_{100}$ are zero. The overall shape of MCF spectra also strongly depends on $\theta_F(\lambda)$ and $\Delta e(\lambda)$ spectra. **Figure 4.6b** summarizes the value of MCF at LSPR peak versus C_{Co}. When C_{Co} increases (from 0 %V), MCF also increases and reaches a maximum value at C_{Co} = 60 %V. Then the MCF value deceases quickly to a negative value as C_{Co} approaches 90 %V and returns to null when C_{Co} = 100 %V. Based on the discussion for **Figure 4.6**, the $CNTA_{60}$ has a very

good MCF performance. Therefore, for future MOP-based device design with CNTAs or nanoparticles in general, C_{Co} = 60 %V should be considered.

4.5. Conclusions

CNTAs with different compositions of Ag and Co are fabricated by SNL and electron beam co-deposition. The samples exhibit strong plasmonic properties with high composition of Ag, and the samples with high composition of Co show larger MO effect. In particular, the enhanced MO effect is coincident with the LSPR properties, *i.e.*, for each sample, the maximum MO effect occurs at LSPR wavelength, which is due to high local E-field. Hence, the MO and optical properties of samples can be adjusted simultaneously by modifying the relative ratio of Ag and Co, which can be used to compromise the MO performances of CNTAs. In addition, the $CNTA_{60}$ sample has been demonstrated to yield better MCF than that of pure Co and Ag CNTAs samples. Moreover, thanks to the flexibility of SNL, several geometrical parameters (sizes, thicknesses, shapes, *etc.*) of CNTAs can also be tuned in order to optimize MO performances. This tunability shows promising designs and applications for future magneto-plasmonic materials and structures. This proposed MOP composite materials and nanostructures can be used in many current MO devices, such as chiroptical devices, *etc*., to achieve a better device performance.

4.6. Experimental Sections

Materials: Deionized water (18 MΩ.cm) was used for all experiments. PS nanospheres (Polysciences Inc., D = 500 nm) and ethanol (Sigma-Aldrich, 98%) were used to create the

nanosphere monolayers. Silver (99.999%), cobalt (99.95%), and titanium (99.995%) from Kurt. J Lesker Company were utilized for e-beam codeposition.

Morphology and composition characterization: The morphologies of CNTAs were characterized by an atomic force microscope (AFM, Park NX10), and all the AFM images were analyzed by XEI - Image Processing and Analysis Software. The compositions of thin film samples were characterized by an Energy-dispersive X-ray spectroscopy (EDS) of a field emission scanning electron microscopy (SEM, FEI Inspect F). Here we assume that the corresponding CNTA samples and thin film samples have the same composition since they were prepared simultaneously. The crystallinities of the composite materials were investigated by an X-ray diffractometry (XRD) with a PANalytical X'Pert PRO MRD X-ray diffractometer at a fixed incident angle of 0.5°.

FDTD calculations: To better understand the optical and MO properties of the samples, FDTD calculations were carried out using a commercial software (Lumerical FDTD Solutions).[109] The extracted film thickness (t_C) and period from AFM images were used to build the FDTD model. The FDTD simulation domain was set to cover a rectangular unit cell (orange box, **Figure 4.3b**). Periodic boundary conditions were used to present the two-dimensional periodicity of CNTAs, and perfect matched layer (PML) boundary conditions were applied on the top and bottom sides of the rectangular cuboid simulation region. The FDTD mesh size was set as 2 nm × 2 nm × 2 nm to compromise between the calculation time and the convergence of the calculations. A frequency-domain field and power monitor

was placed to collect the transmitted light, the **E** and **H** components of the electromagnetic field. The FR was calculated according to Ref. [109-110]. The refractive index of air was fixed to be 1, and the dispersive refractive index of glass was taken from Ref. [111]. The complex optical permittivities $\varepsilon = \varepsilon_1 + i\varepsilon_2$ of Ag, Co, and composite material were experimentally determined from the spectral ellipsometry data of corresponding thin films (Supplementary Information (SI) of Ref. [80]). The MO constants used for FDTD calculations[4] were extracted from the experimental Co thin films and composite thin films data, measured by the FR spectroscopy (see SI of Ref. [80]).

CHAPTER 5

ACTIVE COMPOSITE CHIRAL NANOHOLE ARRAYS

In Chapter 3 and 4, we study the nanostructures with in-plane mirror symmetry, and they therefore exhibit no intrinsic chirality. In this Chapter, we investigate the magneto-chiroptical properties in a novel chiral nanohole array structure, which possesses intrinsic circular dichroism induced by in-plane symmetry breaking. The chiral magneto-plasmonic properties of this composite metasurface will be discussed throughout.

5.1. Introduction

Recently, active chiral plasmonic metamaterials (CPMs) have attracted considerable attention.[130] In general, the optical response of the active CPMs has been tuned by an external stimulus such as light,[131-135] mechanical stretch,[136] temperature, electric field,[137-140] magnetic field,[141-144] etc. Among all tuning mechanisms, magnetically switching optical chirality has been widely considered due to numerous advantages, such as ultrafast switching speed, continuous tunability, and easy to integrate and operate.[37, 130] By incorporating a magnetic material into a CPM structure to form the so-called chiral magneto-plasmonic (CMP) metamaterial, one is able to tune the corresponding chiroptical properties by an external magnetic field due to the magneto-optical (MO) effect. Such an

effect has been realized by a few structures, such in multilayer Au/Co gammadion,[141] plasmonic chiral oligomers with Au/Co multilayer,[143] Au/Co split-ring,[144] Au/Ni trimer nanoantennas,[37] etc. In these structures, when the MO active material (Co, Ni, Fe) is coupled with chiral plasmonic nanostructures, the strong local electromagnetic fields produced by the plasmonic material (Ag, Au) through the localized surface plasmon resonance interact strongly with the magnetic material.[7] Consequently, the MO and circular dichroism properties of the magnetic material could be significantly altered by the externally applied magnetic field.[7] So far, all the reported magnetically tuned CPMs are composed of ferromagnetic and noble metals in two- or three-dimensional (2D and 3D) fashion, such as multilayer structures or separated antennas of single component ferromagnetic/noble metals.[37, 141, 143-144] However, it is expected that if an alternative material system that possesses both magnetic and plasmonic responses, such as a composite of noble metals and magnetic materials, i.e., Au, Ag composites with Co, Fe or Ni, should also be able to construct a good CMP structure. In fact, the use of composite materials in MO nanostructure has recently been demonstrated by our group to enhanced magneto-plasmonic performances of achiral nanostructure (such as nanohole arrays[80] or nanotriangle arrays[81]) in comparison to these made of pure ferromagnetic.

In this work, we propose to design, fabricate, and characterize a composite chiral nanohole array (CCNAs) by shadow nanosphere lithography technique (SNL) made from Ag and Co with different composition.[145] Ag-Co vapors are co-evaporated with different polar/azimuthal angles, and the resulting CCNAs break the mirror symmetry in both in-

plane and light-propagation directions and induce strong intrinsic optical chirality. The Co content in CCNAs allows the magnetically tunable optical chirality, while Ag component induces strong surface plasmon polariton (SPP) and localized surface plasmon resonance (LSPR) and further enhance the tunability of the chiral response. Finite-difference time domain (FDTD) calculations are performed to confirm the experimental results and to give an insight to optical chirality of CCNA structures and their compositions.

5.2. Results and Discussions

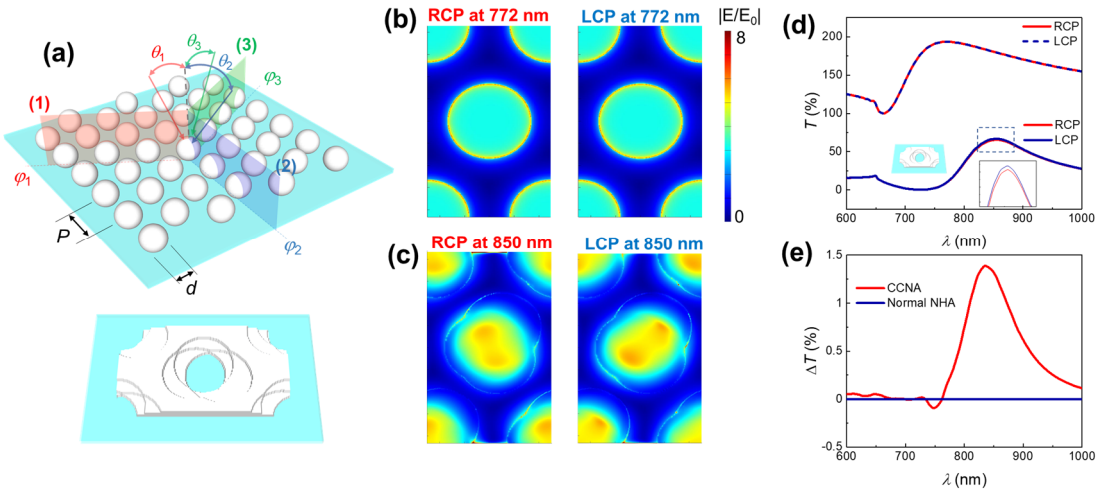

Figure 5.1. (a) Top panel: schematics of the fabrication process and the main parameters of polar angle θ, azimuthal angle φ, period P, and diameter of the etched sphere d. Bottom panel: Calculated structures of the LH-CCNAs based on an in-house MATLAB program. (b) FDTD-calculated electric near-field of a symmetric Ag nano-hole array (NHA) illuminated with the RCP and LCP light at $\lambda = 772$ nm. (c) Calculated field distributions of Ag CCNA under illumination of RCP and LCP light at $\lambda = 850$

nm. (d) The calculated $T_R(\lambda)$ and $T_L(\lambda)$ of symmetry NHA and CCNA samples and (e) corresponding CDT spectra.

The CCNAs are designed based on thin film perforated nanohole arrays (NHAs), which have the following exclusive properties: (i) the extraordinary optical transmission (EOT) effect: the optical transmission in the plasmon-grating coupling wavelength region can be much greater than that predicted by Bethe's theory simply for light going through corresponding holes;[98] (ii) coexistence of SPP and LSPR which both could be used to enhance giant chiro-optical and magneto-optical responses;[7] (iii) multifunctional properties (plasmonic and magneto-optical properties coexist in the system), which come from Ag-Co composite material used;[80] and (iv) ultra-thin thickness. The light-material interaction in this system can be optimized by many factors, such as the shape and dimension of hole aperture, deposition symmetry, film thickness, periodicity, lattice symmetry, filling factor of the NHA, composition of the materials, etc. in order to achieve a maximum chiro-optical properties.[98] Nevertheless, the chiral responses can be magnetically-tunable over a broad spectral range, which can be potentially used for ultrafast optical switch.[37] This large tunable parameter space makes the design of NHA-based CMPs more flexible. The proposed CCNAs fabrication strategy by SNL is depicted in **Figure 5.1a**.[145] Hexagonal non-close-packed nanosphere (period P = 500 nm, diameter d = 350 nm) monolayers are used as a template. Ag and Co vapors are then simultaneously deposited at different incident and azimuthal angles for three consecutive depositions, $\theta_1 = 10°$ and $\varphi_1 = 0°$, θ_2 =

20° and φ_2 = 120°, and θ_3 = 30° and φ_3 = 240°, respectively, where θ_1, θ_2, and θ_3 are the vapor incident angles with respect to substrate normal, φ_1, φ_2, and φ_3 are the relative projected azimuthal angles of incident vapor on the substrate plane. Note that these angles of θ and φ are chosen to minimize the domain effects to circular differential transmission (CDT) spectra.[145] During the three consecutive depositions, the ratio of the Ag and Co deposition rates, the deposited time and thickness for each deposition are fixed as a constant, respectively. Note that the azimuthal rotation direction of the substrate for the three consecutive depositions is counter-clockwise, this results in a left-handed- (LH-) CCNAs, which yield a favorable optical transmission with left-circularly polarized light (which will be discussed below).[145]

We first evaluate the chiroptical response of the Ag CCNA structure as well as achiral NHA by FDTD calculations, which were carried out using a commercial software (Lumerical FDTD Solutions).[109] The geometry parameter of achiral and chiral NHA structures are based on the surface morphology generated from a home-built MATLAB program (with period P = 500 nm, diameter d = 350 nm),[124, 146] and the complex optical permittivity $\varepsilon = \varepsilon_1 + i\varepsilon_2$ of Ag used for calculation were extracted experimentally from the ellipsometry data of corresponding thin films.[80] Two separated calculations with left-circularly polarized light (LCP) and right-circularly polarized light (RCP) were performed and the difference between the optical transmission in two cases was obtained. In addition, the electric field distributions at certain cross-section were taken by a frequency-domain

field and power monitor. The near-field electric field distribution at EOT wavelength position of achiral NHA and CCNA samples (extracted at the Ag-air interface), are summarized in **Figure 5.1b** and **c**, respectively. While the achiral NHA showed no difference in near-field electric field distribution when it is excited with LCP and RCP (**Figure 5.1b**), CCNA exhibits noticeable differences in electric field distribution when it is illuminated with LCP and RCP (**Figure 5.1c**). As a result, the optical transmission at the far-field also exhibits different optical responses: while the LCP- and RCP-optical transmission of achiral NHA are identical, these of CCNA show discrepancies at the transmission dip ($\lambda \approx 750$ nm) and EOT peak ($\lambda_{EOT} \approx 850$ nm) (**Figure 5.1d** and **e**). We highlight that the large chiral optical transmission response is frequently desired to be assosiated with large optical transmission, which is the case at the EOT peak. In addition, the differences between the peak and dip positions of optical transmission spectra (**Figure 5.1d**) comes from a larger effective hole volume of CCNA in comparison to that of achiral NHA. The red-shifts of these dip/peak are consistent with previous works.[147-148]

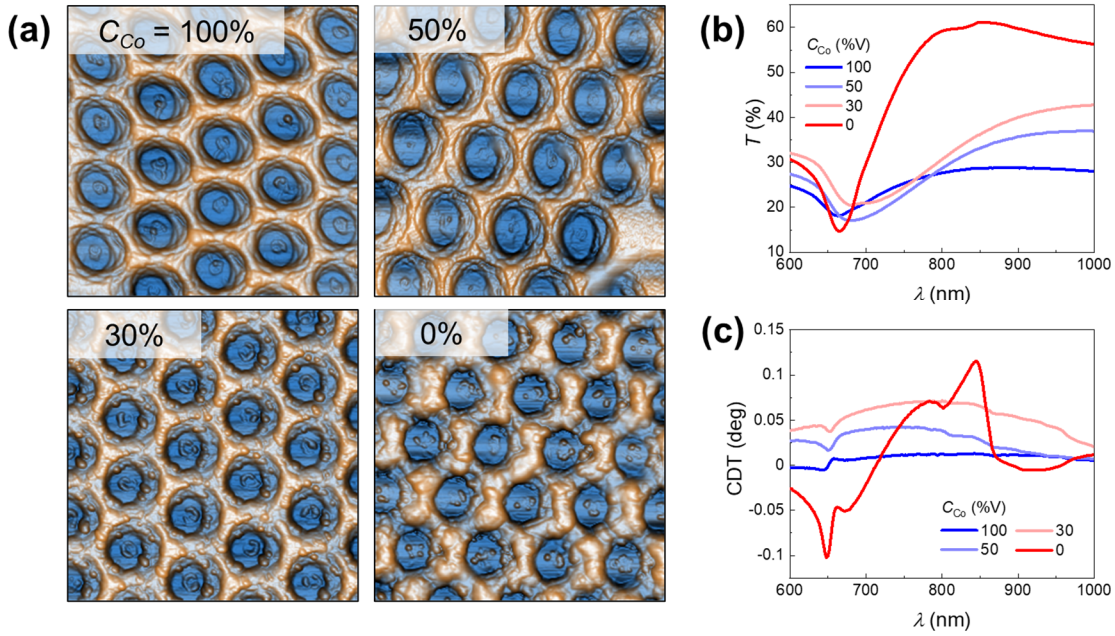

Figure 5.2. (a) Representative AFM images of CCNAs with different C_{Co} (%V). (b) Optical transmission spectra of CCNA samples, illuminated by unpolarized light. (c) CDT spectra of CCNA samples.

Figure 5.2a shows the representative atomic force microscope (AFM) images of LH-CCNAs with different Co concentration C_{Co} = 100, 50, 30, and 0 of volume percentage (%V), respectively (will now be referred as CCNA$_x$, where x = 100, 50, 30, 0, respectively, represents the volume percentage of Co). The thicknesses of the films are consistantly at about 55 ± 7 nm, which matches with the morphology simulated from an in-home MATLAB program.[124, 146] The non-polarized optical transmission spectra of the CCNAs are shown in **Figure 5.2b**. In general, the shape of spectra is similar regardless of C_{Co}, with a transmission maximum peak at $\lambda_{peak} \approx$ 850 nm and a local minimum at $\lambda_{dip} \approx$ 660 nm.

Based on the Bloch wave condition and Wood – Rayleigh anomaly condition, we assinged the transmission maximum $\lambda_{peak} \approx 850$ nm and a local minimum at $\lambda_{dip} \approx 660$ nm as the (1,0) resonance mode and (1,0) Wood's anomaly at the film-glass interface, respectively. λ_{dip} shows an insignificant change when C_{Co} increases, which follows well with the Wood – Rayleigh anomaly theory since the Wood's anomalies are purely geometric and the corresponding wavelength position does not depend on the optical permittivity and plasmonic properties of metal film.[102] On the other hand, λ_{peak} shows a larger change on C_{Co}, as this peak is sensitive to the film permittivity and other geometrical parameters (such as film thickness,[103-104] hole diameter,[104] hole shape[105]).

Figure 5.2c shows the circular differential transmission spectra (CDT) (CDT (deg) = $32.98° \times (T_{LCP} - T_{RCP})$)[149-151] of CCNA sample with different C_{Co}. As expected, $CCNA_0$ gives the strongest CDT signal, with a peak at $\lambda \approx 850$ nm and a dip at $\lambda \approx 650$ nm. We note that the CDT spectra for different azimuthal angles and illumination directions show good resemblances, which implies that the majority of the signal originates from the chirality instead of linear anisotropy. As C_{Co} increases, the magnitude of CDT at these extrema wavelengths decreases and is about a magnitude of order smaller when $C_{Co} = 100$ %V, and the spectral feature becomes very broad. This observation can be explained by the strong local electric fields induced by plasmon resonance in the $CCNA_0$ sample (**Figure 5.3**) [80]. When C_{Co} increases from 0 to 50%V, the imaginary part ε_2 of optical permittivity of composite film increases, while the real part ε_1 of optical permittivity becomes less

negative and approaches to that of the pure Co,[80] which damps the SPR and reduces the CDT at the resonance wavelengths. In addition, the majority of CDT signal of $CCNA_{100}$ sample originates from the CCNA structure, *i.e.* the symmetry breaking of the structure.

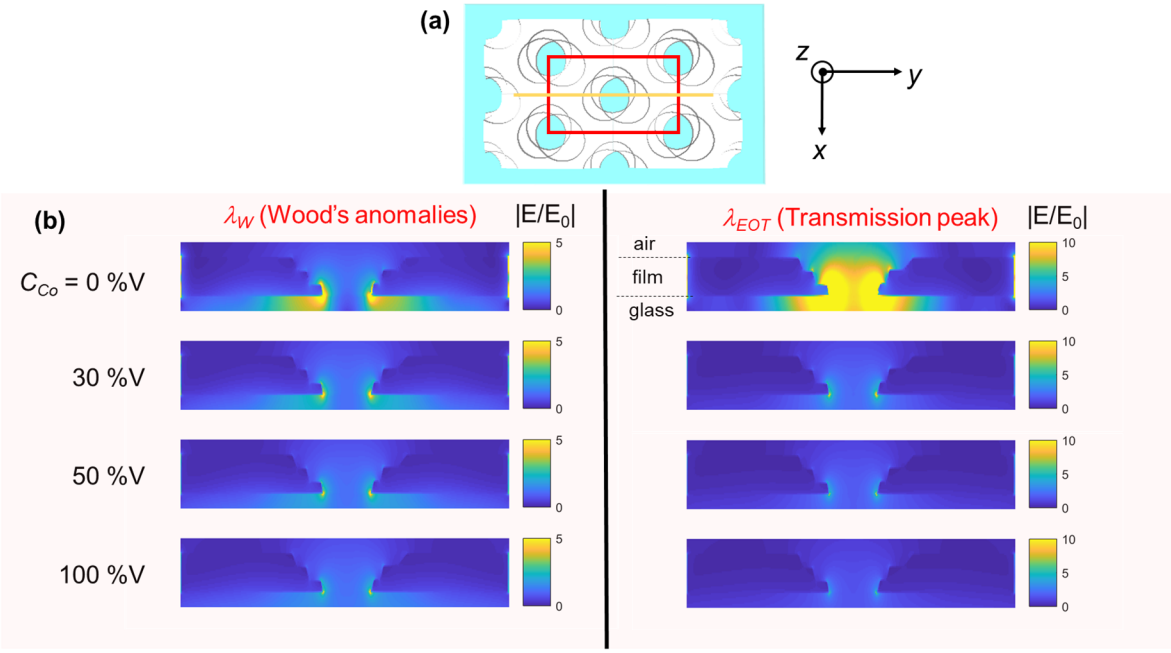

Figure 5.3. (a) A top-view of the hexagonal lattice of CCNA, the red box denotes the rectangular unit cell for FDTD calculations. (b) Time-averaged intensity maps of the FDTD calculated local electric field at the cross-section plane denoted by the yellow line (in (a)), with different C_{Co} (%V).

In order to understand the chiro-optical response of the CCNA at the EOT, we underline the transmitting mechanism of optical field through the NHA structure. Unlike in the metal thin film where the electromagnetic waves must penetrate directly through the film and the evanescent field falls off exponentially from the surface; the introduction of NHA structure

compensates the momentum mismatch between a free-space photon and an surface plasmon (SP) wave.[98] This additional quasi-momentum provided by NHA allows the SP (i) being excited at the light incident film-dielectric interface, (ii) propagating on this interface (so called SPP), (iii) passing through the hole, and (iv) emitting at the another film-dielectric interface and can be probed at the far-field.[152-153] Thus, any disparities of handedness structure that involve in processes (i)-(iv) can create a change in optical transmission of circularly polarized light.

Similarly, in our CCNA structure, SPPs on the light incident interface couple evanescently to the light transmitted interface before being re-emitted into far-field. The role of SPPs is to enhance the electric field magnitude around the apertures and compensates for the exponential attenuation of the evanescent field in the depth of the non-propagating aperture. Based on this knowledge, we hypothesize that the symmetric/dissymmetric coupling between the handedness of the chiral aperature and polarization of the electromagnetic wave in process (iii) originates the chiro-optical responses of the CCNA structure. In order to illustrate this point, the current density of LH-$CCNA_0$ at different cross-section planes (excited from glass-side interface by LCP and RCP at $\lambda \approx 850$ nm) are calculated by FDTD based on the structure exported from the AFM image, at thickness t = 0 (glass-film interface), 20, 40, and 57 nm (air-film interface), respectively (**Figure 5.4a**). In each cross-section plane, the current sources (*i.e.* negative and positive poles) are observable, and the corresponding direction of the dipole changes

with the propagation of the light. The orientations of these dipoles are summarized in **Figure 5.4b**. Under an RCP illumination, the dipole direction rotates about 5° clockwise along the light propagation direction. As the current dipole rotation is against the polarization rotation of the excited light, the dissymmetric coupling between the handedness of the aperture and polarization, *i.e.*, with the opposite rotation, would weaken the evanescent field and in turn reduce the transmission.[145, 150] On the other hand, under an LCP illumination, the dipole orientation rotates 32° clockwise. In this case, the handedness of the structure is the same as the direction of the polarization. Thus, the evanescent field is supported and leads to slightly higher transmission.[145] Another CDT extremum emerges at $\lambda \approx 650$ nm, which is induced by the (1,1) resonance mode at film-glass interface in $CCNA_0$ sample, can be explained in a similar manner.

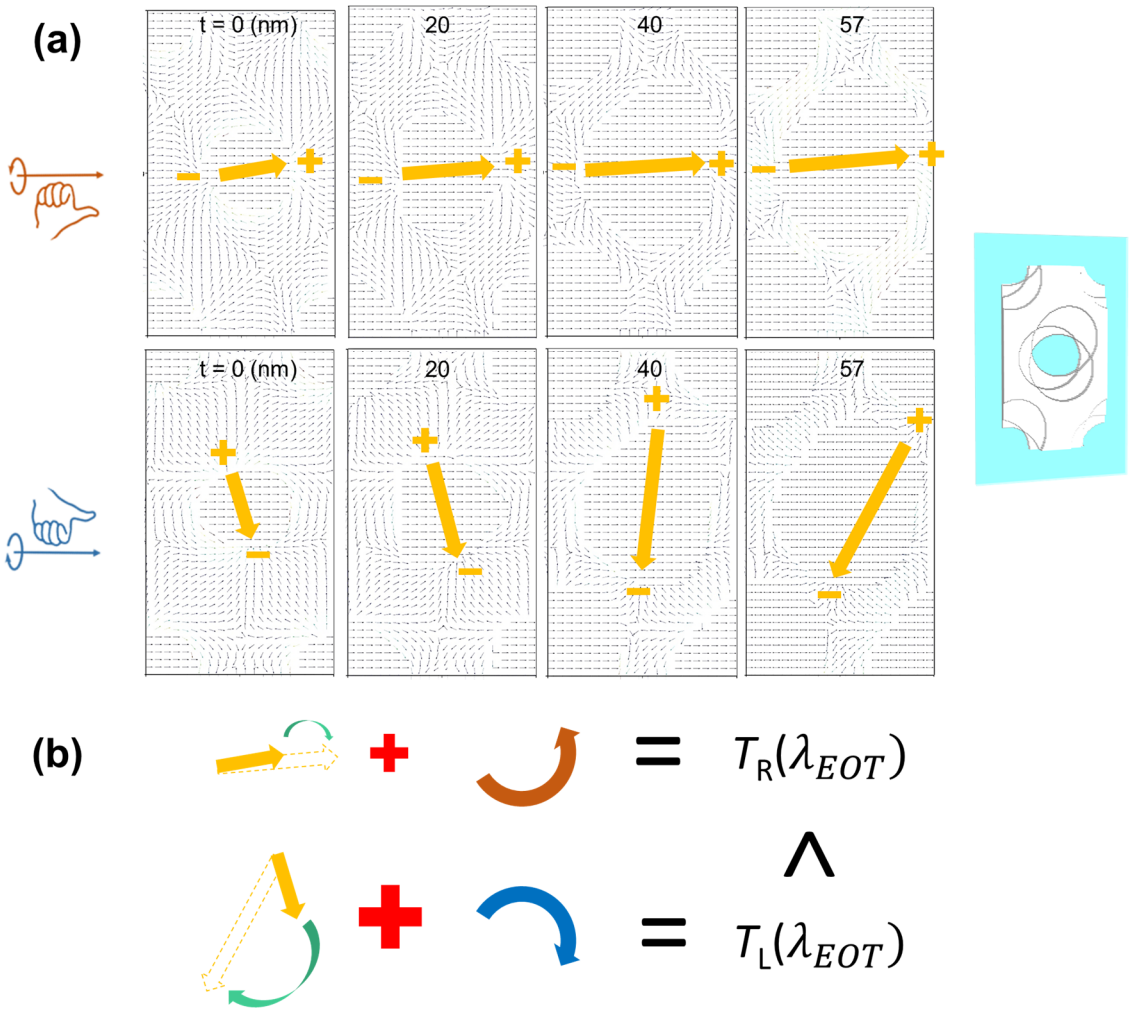

Figure 5.4. (a) The local current density distributions of the $CCNA_0$ sample excited by a RCP (top panel) and a LCP (bottom panel) incident light at λ_1 = 850 nm for the plane t = 0, 20, 40, and 57 nm respectively. The arrows indicate the current density direction. (b) Top-view illustration of rotations of effective current pole directions from the top layer to the bottom layer under RCP and LCP illuminations, respectively. The straight dashed arrows represent the

pole direction at the $t = 0$ nm plane, while the solid arrows show the pole direction at the $t = 57$ nm plane.

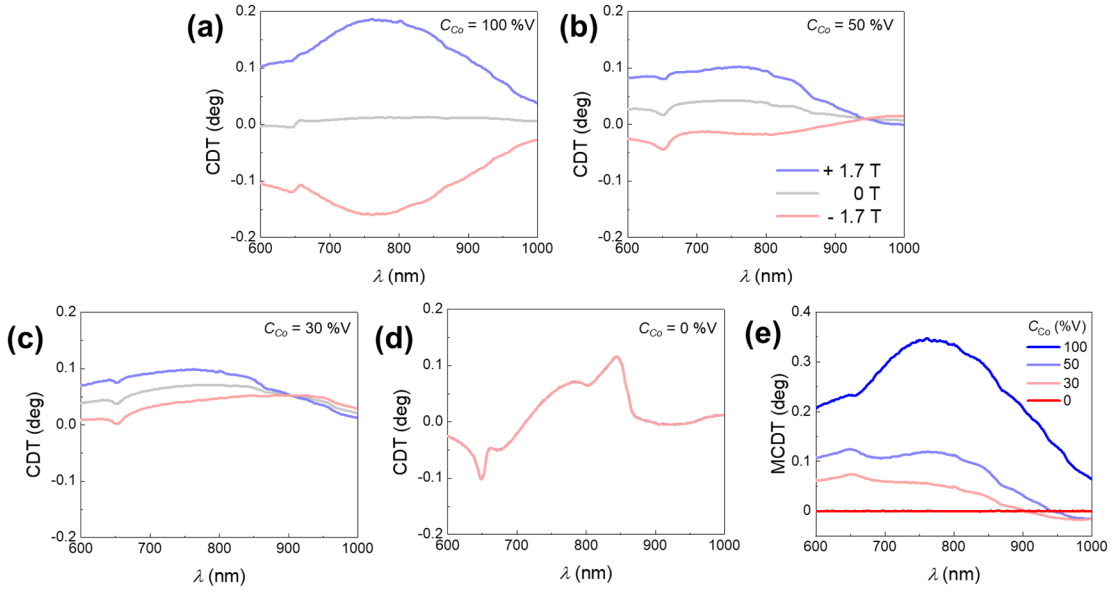

Figure 5.5. The CDT spectra of CCNA samples under external magnetic field of $B = \pm 1.7$ Tesla, with C_{Co} = (a) 100, (b) 50, (c) 30, and (d) 0 (%V). (e) The MCD spectra of CCNA samples with different C_{Co}.

The effect of external magnetic field to switch the optical chirality of the CCNA samples are shown in **Figure 5.5** by applying a constant manetic field, $B = + 1.7$ T, 0 T, and -1.7 T for CCNAs with different C_{Co}. Note that normal angle of incidence of light was used and polar magnetic field was applied. Generally, CDT changes with the external magnetic field is the largest in pure Co sample, and magnitude of change reduces gradually when C_{Co} decreases and reaches zero in pure Ag CCNA sample. In addition, over the

wavelength range of 600 – 900 nm, CDT increases when the direction of magnetic field lines is parallel with the wave vector of incident beam, and vice versa, CDT decreases when the direction of magnetic field lines is anti-parallel with the wave vector of incident beam. In order to quantitatively measure the change of CDT under magnetic field, we utilize the magnetic CDT (MCDT), which is determined by the following equation:[154]

$$MCDT = CDT(+B) - CDT(-B), \tag{5.1}$$

where the $CDT(\pm B)$ is the CDT signal measured at external magnetic field of $B = \pm 1.7$ Tesla, respectively. **Figure 5.5e** shows the MCDT spectra extracted from **Figure 5.5a-d**, which reveals the largest MCDT magnitude for the pure Co CCNA sample, and decreases to null when C_{Co} decreases to 0 %V.

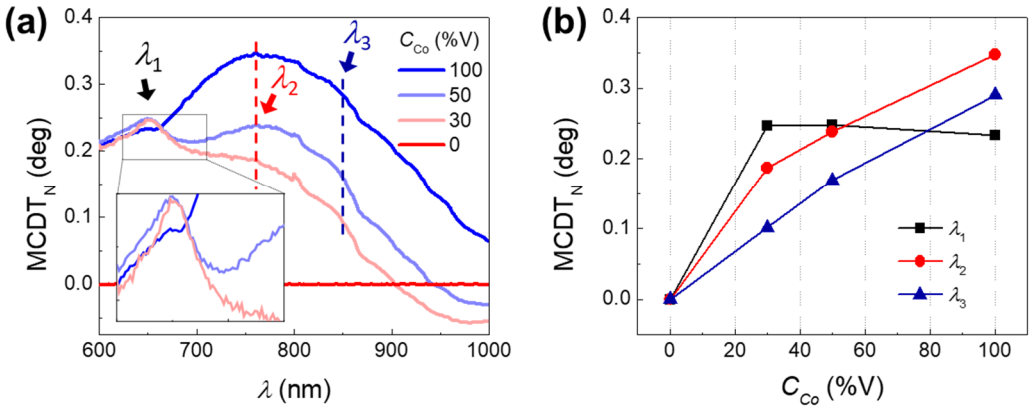

Figure 5.6. (a) The normalized $MCDT_N$ spectra of CCNA samples under external magnetic field of $B = \pm 1.7$ T, with different C_{Co}. (b) The plots of the $MCDT_N$ magnitudes of different CCNA samples extracted at λ_1, λ_2, and λ_3 versus C_{Co}.

In order to compare the MCDT magnitude with different C_{Co}, we normalize MCDT for amount of magnetic material, $MCDT_N = (MCDT \times 100)/C_{Co}$. The normalized $MCDT_N$ spectra of CCNAs to the same Co content with different C_{Co} are summarized in **Figure 5.6a**. At C_{Co} = 100 %V (pure Co sample), CCNA shows the maximum CDT modulation magnitude of ~ 0.35 degree at $\lambda \approx 750$ nm. This modulation amplitude is in the same order of magnitude with up-to-date magneto-chiroptical devices.[141-144, 154] As C_{Co} decreases, the MCDT magnitude at this peak decreases in almost a linear fashion to null (as in pure Ag CCNA sample, see **Figure 5.5e**). However, at $\lambda_1 \approx 660$ nm, there appears a peak. To gain a quantatative understanding, the $MCDT_N$ magnitude of different CCNA samples at two local peaks at, $\lambda_1 \approx 660$ nm and $\lambda_2 \approx 760$ nm, as well as at the EOT wavelength $\lambda_3 \approx 850$ nm are plotted as a function of C_{Co} in **Figure 5.6b**. While the magnitudes of $MCDT_N$ at $\lambda_2 \approx 760$ nm and $\lambda_3 \approx 850$ nm decrease gradually when C_{Co} decreases, it behaves differently at the Wood's anomaly. At λ_1, the $CCNA_{30}$ and $CCNA_{50}$ samples yield even more $MCDT_N$ than that of $CCNA_{100}$ sample. This peak also appears to be sharper with higher concentration of Ag, as can be seen in the inset of **Figure 5.6a,** which is consistent with our previous reports on enhanced Faraday rotation at the plasmonic resonance.[83] The different behavior at λ_1 can be explained by the enhancement of local electric field due to the Wood's anomaly in comparison to that of the $CCNA_{100}$ sample, which comes from the samples with a high ratio of Ag component (> 50 %V).

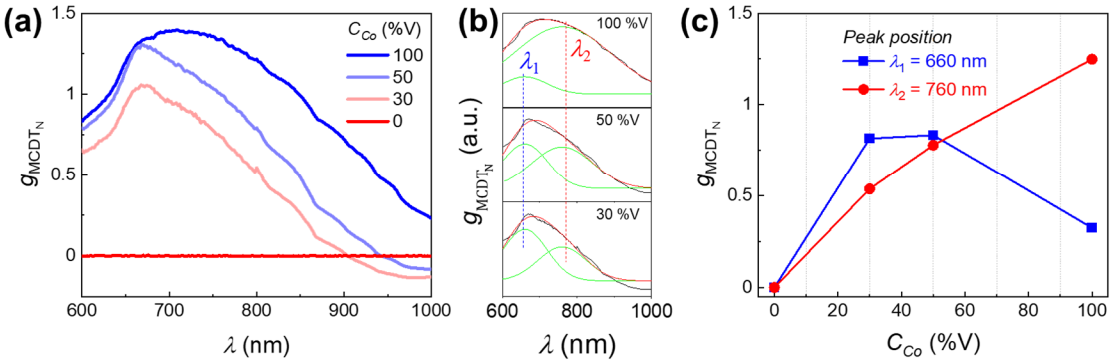

Figure 5.7. (a) $g_{\mathrm{MCDT_N}}$ spectra of Co CCNA with different C_{Co} and (b) the fitting of these spectra with two peaks at λ_1 and λ_2. (c) The plots of the $g_{\mathrm{MCDT_N}}$ magnitudes of peak λ_1, λ_2 in (b), as a function of C_{Co}.

We further obtained the asymmetry factor $g_{\mathrm{MCDT_N}}$ of CCNA sample, which can be calculated by the following equation,

$$g_{\mathrm{MCDT_N}} = \frac{g_{\mathrm{MCDT}}}{C_{Co}} \times 100 = \frac{1}{C_{Co}} \frac{\mathrm{CDT}(+B) - \mathrm{CDT}(-B)}{T_{unpolarized}} \times 100,$$

where CDT(±B) is the CDT signal measured at an external magnetic field of B, $T_{unpolarized}$ is the unpolarized optical transmission, and C_{Co} (%V) is the volume concentration of Co. The obtained $g_{\mathrm{MCDT_N}}$ spectra for different C_{Co} are presented in the **Figure 5.7a**. For the $\mathrm{CCNA_{100}}$ sample, a broad $g_{\mathrm{MCDT_N}}$ peak at $\lambda \approx 710$ nm is observed, as this peak is a combination of two peaks: the intrinsic $\mathrm{MCDT_N}$ peak at $\lambda_2 \approx 760$ nm, and the peak raised by the low transmission ($T_{unpolarized}$) at Wood's anomaly $\lambda_1 \approx 660$ nm. As the

composition of Ag is increased and C_{Co} = 50 %V, the magnitude of the peak at $\lambda_2 \approx 760$ nm decreases and the peak at $\lambda_1 \approx 660$ nm emerges with an unchanged magnitude in comparison to that of the $CCNA_{100}$ sample. However, the magnitude of the $g_{\mathrm{MCDT_N}}$ peak at $\lambda_1 \approx 660$ nm furtherly drops in $CCNA_{30}$. In order to quantitatively evaluate the attribution of two peaks at λ_1 and λ_2 to the $g_{\mathrm{MCDT_N}}$ spectra with different C_{Co}, the broad peak is deconvoluted into two Gaussian peaks at λ_1 and λ_2, as presented in **Figure 5.7b**. The magnitude of peak λ_2, summarized in **Figure 5.7c**, increases almost linearly with C_{Co}, which is due to the intrinsic MO response of the added Co component. On the other hand, the magnitudes of peak λ_1 of $CCNA_{50}$ and $CCNA_{30}$ samples are larger than that of $CCNA_{100}$ sample. The anomaly in the behavior of peak λ_1 can be ascribed to the plasmonic enhancement effect induced by the Wood's anomalies at λ_1. By compromising the C_{Co}, one can readily tune the intrinsic CDT signal as well as the magnitude of MCDT signal of CCNA sample.

5.3. Conclusions

In summary, we report the optical- and magneto-optics chiropticality of the CCNA sample, made from low-cost SNL technique and electron beam metal co-deposition. The CCNA sample shows strong intrinsic CDT signal, which emerge at the optical resonance induced by SPR. This CDT signal can be modulated magnetically by external magnetic field, which the modulation amplitude up to 0.35°. This result demonstrates the possibility to fabricate

large-scale active chiroptical metasurfaces using CCNA sample, which is promising for imaging and sensing applications.

5.4. Experimental Sections

Fabrication processes: The monolayer-coated substrates were loaded into a custom-built dual-source electron deposition system (Pascal Technology) and mounted on a motor-controlled rotated holder. The metal depositions were performed when the base pressure of the chamber reached 10^{-6} Torr, and the working pressure of chamber during the deposition was kept under 5×10^{-6} Torr. A thin layer of Ti (t_{Ti} = 3 nm, deposition rate = 0.05 nm/s) was first coated in order to increase the adhesion between composite thin films and the substrates. A composite layer was then formed by depositing Ag and Co simultaneously. The vapors of Ag and Co came from two separate crucibles, which are about 0.5 m apart from the substrate holder. The thicknesses and deposition rates of Ag and Co were measured independently by two separated quartz crystal microbalances (QCMs). The total deposition rate was set to be 0.60 nm/s. The volumic ratio of Co (C_{Co}) in the Ag-Co composite thin film and CCNA was controlled by adjusting the deposition rate of Ag and Co, and a series of samples with different C_{Co} was fabricated (C_{Co} = 0, 30, 50, and 100 (%V)). Afterward, the PS nanospheres were removed, and the substrates were subsequently washed with toluene, isopropyl alcohol, and deionized water to remove residual PS. Before any characterizations, the CCNA samples were stored inside a M.

Braun glovebox system filled with N_2 (the concentrations of O_2 and H_2O are less than 0.1 ppm) to minimize potential oxidation effects.

Morphology and composition characterization: The morphologies of CCNAs were characterized by an atomic force microscope (AFM, Park NX10), and all the AFM images were analyzed by XEI - Image Processing and Analysis Software. The crystallinities of the composite materials were investigated by an X-ray diffractometry (XRD) with a PANalytical X'Pert PRO MRD X-ray diffractometer at a fixed incident angle of 2.5°.

CHAPTER 6

HYDRIDE COMPOSITE NANOPATCHY ARRAYS FOR MANGETO-OPTICAL HYDROGEN SENSOR

In this Chapter, we explore an interesting an application of composite-based MO device: hydrogen sensing.

6.1. Introduction

Hydrogen fuel is a key energy carrier of the future, and it is one of the most practical alternatives to fossil fuel-based chemical storage, with a high theoretical energy density and universality of sourcing.[155] However, significant challenges remain with respect to the safe deployment of hydrogen fuel sources and therefore its widespread adoption.[156] For hydrogen leakage detection and concentration controls, it is essential that hydrogen sensors have good stability, high sensitivity, rapid response time, and most importantly be "spark-free".[157-158] High performance hydrogen sensors are, however, not only of importance in future hydrogen economy but also the chemical industry,[159] food industry,[160-161] medical applications,[162] nuclear reactors,[163] and environment pollution control.[164]

Numerous optical hydrogen sensors based on hydride-forming metal plasmonic nanostructure have been explored.[165-166] Pd is the most common hydriding metal for sensor

applications due to its rapid response, room temperature reversibility, and relative inertness.[167] However, pure Pd nanoparticles suffer from the coexistence of an α-β mixed phase region, inducing hysteresis and hence non-specific readout and limited reaction rate.[166, 168-169] It is possible to minimize this hysteresis and boost the reaction kinetics through the incorporation of alloying metals, such as Co, Au, or Ag.[165-166, 170] It has been believed that the enhanced reaction kinetics in the alloying metal hydrides is associated with the reduction of the enthalpy of formation due to the reduced abrupt volume expansion/contraction occurring in smaller mixed phase regions, resulting in a reduction of energy barrier for hydride formation/dissociation, and the improved diffusion rate upon (de)hydrogenation.[166, 169, 171-174] Synergistically with material design, various sensing nanostructures have been engineered to minimize the volume-to-surface ratio (VSR) of the sensor, a critical condition for achieving fast response time and low hysteresis.[166] These structures include nanostripes,[175] nanoholes,[176-177] lattices,[177] nanobipyramids,[178] hemispherical caps,[177] nanowires, mesowires,[179] and chiral helices.[180-181] Moving beyond metals, other materials such a polymers can be incorporated, as Nugroho *et al.*[165] recently demonstrated, significantly boosting the sensitivity and response time of a Pd-based nanosensor. Along with downsizing the active material layer, the benchmark response time of 1 s at 1 mbar H_2 and 30 °C has been achieved,[165] however optical contrast was sacrificed. As a result, sub-second response time and ppm limit of detection (LOD) have not been achieved in a single sensor.

In this Chapter, we demonstrate a compact magneto-optical (MO) hydrogen sensing platform with the fastest response reported to date and part-per-billion (ppb) LOD. The sensor is comprised of Pd-Co nano-patchy (NP) arrays with a magnetic circular dichroism (MCD) readout. These hexagonally-packed nano-arrays are generated by facile single metal glancing angle deposition (GLAD) on polystyrene (PS) nanosphere monolayers. This fabrication process requires just one deposition step with no post-processing required, simplifying scale-up and reducing costs. By coating a Teflon AF (TAF) polymer layer, the response time of the metasurfaces was reduced below 0.5 s from 1-100 mbar of H_2 partial pressure, surpassing the strictest requirements for H_2 sensing while preserving excellent accuracy (<3% full scale) and 700 ppm LOD. In a broader perspective, our work illustrates evolution in hydrogen gas sensor technologies through rational topological design and targeted integration of non-traditional materials, such as polymers and active alloying elements. These concepts are universal for promoting strong interactions between gas and materials and may be generally applied to advance sensor and catalyst development, among others.

6.2. Results and Discussion

We designed and fabricated the magnetic hydride hydrogen sensor using a template of hexagonal arrays nanosphere monolayer (diameter D = 200 nm), as illustrated in **Figure 6.1**a (see **Experimental Section**). The nanoarchitecture of the sensor consists of $Pd_{67}Co_{33}$ composite hemispherical nano-patchy (NP) on top of hexagonal closed-packed nanosphere

monolayer, which was verified by scanning electron microscopy (SEM) and energy-dispersive spectroscopy (EDS) elemental mapping. Using ultra-high-resolution SEM (SU-9000, Hitachi), we revealed the morphology of the NP sensor, which consists of many sub-10-nm granules (**Figure 6.1b** and **c**). These granules allocate and cover fully the top surface of the polystyrene sphere, and have an average equivalent diameter of 9.0 ± 2.8 nm (**Figure 6.1**c, inset), which is consistent with the observations of film morphologies presented in our previous work.[182] In addition, EDS elemental mapping shows an uniform distribution of Pd and Co on the top on nanosphere (**Figure 6.1d**) and confirms an ratio of Pd over Co of 64:36, which is in agreement with the 67:33 ratio obtained controlling deposition rate and thickness.

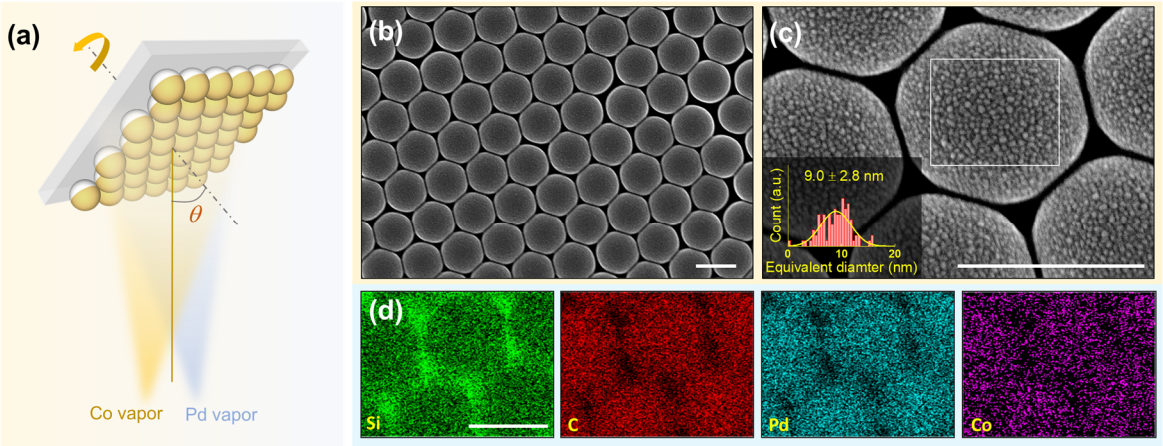

Figure 6.1. (a) Schematic of the fabrication process. (b) A top-view SEM image of PdCo nano-patchy (NP). (c) An ultra-high-resolution SEM micrograph showing morphology of NP sample. Inset: grain size analysis for the area (denotes by a white-

border rectangle) on the top of a nanosphere. (d) EDS elemental maps of NP samples. All scale bars correspond to 200 nm.

6.2.1. PdCo NP Based MCD Hydrogen Sensor

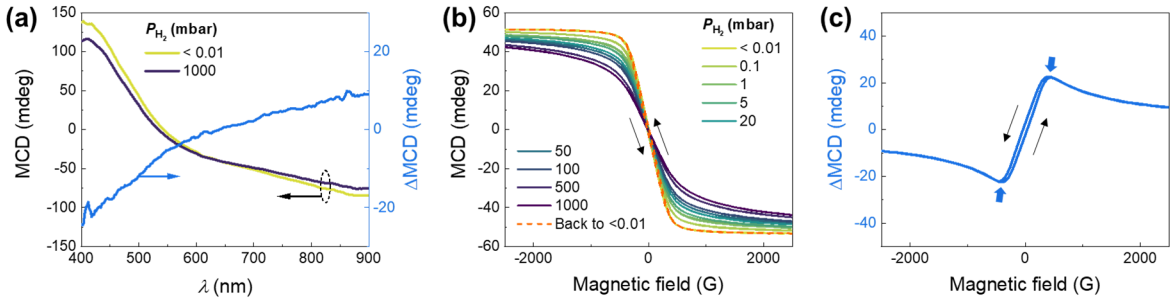

Figure 6.2. (a) MCD spectra $MCD_{1000\ mbar}$ and $MCD_{0\ mbar}$ of NP sample, measured at P_{H_2} = 1000 mbar and < 0.01 mbar, respectively, and ΔMCD = $MCD_{1000\ mbar}$ − $MCD_{0\ mbar}$. (b) MCD hysteresis loops of NP at λ = 450 nm, measured under several H_2 pressures and vacuum (before and after exposed to H_2). (c) ΔMCD hysteresis loop shows maxima changes of MCD signal at ~ ±380 G. Colored arrows indicate ΔMCD maxima. Black arrows in (b) and (c) denote the scanning magnetic field direction.

Among several MO indicators such as Faraday effect (FE) and magneto-optical Kerr effect (MOKE), we chose magnetic circular dichroism (MCD) as a hydrogen sensing readout signal, since the MCD of glass substrate and PS monolayer is negligible at an external magnetic field of **B** < 3000. The MCD spectra of NP sample (taken at **B** = 2600 G, see Experimental Section for more details) is plotted in **Figure 6.2**a, shows a decrease of MCD signal when the wavelength λ increases up to $\lambda \approx$ 535 nm. The MCD signal

approaches zero when $\lambda_{zero} \approx 535$ nm, and the sign of MCD flips when $\lambda > \lambda_{zero}$. There exists a kink near $\lambda_{kink} \approx 600$ nm, longer which the slope of MCD versus λ is noticeably smaller. It is worth noting that the spectral shape, amplitude, and its behaviors of NP follow the control PdCo composite thin film sample and are analogous to these of a Co thin film.[183]

Upon hydrogenation, the MCD magnitude versus the probe wavelength generally reduces, as can be seen in smaller slopes above and below λ_{kink} (**Figure 6.2a**). The MO signal change ΔMCD of NP sample (**Figure 6.2a**), where $\Delta MCD = MCD_{1000\ mbar} - MCD_{0\ mbar}$ is the difference of MCD signal when $P_{H_2} = 1000$ and < 0.01 mbar, is monotonically increase with the probe wavelength from negative to positive value while the ΔMCD in the control PdCo thin film sample fluctuates in a similar ΔMCD range (**Figure B1** in **Appendix B**). This ΔMCD difference between two samples might be due to the effect of sample morphology on the ΔMCD signal. We note that the MCDs of the glass substrate and a stand-alone nanosphere monolayer do not change upon their exposure to hydrogen.

Figure 6.2b shows the MCD magnetization curve with the probe wavelength $\lambda = 450$ nm, where the MCD magnitude is maximized and the MCD hysteresis loop as the external magnetic field was swept between **B** = −2600 G and +2600 G is well-defined. At very low P_{H_2} < 0.01 mbar or no hydrogen is present, the MCD hysteresis loop exhibits a typical soft magnetic ferromagnetic characteristic, with relatively small coercivity field (H_c < 10 G). In addition, the hysteresis curve shows an out-of-plane hard-axis behavior with almost no remanence, and saturation field is at relatively low magnetic fields (~600 G). Putting in

contrast with a control sample, MCD hysteresis of PdCo thin film (at λ = 450 nm) shows an easy-axis behavior with relatively large remanence, large H_c (> 400 G), and high saturation field (> 1000 G) (**Figure B2** in **Appendix B**). The behavioral differences between MCD hysteresis loops of NP and thin film can be attributed to several factors: (**i**) the curvature of nanosphere induces the alteration of film thickness/shape,[182] which significantly modify the magnetic properties of the sample;[184-185] (**ii**) morphologically, NP consists of numerous separated and confined nano-particles in hexagonal-lattice arrays with almost-zero/negligible magnetic coupling interactions, while in PdCo thin film, the continuity of the film supports the domain formation and domain wall shifting, especially when hydrogen is present [186]; (**iii**) the simultaneous deposition of Pd and Co on a curve substrate leads to formation of grains with tilted growth direction and lateral grain sizes (**Figure 6.1c**), which significantly influences to the magnetic properties of NP.[185]

The introduction of hydrogen instantly renders a reduction in MCD magnitude regardless of external magnetic field strength in the studying magnetic range, and the magnitude of the changes (ΔMCD) increase when P_{H_2} increases (**Figure 6.2b**). In addition, we observed an increasing slope in magnetic field versus MCD curve (from −500 G to +500 G) and the saturation field shifts to a higher field strength, which implies a reduction in out-of-plane component.[59] At P_{H_2} = 1000 mbar, the MCD signal still does not reach a fully-saturation at ~2500 G, while the remanence and coercivity remain small and

relatively the same as without hydrogen. More importantly, a reversible MCD signal was observed upon dehydrogenation (**Figure 6.2b**).

For a sensing application, we only consider an external magnetic field under which NP yields the maximum ΔMCD, and a strong magnetic field that fully magnetizes the sample is not necessary. **Figure 6.2c** presents ΔMCD of NP sample at different external magnetic fields, which is the signal difference between P_{H_2} = 1000 mbar curve and P_{H_2} < 0.01 mbar curve in **Figure 6.2b**. Interestingly, we found two ΔMCD maxima at relatively low magnetic field of ±380 G (**Figure 6.2c**, colored arrows). In addition, a narrow hysteresis in ΔMCD magnetization loop which could instigate non-specific sensor readout can be seen at a low magnetic field range (< 380 G), however no hysteresis is observed at 380 G or stronger magnetic field. We therefore set a constant external magnetic field of either – 380 G or +380 G for all sensing characterizations of MCD NP hydrogen sensor, in order to obtain the highest signal-to-noise ratio (SNR) and high sensor accuracy. It is worth noting that this low magnetic field strength can be generated by using a low-priced commercialized permanent magnet, which significantly simplifies the sensor assembly as no high-power electromagnet required, making this sensing platform light-weight and cost-friendly.

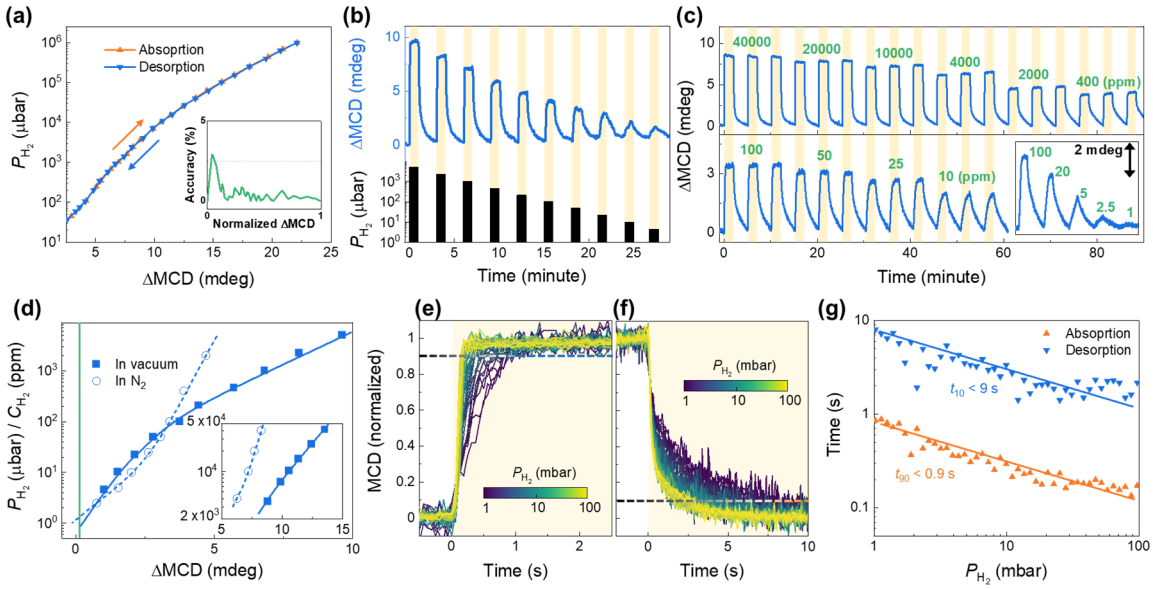

Figure 6.3. (a) MO hydrogen sorption isotherm of NP extracted at ΔMCD maxima (at +380 G). Inset: Sensor accuracy at specific normalized ΔMCD readout over hydrogen pressure range of 10^1 μbar to 10^6 μbar. (b) ΔMCD response of NP sensors to stepwise decreasing hydrogen pressure in the 5000 – 4.6 μbar range, measured at 1 Hz sampling frequency in a vacuum chamber. Shaded areas denote the periods where the sensor is exposed to hydrogen. (c) ΔMCD response of NP (1 Hz of sampling frequency) with different hydrogen concentration (C_{H_2}), measured in flowing nitrogen (400 ml/min). Shaded areas denote the periods where the sensor is exposed to hydrogen. (d) Measured ΔMCD response as a function of hydrogen pressure/concentration derived from (b) and (c). The green solid line denotes the defined LOD at 3σ = 0.12 mdeg. (e) Raw absorption kinetics response and (f) raw desorption kinetic response (with desorption

pressure of <0.08 mbar) of to varying H_2 pressure from 1000 to 1 mbar at 23 °C (16 Hz of sampling frequency). (g) Extracted absorption time (t_{90}) and desorption time (t_{10}), derived from (e) and (f).

MCD hydrogen sorption isotherm of NP sample is shown in **Figure 6.3a**, where the change of MCD signal ΔMCD versus P_{H_2} is extracted at $\lambda = 450$ nm and **B** = +380 G. The shape of MCD isotherm curve is generally similar to that of optical transmission isotherm,[182] and no hysteresis is observed at the measured pressure range. In addition, the plateau pressure shifts significantly to higher pressure than that of Pd NP [177, 182] and is above our probing pressure range, which is consistent with the previous observation for bulk PdCo alloys [187-188] and similar to the behaviors of the PdCu alloy nanoparticles.[189] As a result, our sensor yields very high sensor accuracy (<2.5 % full-scale, and <1 % when P_{H_2} > 1 mbar) and can be considered as "hysteresis-free" (**Figure 6.3a**, inset).

The very high surface coverage (> 90 %) of our NP [182, 190] along with the unique utilization of MCD as the hydrogen indicator allow stable and sizable sensor responses at very low concentrations of hydrogen, which could hardly be resolved by using other optical-based responses as a hydrogen indicator (such as transmission or reflection) with a PdCo NP sensor with Co content up to > 30 % at. In **Figure 6.3b**, PdCo NP sensor shows distinct MCD responses to step-wise pressure pulse of pure H_2 from 5000 to 4.6 μbar at 1 Hz sampling rate, and can clearly resolve the lowest hydrogen pulse with potential detection at even lower P_{H_2}. In flow mode with N_2 as a gas carrier (flow rate of 400

ml/min), PdCo NP sensor produces reproducible MCD responses with 3-cycles of each hydrogen concentration (C_{H_2}), ranging from 40000 ppm to 10 ppm (**Figure 6.3c**). Further tests show that NP sensors exhibits a distinct response from the background noise at C_{H_2} as low as <2.5 ppm (**Figure 6.3c**, inset). In order to quantitatively assess the limit of detection (LOD) of NP sensor, we performed the noise evaluations with different signal sampling frequency and obtained an experimental signal noise σ = 0.04 mdeg at 1 Hz. Hence, by defining the LOD as 3σ = 0.12 mdeg, we extrapolated that the LOD is <1 μbar with pure H_2 and <1.5 ppm of H_2 in N_2 (**Figure 6.3d**). It is worth noting that the PdCo NP sensor shows different MCD sensitivities in two different cases (pure H_2 in vacuum and H_2 in an inert gas), especially when P_{H_2} (C_{H_2}) > 100 μbar (ppm), which has not been seen by using optical transmission [182] or in sensors using other optical readout.[165, 189, 191] Therefore, a calibration step for the environment in which the sensor operates is required for a real-life application.

Among all of the performance target for automotive hydrogen safety sensors released by the US Department of Energy,[192] the sensor response time target of t_{90} < 1 s (t_{90}, the time required to reach 90% of the final equilibrium response) is one of the most crucial and challenging target to achieve. Indeed, only a few of optical hydrogen sensor has explicitly demonstrated this capability at $P_{H_2} \leq 1$ mbar (or $C_{H_2} \leq 0.1$ %V) and room temperature.[165, 182, 193] In this work, we employed two main strategies (**i**)-(**ii**) to bring the response time t_{90} to under 1-s benchmark, as well as to minimize the recovery time t_{10} (the time required to

reach 10% of the signal with releasing pressure of $P_{H_2} \leq 0.08$ mbar). (**i**) The kinetics of (de)hydrogenation is improved significantly by the incorporation of Co, as PdCo NP remains in α-phase over the pressure region of interest and avoids the α- to β-phase transition which requires longer equilibrium times.[182] (**ii**) The unique nanoarchitecture of NP and flexibility of fabrication method allows to reduce the volume-to-surface ratio (VSR) facilely and effectively, which is highly desired for faster absorption/desorption kinetic rate. By reducing nanosphere size from D = 500 nm down to 200 nm, t_{90} was accelerated by a factor of ~ 2.5, and the t_{90} of NP with D = 200 nm is about an order of magnitude faster than that of control thin film. The raw absorption/desorption kinetics of PdCo NP sensor (**Figure 6.3e** and **f**) and the extracted t_{90}/t_{10} (**Figure 6.3g**) show < 0.9 s (< 9 s) for absorption (desorption) times to varying H_2 pressure pulses ranges from 100 to 1 mbar, respectively. The pressure dependent response/recovery time of NP sensors follows the power law [165] with similar slopes, as can be seen by an near-linear dependence between $\log(t_{90})$ or $\log(t_{10})$ versus $\log(P_{H_2})$. We highlight that the LOD is preserved at < 1.5 ppm in the same system, and these performances place our PdCo NP system among the fastest and most sensitive optical-based hydrogen sensors, and this is one of very few hydrogen sensing platforms can achieve sub-second response and ppm-LOD in a single sensor.[182]

Summarily, in this first half of our study we have established the usages of MO signal (*i.e.* MCD) for hydrogen sensing using NP metasurfaces, which demonstrates impressive sensing metrics such as sub-second response time and ppm-LOD. Nevertheless, the

uniqueness of our system opens many possibilities for improvements. Thus, in the second half of the work, we reveal some strategies to experimentally improve these already impressive metrics, by using sample stacking and polymer coating. The implementation of this sensor platform for real-life application is also evaluated by rigorous tests with aging effect, interference gases, and moisture.

6.2.2. Sensor Stacks

Enhancing the sensor signal as well as improving LOD without vitiating the fast response time is challenging, since it requires a higher volume of active materials (*e.g.* thicker sensing layers, or higher surface coverage) which normally associates with a higher VSR (slower sorption kinetics) or necessitates of changing sensor nanoarchitecture.[182] Here, we propose a hydrogen sensor platform consists of a multilayer of NP-on-nanosphere-monolayer. This multilayer structure can be realized by transferring monolayers to other substrates by using water-floating,[194] scotch-tape,[177] sonicating and recasting, or just by simply stacking multiple NP sensors on top of each other (**Figure 6.4a**). We hypothesize that (**i**) hydrogen molecules can easily and rapidly penetrate through the porous nanosphere hexagonal-pack and reach the sorption sites on the NP surface, along with an unchanged VSR, would preserve the fast response characteristic of an individual NP sensor; and (**ii**) the volume of sensing materials is multiplicated by number of stacking layers, n, results in n-fold enhancement in sensor signal and pushing LODs to a lower P_{H_2}/C_{H_2} as long as the light transmission is still sufficient for the MCD detection.

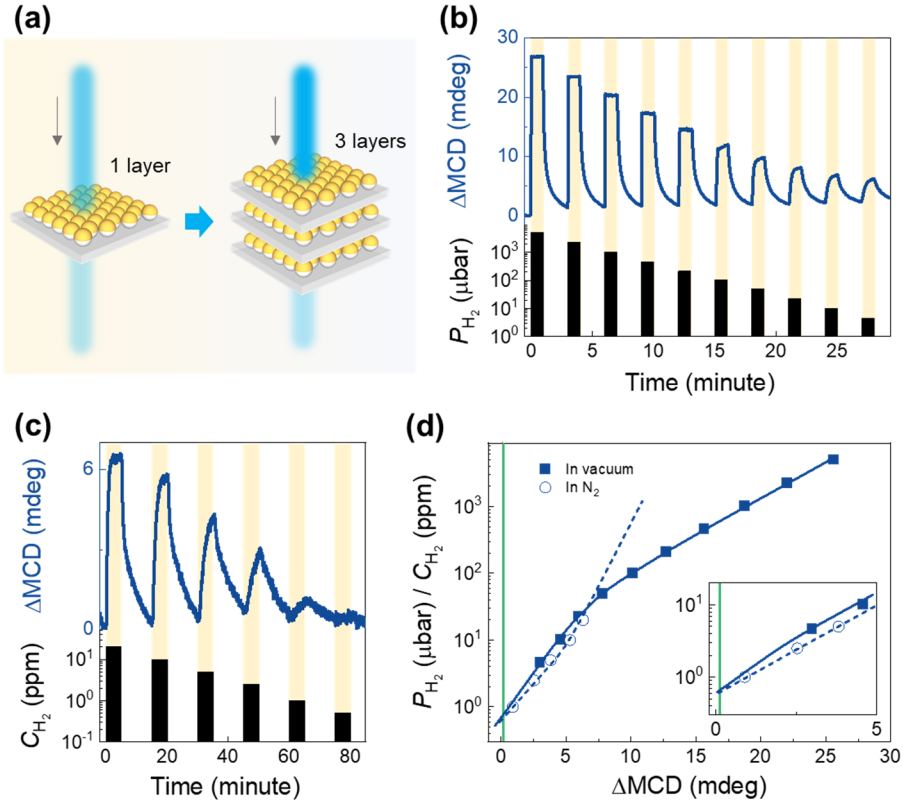

Figure 6.4. (a) A schematic illustrating a single-layer NP sensor and a triple-layer NP sensor. (b) ΔMCD response of triple-layer NP sensors to stepwise decreasing hydrogen pressure in the 5000 – 4.6 μbar range, measured at 1 Hz sampling frequency in a vacuum chamber. Shaded areas denote the periods where the sensor is exposed to hydrogen. (c) ΔMCD response of triple-layer NP sensors (1 Hz of sampling frequency) with different hydrogen concentration (C_{H_2}), measured in flowing nitrogen (400 ml/min). Shaded areas denote the periods where the sensor is exposed to hydrogen. (d) Measured ΔMCD response as a function of hydrogen pressure/concentration derived

from (b) and (c). The green solid line denotes the defined LOD at 3σ = 0.12 mdeg. Inset: a magnified view at low P_{H_2}/C_{H_2}.

We examine these hypotheses by testing a representative triple-layer NP sensor (**Figure 6.4a**) with standard response time and LOD measurements. In **Figure 6.4b**, we show the responses of triple-layer sensor to multiple step-wise hydrogen pulses (an identical test with a single-layer NP was presented in **Figure 6.3b**). The triple-layer NP sensor yields an approximately 3 times larger of MCD signal than that of single-layer NP sensor (at a certain P_{H_2}), and the lowest hydrogen pulses of 4.6 μbar (our system limit) is clearly resolved. In addition, this triple-layer NP sensor can resolve a 1-ppm hydrogen pulse in nitrogen (**Figure 6.4c**), which can hardly be seen with a single-layer NP (**Figure 6.3c**, inset). Consequently, we extrapolated that the LOD is < 700 nbar and < 700 ppb for pure H_2/vacuum and H_2 in nitrogen, respectively (**Figure 6.4d**).

It is expected that we can further lower down the LOD by having more sensing layers, however, the sensor platform requires higher power consumption as a trade-off. In particular, the transmission of a single-layer NP on glass substrate (at probing λ = 450 nm) is ~40 %. However, this power consumption rate can be significantly reduced by making the stack more transparent. For instance, exfoliating and transferring the monolayer can cut down the number of glass substrate used, or by using another monolayer template whose transparency at probing λ is higher.

6.2.3. PdCo NP/TAF and NP/TAF/PMMA Based MCD Hydrogen Sensor

Recent works on polymer-coated hydrogen sensors [165, 193, 195] and metal-organic framework-coated system [196-197] have provided meaningful insights on using coating layer for accelerating the hydrogen sorption kinetics. For instance, Nugroho *et al.* employed a 30-nm of polytetrafluoroethylene (PTFE) coating layer on PdAu alloy sensor to effectively reduce the activation barrier for hydrogen absorption from surface to subsurface sites, which results in sub-second response time.[165] To this end, we chose to coat a layer of Teflon-AF 2400 (TAF) for a potential improvement of sorption kinetic. In the same family of perfluorinated polymer as PTFE, TAF possesses high chemical resistances and hydrophobicity, while having a high gas permeability and low refractive index,[198] which are favorable for an optical-based sensing system.

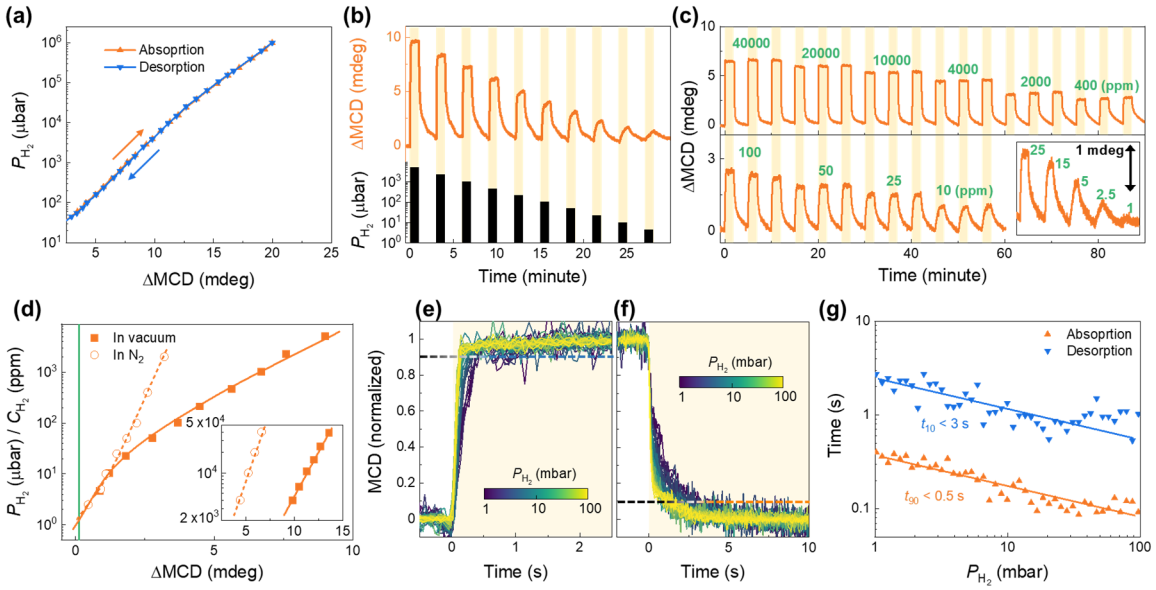

Figure 6.5. (a) MO hydrogen sorption isotherm of NP/TAF extracted at ΔMCD maxima. (b) ΔMCD response of NP/TAF sensors to stepwise decreasing hydrogen pressure in the 5000 – 4.6 μbar range, measured at 1 Hz sampling frequency in a vacuum chamber. Shaded areas denote the periods where the sensor is exposed to hydrogen. (c) ΔMCD response of NP/TAF (1 Hz of sampling frequency) with different hydrogen concentration (C_{H_2}), measured in flowing nitrogen (400 ml/min). Shaded areas denote the periods where the sensor is exposed to hydrogen. (d) Measured ΔMCD response as a function of hydrogen pressure/concentration derived from (b) and (c). The green solid line denotes the defined LOD at $3\sigma = 0.12$ mdeg. (e) Raw absorption kinetics response and (f) raw desorption kinetic response (with desorption pressure of <0.08 mbar) of to varying H_2 pressure from 1000 to 1 mbar at 23 °C (16 Hz of sampling frequency). (g) Extracted absorption time (t_{90}) and desorption time (t_{10}), derived from (e) and (f).

We next characterize the NP/TAF sensor as previously. We observe similar MO behaviors (MCD spectra, ΔMCD upon hydrogenation, and MCD magnetization) of coated sample, in comparison to these of uncoated sample. The extracted MCD sorption isotherm is summarized in **Figure 6.5a**, shows a hysteresis-free characteristic and comparable of signal level to uncoated sample. Further tests to examine the LOD of the NP/TAF sensor show that it can resolve at as low as 4.6 μbar pulses of pure H_2 in vacuum (**Figure 6.5b**) or 2.5 ppm of H_2 pulse in N_2 gas carrier (**Figure 6.5c**). From the experimental results, we

extrapolated that the LOD is ~ 1 μbar with pure H_2 and < 1.5 ppm of H_2 in N_2, which is on par with the uncoated NP sensor (**Figure 6.5d**). Notably, the sorption times of NP/TAF system are remarkably accelerated (**Figure 6.5e** and **f**). Three notable features are underlined (**Figure 6.5g**): (**1**) the t_{90} at P_{H_2} = 1 mbar is ~ 0.45 s, which is 2-time faster than any optical hydrogen sensors under similar conditions;[165, 182, 193] (**2**) the t_{90} at P_{H_2} = 40 mbar (~ 4 vol%) is < 0.1 s, which is nearly twice as fast as any optical hydrogen sensors under similar conditions;[170, 189] and (**3**) with the recovery times t_{10} with P_{H_2} = 1−100 mbar are < 3 s, with t_{10} at P_{H_2} = 40 mbar (~ 4 vol%) is only 1 s, NP/TAF is one of the fastest sensors under similar conditions.[191] Along with the ppm-LOD, this NP/TAF sensing platform represents the current state of the art in hydrogen sensing.

Another important aspect of a hydrogen sensor is the resistance toward the poisonous gas species such as CO, which exists with a trace level in the ambient air. Long-term exposure to these poisonous gases significantly degrades sensor performance (such as reducing sensitivity, accuracy, and slowing down the sensor response), which eventually shortens the lifetime of the sensor.[191] As TAF is well-known for its high gas permeability and poor selectivity,[199] it is expected that NP sensor is not fully protected by the TAF coating layer toward the deactivation gases such as CO. To overcome this drawback, we encapsulate the NP/TAF with a polymer layer of PMMA (see **Experimental Section**), as PMMA has been demonstrated as an excellent hydrogen selective membrane.[165, 182, 200-201]

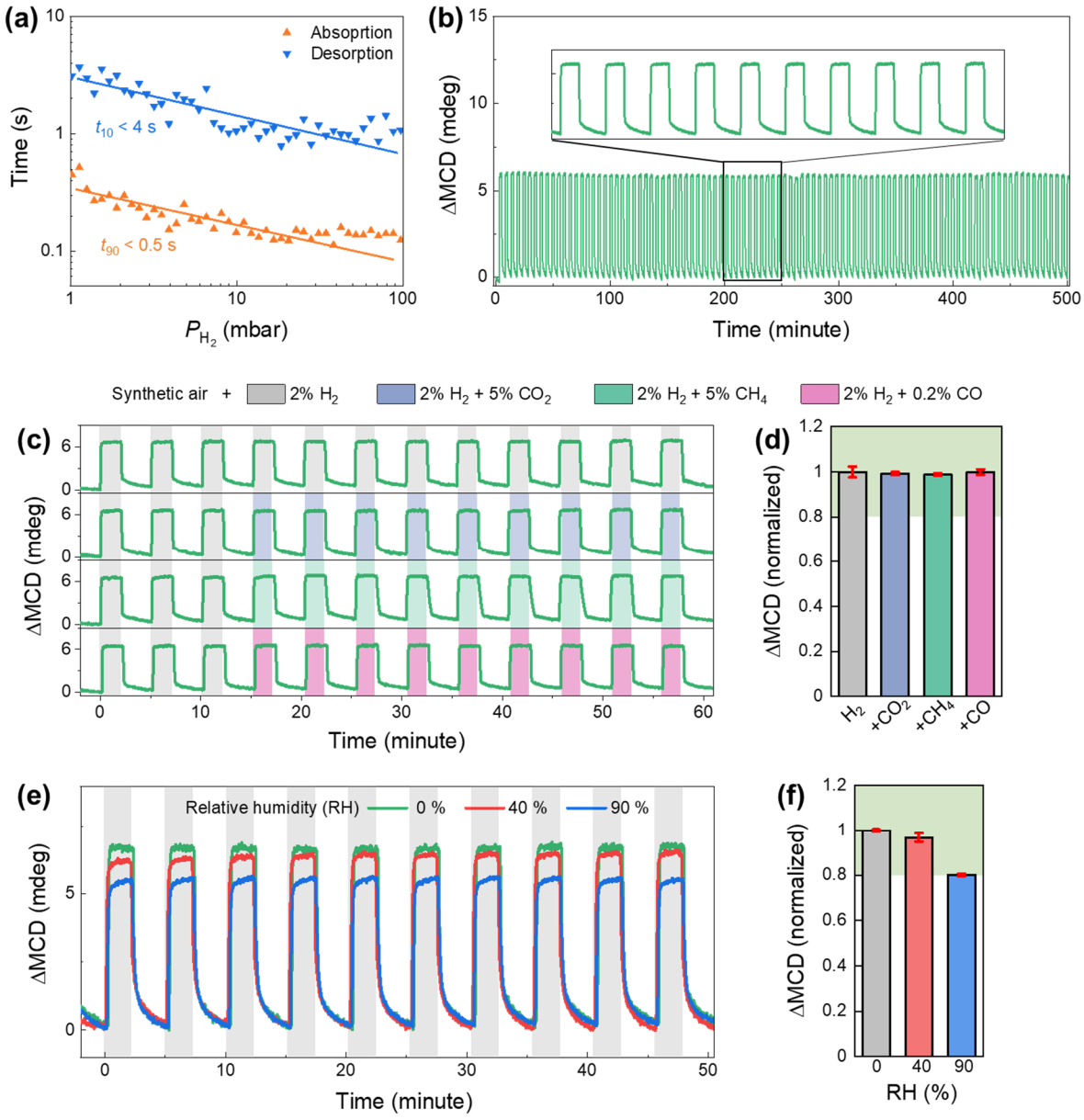

Figure 6.6. (a) Extracted absorption time (t_{90}) and desorption time (t_{10}) of NP/TAF/PMMA sensor. (b) ΔMCD response of NP/TAF/PMMA sensor upon 100 cycles of 2% H_2 in synthetic gas (400 ml/min). (c) Time-resolved ΔMCD response of

NP/TAF/PMMA sensor to 3 pulses of 2% H_2 followed by 9 pulses of 2% H_2 + 5% CO_2, 2% H_2 + 5% CH_4, 2% H2 + 0.2% CO; and (d) normalized sensor signal to the one obtained with 2% H_2 in syntheic gas flow. The error bars denote the standard deviation from 9 cycles. (e) Time-resolved ΔMCD response of NP/TAF/PMMA sensor to 10 pulses of 2% H_2 with different relative humidiy (RH) of 0-90% and (f) normalized signal to the one obtained with 2% H_2 in dry condition. All measurements were performed at 23 °C, using synthetic gas as carrier gas. The green shaded areas in (d) and (f) denote the ±20% deviation limit from the normalized ΔMCD response with 2% H_2.

We then performed an identical sensing characterization for this tri-layer sensor. Remarkably, we observed essential no change in t_{10} and t_{90} of NP/TAF/PMMA in comparison to NP/TAF sample (**Figure 6.6a**), which implies that (**i**) coating a thin layer of PMMA does not block/slow-down H_2 reaching/leaving the sorption sites on PdCo NP and (**ii**) the ultrafast response time is ascribed to the reduced activation barrier induced at the TAF/PdCo interface.[165] On the other hand, a notable performance which needs to be emphasized is the LOD of < 0.9 μbar of pure H_2 in vacuum and ~2 ppm of H_2 in N_2.

Further rigorous tests have been carried out on NP/TAF/PMMA tandem to assess the operation in practical condition, such as sensing in more realistic gas carrier like synthetic air, under interferences from toxic gases (CO, CO_2, CH_4) and moisture. The tandem sensor shows a great stability without the sign of degradation, upon > 500 of (de)hydrogenation

cycle (2% H_2 in synthetic air), and the first 100-cycles of a 5-month-old sample (stored in glove-box) are presented in **Figure 6.6b**. In addition, an excellent selectivity of NP/TAF/PMMA to high concentration pulses of CO (0.2%), CO_2 (5%), and CH_4 (5%) are observed, as in essence no sign of signal degradation is witnessed upon 9 pulses of gas exposure (**Figure 6.6c** and **d**). We note that, the CO_2 and CH_4 selectivity of the system might come from intrinsic resistances of PdCo materials,[182] and further enhanced by the selective PMMA coating. Furthermore, NP/TAF/PMMA shows a great tolerant toward the humidity, as the absolute response of the sensor remains within the ± 20% deviation limit [202] up to a high relative humidity (RH) of 90%. Additionally, we highlight that by stacking this tandem sensor as presented above, it is possible to realize an exemplary optical hydrogen sensor platform with sub-0.5-second response, ppb-LOD, and robustness against interfering gases and moistures.

6.3. Conclusions

In summary, we have demonstrated a method to produce a class of rapid-response, highly sensitive, and accurate MO Pd-Co composite hydrogen sensors through glancing angle deposition on PS-nanospheres. It is facile to tune these metasurface sensors through simple alloying, angle of deposition, or film thickness, which dictates the qualitative nature, quantitative metrics, and hysteresis of the response. By encapsulating the NP sensor with TAF and PMMA, the sensor response time (t_{90}) at 1 mbar is less than 0.5 s, which is the fastest response ever reported at the critical H_2 concentration required for leak detection.

Additionally, these sensors readily detect concentration as a low as <1 ppm in nitrogen, maintain high accuracy due to the hysteresis-free operation, and exhibit robustness against aging, temperature, moisture, and disturbance gases. These sensors demonstrate a viable path forward to spark-proof optical sensors for hydrogen detection applications.

6.4. Experimental Sections

*Morphology and composition characterization***.** Scanning electron microscopy (SEM) was performed with a Thermo Fisher Scientific (FEI) Teneo field emission scanning electron microscope (FESEM). Energy-dispersive spectroscopy (EDS) elemental mapping was performed with 150 mm Oxford XMaxN detector. Ultra-high-resolution SEM was performed with a SU-9000, Hitachi (with resolution of 0.4 nm at 30 kV).

*Hydrogen sensing measurement***.** All MO, optical isotherm, LOD, response/release time measurements are performed in a home-made vacuum chamber with two quartz windows.[177] The hydrogen pressure was monitored by three independent pressure transducers with different which cover the pressure range of 10^{-6} to 1.1 bar (two PX409-USBH, Omega and a Baratron, MKS). Optical transmission measurements were performed with an unpolarized collimated halogen lamp light source (HL-2000, Ocean Optics) and a spectrometer (USB4000-VIS-NIR-ES, Ocean Optics). The optical response/release time measurements were performed at 12.5 Hz sampling frequency (4 ms integration time with 10 averages). The LOD measurements were performed at 1.25 Hz sampling frequency (4 ms integration time with 100 averages), and $\Delta T/T$ responses were averaged over

wavelength range of λ = 500 – 660 nm for the best SNR. For LOD measurements in flow mode, ultra-high purity hydrogen gas (Airgas) was diluted with ultra-high purity nitrogen gas (Airgas) or synthetic gas (Airgas) to targeted concentrations by commercial gas blenders (GB-103, MCQ Instruments). The gas flow rate was kept constant at 400 ml/min for all measurements. All experiments (except the temperature-dependent experiments) were performed at constant 25 °C.

*FDTD calculations***.** FDTD calculations of Pd hydride NP samples were carried out using a commercial software (Lumerical FDTD Solutions).[109] The geometric parameters of Pd cap were obtained from MATLAB simulation. The mesh size of 2 nm × 2 nm × 2 nm was chosen. The refractive index of glass and PS was chosen to be 1.5 and 1.59, respectively, and the optical parameters of Pd and PdH_x were extracted from Ref. [203].

*PMMA coating***.** PMMA (Sigma Aldrich, 10 mg/ml dissolved in acetone by heating up the mix to 80 °C and cooling down to the room temperature, M_w = 15 000) was spin-coated on sensors at 5000 r.p.m. for 120 s followed by a soft baking at 85 °C on a hotplate for 20 minutes. Using the same coating process on a clean glass substrate results in a ~50 nm PMMA film, as measured by an atomic force microscope (NX-10, Park Instrument).

CHAPTER 7

CONCLUSIONS AND FUTURE WORK

In this Dissertation, we have demonstrated that SNL together with electron beam co-evaporation technique are a powerful technique-combination for preparing MOP nanostructures and devices. Accordingly, we reveals the strategies to produce consistently composite-based metasurfaces, including nanohole arrays, nano-triangle arrays, chiral nanohole arrays, and nanopatchy arrays.

Particularly, in **Chapter 3-4**, plasmonic nano-lattice such as nanohole arrays and nano-triangle arrays are examined. The nanostructures show strong composition-dependent magneto-plasmonic property. In fact, both experimental and FDTD numerical results show that the MO response is strongly related to the plasmonic property. The magneto-optics response of these magneto-plasmonic systems behave differently, depending on the nature of the plasmon resonance that the system supports (*i.e.* SPP wave in the nanohole array or LSPR wave in the nanotriangle array), and by adjusting the Co content, their MOP performances can be maximized. In **Chapter 5**, we introduce the inplane symmetry breaking to the nanohole array structure by a glancing angle deposition. The chiral nanohole arrays now show a strong intrinsic chiroptical response, which is enhanced strongly by SPR when Ag is a major component. On the other hand, the Co component

allows for magnetic tuning circular dichroism, with the maximum modulation amplitude up to 0.35°. In **Chapter 6**, we explore an interesting an application of composite-based MO device: hydrogen sensing, by alloying Co with a hydride-forming metal of Pd. The nano-patchy hydrogen sensor shows a rapid-response and is highly sensitive, and its performances surpasses any existing hydrogen sensor in the literature.

There are many possibilities to develop the works presented in this Dissertation. It would be interesting to investigate the MOP of other composite chiral nanostructures made by SNL such as nano-fan,[146] nano-spring,[204] chiral-stack,[205] etc. These nanostructures support LSPR and are expected to give a better magneto-plasmonic enhancement in comparison to that of nanostructures that support SPP mode.[45, 80] For the MO hydrogen sensors, adding noble metals (Ag or Au) in Pd-Co composite to form a ternary Ag-Pd-Co, Au-Pd-Co or Pd-Co/Ag(Au) bilayer could be an interesting improvement, as plasmonic functionality can give a great enhancement in signal response and improve sensing SNR.

REFERENCES

1. Faraday, M., Experimental researches in electricity. *Philosophical Transactions of the Royal Society of London* **1846,** (136), 1-20.

2. Faraday effect. https://en.wikipedia.org/wiki/Faraday_effect.

3. Pineider, F.; Sangregorio, C., Nanomaterials for magnetoplasmonics. In *Novel Magnetic Nanostructures*, Elsevier: 2018; pp 191-220.

4. Zvezdin, A. K.; Kotov, V. A., *Modern magnetooptics and magnetooptical materials*. Institute of Physics Pub: Bristol : Philadelphia, Pa, 1997; p 386.

5. Sun, C. Magneto-optical spectroscopy of novel ferromagnetic materials. 2010.

6. Kerr, J., XLIII. On rotation of the plane of polarization by reflection from the pole of a magnet. *The London, Edinburgh, and Dublin Philosophical Magazine and Journal of Science* **1877,** *3* (19), 321-343.

7. Armelles, G.; Cebollada, A.; García-Martín, A.; González, M. U., Magnetoplasmonics: Combining Magnetic and Plasmonic Functionalities. *Adv. Opt. Mater.* **2013,** *1* (1), 10-35.

8. Mason, W. R., *A Practical Guide to Magnetic Circular Dichroism Spectroscopy*. 2007; p 223.

9. Hamrle, J. Magneto-optical determination of the in-depth magnetization profile in magnetic multilayers. Université Paris Sud-Paris XI, 2003.

10. Kuch, W.; Schäfer, R.; Fischer, P.; Hillebrecht, F. U., *Magnetic microscopy of layered structures*. Springer: 2015.

11. Bruno, P.; Suzuki, Y.; Chappert, C., Magneto-optical Kerr effect in a paramagnetic overlayer on a ferromagnetic substrate: A spin-polarized quantum size effect. *Phys. Rev. B* **1996,** *53* (14), 9214.

12. Kubo, R., Statistical-mechanical theory of irreversible processes. I. General theory and simple applications to magnetic and conduction problems. *Journal of the Physical Society of Japan* **1957,** *12* (6), 570-586.

13. Jackson, J. D., Classical electrodynamics. American Association of Physics Teachers: 1999.

14. Floess, D.; Weiss, T.; Tikhodeev, S.; Giessen, H., Lorentz Nonreciprocal Model for Hybrid Magnetoplasmonics. *Phys. Rev. Lett.* **2016,** *117* (6).

15. Weber, M. J., *CRC handbook of laser science and Technology supplement 2: optical materials*. CRC press: 1994; Vol. 8.

16. Freiser, M., A survey of magnetooptic effects. *IEEE Trans. Magn.* **1968,** *4* (2), 152-161.

17. Ngo, T.-D., *Composite and Nanocomposite Materials: From Knowledge to Industrial Applications*. BoD–Books on Demand: 2020.

18. Chawla, K. K., *Composite materials: science and engineering*. Springer Science & Business Media: 2012.

19. Ferreira, A. D. B. L.; Novoa, P. R. O.; Marques, A. T., Multifunctional Material Systems: A state-of-the-art review. *Composite Structures* **2016,** *151*, 3-35.

20. Lendlein, A.; Trask, R. S., Multifunctional materials: concepts, function-structure relationships, knowledge-based design, translational materials research. *Multifunctional Materials* **2018,** *1* (1), 010201.

21. Hu, H.; Xin, J. H.; Hu, H.; Wang, X.; Miao, D.; Liu, Y., Synthesis and stabilization of metal nanocatalysts for reduction reactions–a review. *Journal of Materials Chemistry A* **2015,** *3* (21), 11157-11182.

22. Wu, Z.-S.; Zhou, G.; Yin, L.-C.; Ren, W.; Li, F.; Cheng, H.-M., Graphene/metal oxide composite electrode materials for energy storage. *Nano Energy* **2012,** *1* (1), 107-131.

23. Salernitano, E.; Migliaresi, C., Composite materials for biomedical applications: a review. *Journal of Applied Biomaterials and Biomechanics* **2003,** *1* (1), 3-18.

24. Kinsey, N.; DeVault, C.; Boltasseva, A.; Shalaev, V. M., Near-zero-index materials for photonics. *Nature Reviews Materials* **2019,** *4* (12), 742-760.

25. Choy, T. C., *Effective medium theory: principles and applications*. Oxford University Press: 2015; Vol. 165.

26. Hui, P. M.; Stroud, D., Theory of Faraday rotation by dilute suspensions of small particles. *Appl. Phys. Lett.* **1987,** *50* (15), 950-952.

27. Gehr, R. J.; Boyd, R. W., Optical properties of nanostructured optical materials. *Chemistry of materials* **1996,** *8* (8), 1807-1819.

28. You, C.-Y.; Shin, S.-C.; Kim, S.-Y., Modified effective-medium theory for magneto-optical spectra of magnetic materials. *Phys. Rev. B* **1997,** *55* (9), 5953.

29. Granovsky, A.; Kuzmichov, M.; Clerc, J. P., The Symmetrised Maxwell-Garnett Approximation for Magneto-Optical Spectra of Ferromagnetic Composites. *J. Magn. Soc. Jpn.* **1999,** *23* (1_2), 382-384.

30. Maier, S. A., *Plasmonics: fundamentals and applications*. Springer Science & Business Media: 2007.

31. Murray, W. A.; Barnes, W. L., Plasmonic materials. *Adv. Mater.* **2007,** *19* (22), 3771-3782.

32. Naik, G. V.; Kim, J.; Boltasseva, A., Oxides and nitrides as alternative plasmonic materials in the optical range. *Opt. Mater. Express* **2011,** *1* (6), 1090-1099.

33. Lakowicz, J. R., Plasmonics in biology and plasmon-controlled fluorescence. *Plasmonics* **2006,** *1* (1), 5-33.

34. Shahbazyan, T. V.; Stockman, M. I., *Plasmonics: theory and applications*. Springer: 2013.

35. Petryayeva, E.; Krull, U. J., Localized surface plasmon resonance: Nanostructures, bioassays and biosensing—A review. *Analytica chimica acta* **2011,** *706* (1), 8-24.

36. Qin, J.; Deng, L.; Kang, T.; Nie, L.; Feng, H.; Wang, H.; Yang, R.; Liang, X.; Tang, T.; Shen, J., Switching the Optical Chirality in Magnetoplasmonic Metasurfaces Using Applied Magnetic Fields. *ACS Nano* **2020,** *14* (3), 2808-2816.

37. Zubritskaya, I.; Maccaferri, N.; Inchausti Ezeiza, X.; Vavassori, P.; Dmitriev, A., Magnetic control of the chiroptical plasmonic surfaces. *Nano Lett.* **2017,** *18* (1), 302-307.

38. Temnov, V. V.; Armelles, G.; Woggon, U.; Guzatov, D.; Cebollada, A.; Garcia-Martin, A.; Garcia-Martin, J.-M.; Thomay, T.; Leitenstorfer, A.; Bratschitsch, R.,

Active magneto-plasmonics in hybrid metal–ferromagnet structures. *Nat. Photonics* **2010,** *4* (2), 107-111.

39. Banthí, J. C.; Meneses-Rodríguez, D.; García, F.; González, M. U.; García-Martín, A.; Cebollada, A.; Armelles, G., High magneto-optical activity and low optical losses in metal-dielectric Au/Co/Au–SiO2 magnetoplasmonic nanodisks. *Adv. Mater.* **2012,** *24* (10), OP36-OP41.

40. Maksymov, I. S., Magneto-plasmonic nanoantennas: Basics and applications. *Reviews in Physics* **2016,** *1*, 36-51.

41. Wurtz, G. A.; Hendren, W.; Pollard, R.; Atkinson, R.; Guyader, L. L.; Kirilyuk, A.; Rasing, T.; Smolyaninov, I. I.; Zayats, A. V., Controlling optical transmission through magneto-plasmonic crystals with an external magnetic field. *New J. Phys.* **2008,** *10* (10), 105012.

42. Ebert, H., Magneto-optical effects in transition metal systems. *Reports on Progress in Physics* **1996,** *59* (12), 1665.

43. Ferreiro-Vila, E.; González-Díaz, J. B.; Fermento, R.; González, M. U.; García-Martín, A.; García-Martín, J. M.; Cebollada, A.; Armelles, G.; Meneses-Rodríguez, D.; Sandoval, E. M., Intertwined magneto-optical and plasmonic effects in Ag/Co/Ag layered structures. *Phys. Rev. B* **2009,** *80* (12), 125132.

44. Yang, K.; Clavero, C.; Skuza, J. R.; Varela, M.; Lukaszew, R. A., Surface plasmon resonance and magneto-optical enhancement on Au–Co nanocomposite thin films. *J. Appl. Phys.* **2010,** *107* (10), 103924.

45. Luong, H. M.; Ai, B.; Zhao, Y.; Nguyen, T. D., Weak enhanced resonant Faraday rotation in pure cobalt plasmonic lattices: Thickness dependent Faraday rotation studies. *J. Magn. Magn. Mater.* **2018,** *468*, 79-84.

46. Belotelov, V. I.; Kreilkamp, L. E.; Akimov, I. A.; Kalish, A. N.; Bykov, D. A.; Kasture, S.; Yallapragada, V. J.; Venu Gopal, A.; Grishin, A. M.; Khartsev, S. I.; Nur-E-Alam, M.; Vasiliev, M.; Doskolovich, L. L.; Yakovlev, D. R.; Alameh, K.; Zvezdin, A. K.; Bayer, M., Plasmon-mediated magneto-optical transparency. *Nat. Commun.* **2013,** *4*, 2128.

47. Belotelov, V. I.; Akimov, I. A.; Pohl, M.; Kotov, V. A.; Kasture, S.; Vengurlekar, A. S.; Gopal, A. V.; Yakovlev, D. R.; Zvezdin, A. K.; Bayer, M., Enhanced magneto-optical effects in magnetoplasmonic crystals. *Nat. Nanotechnol.* **2011,** *6* (6), 370-376.

48. González-Díaz, J. B.; Sepúlveda, B.; García-Martín, A.; Armelles, G., Cobalt dependence of the magneto-optical response in magnetoplasmonic nanodisks. *Appl. Phys. Lett.* **2010,** *97* (4), 043114.

49. López-Ortega, A.; Takahashi, M.; Maenosono, S.; Vavassori, P., Plasmon induced magneto-optical enhancement in metallic Ag/FeCo core/shell nanoparticles synthesized by colloidal chemistry. *Nanoscale* **2018,** *10* (39), 18672-18679.

50. Jain, P. K.; Xiao, Y.; Walsworth, R.; Cohen, A. E., Surface Plasmon Resonance Enhanced Magneto-Optics (SuPREMO): Faraday Rotation Enhancement in Gold-Coated Iron Oxide Nanocrystals. *Nano Lett.* **2009,** *9* (4), 1644-1650.

51. Yao, H.; Shiratsu, T., Multipolar Surface Magnetoplasmon Resonances in Triangular Silver Nanoprisms studied by MCD Spectroscopy. *J. Phys. Chem. C* **2017,** *121* (1), 761-768.

52. Choi, B.; Xu, H.; Hajisalem, G.; Gordon, R., Localized surface plasmon resonance enhanced magneto-optical Kerr effect in Ni80Fe20 thin films coated with Au nanorods. *Appl. Phys. Lett.* **2018,** *112* (2), 022403.

53. Wang, L.; Clavero, C.; Huba, Z.; Carroll, K. J.; Carpenter, E. E.; Gu, D.; Lukaszew, R. A., Plasmonics and Enhanced Magneto-Optics in Core–Shell Co–Ag Nanoparticles. *Nano Lett.* **2011,** *11* (3), 1237-1240.

54. Armelles, G.; Cebollada, A.; García-Martín, A.; Montero-Moreno, J. M.; Waleczek, M.; Nielsch, K., Magneto-optical Properties of Core–Shell Magneto-plasmonic Au–Co(x)Fe(3 - x)O4 Nanowires. *Langmuir* **2012,** *28* (24), 9127-9130.

55. de Sousa, N.; Froufe-Pérez, L. S.; Sáenz, J. J.; García-Martín, A., Magneto-Optical Activity in High Index Dielectric Nanoantennas. *Sci. Rep.* **2016,** *6*, 30803.

56. Varytis, P.; Pantazopoulos, P. A.; Stefanou, N., Enhanced Faraday rotation by crystals of core-shell magnetoplasmonic nanoparticles. *Phys. Rev. B* **2016,** *93* (21), 214423

57. Chen, Q.; Wang, Q.; Wang, H.; Ma, Q.; Chen, Q., Surface Plasmon Resonance Enhanced Faraday Rotation in Fe3O4/Ag Nanoparticles Doped Diamagnetic Glass. *Plasmonics* **2017**.

58. Martín-Becerra, D.; García-Martín, J. M.; Huttel, Y.; Armelles, G., Optical and magneto-optical properties of Au: Conanoparticles and Co: Aunanoparticles doped magnetoplasmonic systems. *J. Appl. Phys.* **2015,** *117* (5), 053101.

59. Ctistis, G.; Papaioannou, E.; Patoka, P.; Gutek, J.; Fumagalli, P.; Giersig, M., Optical and Magnetic Properties of Hexagonal Arrays of Subwavelength Holes in Optically Thin Cobalt Films. *Nano Lett.* **2009,** *9* (1), 1-6.

60. Diwekar, M.; Kamaev, V.; Shi, J.; Vardeny, Z. V., Optical and magneto-optical studies of two-dimensional metallodielectric photonic crystals on cobalt films. *Appl. Phys. Lett.* **2004,** *84* (16), 3112-3114.

61. Sapozhnikov, M. V.; Gusev, S. A.; Rogov, V. V.; Ermolaeva, O. L.; Troitskii, B. B.; Khokhlova, L. V.; Smirnov, D. A., Magnetic and optical properties of nanocorrugated Co films. *Appl. Phys. Lett.* **2010,** *96* (12), 122507.

62. Rubio-Roy, M.; Vlasin, O.; Pascu, O.; Caicedo, J. M.; Schmidt, M.; Goñi, A. R.; Tognalli, N. G.; Fainstein, A.; Roig, A.; Herranz, G., Magneto-Optical Enhancement by Plasmon Excitations in Nanoparticle/Metal Structures. *Langmuir* **2012,** *28* (24), 9010-9020.

63. Melander, E.; George, S.; Caballero, B.; García-Martín, A.; Hjörvarsson, B.; Kapaklis, V.; Papaioannou, E. T., Thickness dependent enhancement of the polar magneto-optic Kerr effect in Co magnetoplasmonic nanostructures. *arXiv preprint arXiv:1611.00078* **2016**.

64. Papaioannou, E. T.; Fang, H.; Caballero, B.; Akinoglu, E. M.; Giersig, M.; García-Martín, A.; Fumagalli, P., Role of interactions in the magneto-plasmonic response at the geometrical threshold of surface continuity. *Opt. Express* **2017,** *25* (26), 32792-32799.

65. Papaioannou, E. T.; Kapaklis, V.; Melander, E.; Hjörvarsson, B.; Pappas, S. D.; Patoka, P.; Giersig, M.; Fumagalli, P.; Garcia-Martin, A.; Ctistis, G., Surface plasmons and magneto-optic activity in hexagonal Ni anti-dot arrays. *Opt. Express* **2011,** *19* (24), 23867-23877.

66. González-Díaz, J. B.; García-Martín, J. M.; García-Martín, A.; Navas, D.; Asenjo, A.; Vázquez, M.; Hernández-Vélez, M.; Armelles, G., Plasmon-enhanced magneto-optical activity in ferromagnetic membranes. *Appl. Phys. Lett.* **2009,** *94* (26), 263101.

67. Torrado, J. F.; González-Díaz, J. B.; Armelles, G.; García-Martín, A.; Altube, A.; López-García, M.; Galisteo-López, J. F.; Blanco, A.; López, C., Tunable magneto-photonic response of nickel nanostructures. *Appl. Phys. Lett.* **2011,** *99* (19), 193109.

68. Grunin, A. A.; Sapoletova, N. A.; Napolskii, K. S.; Eliseev, A. A.; Fedyanin, A. A., Magnetoplasmonic nanostructures based on nickel inverse opal slabs. *J. Appl. Phys.* **2012,** *111* (7), 07A948.

69. Fang, H.; Caballero, B.; Akinoglu, E. M.; Papaioannou, E. T.; García-Martín, A.; Cuevas, J. C.; Giersig, M.; Fumagalli, P., Observation of a hole-size-dependent energy shift of the surface-plasmon resonance in Ni antidot thin films. *Appl. Phys. Lett.* **2015,** *106* (15), 153104.

70. Rollinger, M.; Thielen, P.; Melander, E.; Östman, E.; Kapaklis, V.; Obry, B.; Cinchetti, M.; García-Martín, A.; Aeschlimann, M.; Papaioannou, E. T., Light Localization and Magneto-Optic Enhancement in Ni Antidot Arrays. *Nano Lett.* **2016,** *16* (4), 2432-2438.

71. Papaioannou, E. T.; Kapaklis, V.; Patoka, P.; Giersig, M.; Fumagalli, P.; Garcia-Martin, A.; Ferreiro-Vila, E.; Ctistis, G., Magneto-optic enhancement and magnetic properties in Fe antidot films with hexagonal symmetry. *Phys. Rev. B* **2010,** *81* (5), 054424.

72. Torrado, J. F.; Papaioannou, E. T.; Ctistis, G.; Patoka, P.; Giersig, M.; Armelles, G.; Garcia-Martin, A., Plasmon induced modification of the transverse magneto-optical response in Fe antidot arrays. *Phys. Status Solidi Rapid Res. Lett.* **2010,** *4* (10), 271-273.

73. Caballero, B.; García-Martín, A.; Cuevas, J. C., Generalized scattering-matrix approach for magneto-optics in periodically patterned multilayer systems. *Phys. Rev. B* **2012,** *85* (24), 245103.

74. Caballero, B.; García-Martín, A.; Cuevas, J. C., Faraday effect in hybrid magneto-plasmonic photonic crystals. *Opt. Express* **2015,** *23* (17), 22238.

75. Liang, H.; Liu, H.; Zhang, Q.; Fu, S.-F.; Zhou, S.; Wang, X.-Z., Giant enhancement of Kerr rotation in two-dimensional Bismuth iron garnet/Ag photonic crystals. *Chin. Phys. B* **2015,** *24* (6), 067807.

76. Maccaferri, N.; Inchausti, X.; García-Martín, A.; Cuevas, J. C.; Tripathy, D.; Adeyeye, A. O.; Vavassori, P., Resonant Enhancement of Magneto-Optical Activity Induced by Surface Plasmon Polariton Modes Coupling in 2D Magnetoplasmonic Crystals. *ACS Photonics* **2015,** *2* (12), 1769-1779.

77. Larson, S. R. Combinatorial Fabrication of Composite Nanostructures for Photocatalytic and Plasmonic Applications. University of Georgia, 2018.

78. Larson, S. R.; Luong, H.; Song, C.; Zhao, Y., Dipole Radiation Induced Extraordinary Optical Transmission for Silver Nanorods Covered Silver Nanohole Arrays. *J. Phys. Chem. C* **2019,** *123* (9), 5634-5641.

79. Larson, S.; Carlson, D.; Ai, B.; Zhao, Y., The Extraordinary Optical Transmission and Sensing Properties of Ag/Ti Composite Nanohole Arrays. *Physical Chemistry Chemical Physics* **2019**.

80. Luong, H. M.; Pham, M. T.; Ai, B.; Nguyen, T. D.; Zhao, Y., Magnetoplasmonic properties of Ag-Co composite nanohole arrays. *Phys. Rev. B* **2019,** *99* (22), 224413.

81. Luong, H. M.; Minh, P. T.; Nguyen, T.; Zhao, Y., Magneto-plasmonic properties of Ag-Co composite nano-triangle arrays. *Nanotechnology* **2019,** *30* (42), 425203.

82. Luong, H. M.; Pham, M. T.; Larsen, G. K.; Nguyen, T. D., Plasmonic sensing of hydrogen in Pd nano-hole arrays. *Plasmonics: Design, Materials, Fabrication, Characterization, and Applications XVII* **2019,** *11082*, 110821D.

83. Luong, H. M.; Pham, M. T.; Nguyen, T. D.; Zhao, Y., Enhanced Resonant Faraday Rotation in Multilayer Magnetoplasmonic Nanohole Arrays and Their Sensing Application. *J. Phys. Chem. C* **2019,** *123* (46), 28377-28384.

84. Mahan, J. E., *Physical vapor deposition of thin films*. 2000.

85. Zhao, Y., Dynamic shadowing growth and its energy applications. *Frontiers in Energy Research* **2014,** *2*, 38.

86. Ai, B.; Zhao, Y., Glancing angle deposition meets colloidal lithography: a new evolution in the design of nanostructures. *Nanophotonics* **2018,** *8* (1), 1-26.

87. Ambekar, J. D.; Panmand, R. P.; Sonawane, R. S.; Apte, S. K.; Hundiwale, D. G.; Kale, B. B., Preparation and magneto-optical properties of stable bismuth phosphate nanoparticles in phosphate glass. *RSC Adv.* **2015,** *5* (59), 48112-48117.

88. Atkinson, R. Magnetism in a New Light. http://www.hindsinstruments.com/wp-content/uploads/pem-10-MOKE.pdf.

89. Instrument, H. Magnetic circular dichroism (MCD) https://www.hindsinstruments.com/techniques/dichroism/magnetic-circular-dichroism/.

90. Temnov, V. V.; Razdolski, I.; Pezeril, T.; Makarov, D.; Seletskiy, D.; Melnikov, A.; Nelson, K. A., Towards the nonlinear acousto-magneto-plasmonics. *J. Opt.* **2016,** *18* (9), 093002.

91. Kravets, V. G.; Lapchuk, A. S., Enhancement of magneto-optical effects in magnetic nanoparticles near gold-dielectric surfaces. *Appl. Opt.* **2010,** *49* (26), 5013-5019.

92. David, S.; Polonschii, C.; Luculescu, C.; Gheorghiu, M.; Gáspár, S.; Gheorghiu, E., Magneto-plasmonic biosensor with enhanced analytical response and stability. *Biosens. Bioelectron.* **2015,** *63*, 525-532.

93. Lu, H. P.; Liu, C.; Qin, J.; Wang, C. T.; Zhang, Y.; Deng, L. J.; Bi, L., Enhanced magneto-optical Kerr effect and index sensitivity in Au/FexCo1-x magnetoplasmonic transducers. *Photonics Research* **2017,** *5* (5), 385-390.

94. Wang, S.-Y.; Zheng, W.-M.; Qian, D.-L.; Zhang, R.-J.; Zheng, Y.-X.; Zhou, S.-M.; Yang, Y.-M.; Li, B.-Y.; Chen, L.-Y., Study of the Kerr effect of CoxAg100−x granular films. *J. Appl. Phys.* **1999,** *85* (8), 5121-5123.

95. Ingram, W. M.; Han, C. Q.; Zhang, Q. J.; Zhao, Y. P., Optimization of Ag-Coated Polystyrene Nanosphere Substrates for Quantitative Surface-Enhanced Raman Spectroscopy Analysis. *J. Phys. Chem. C* **2015,** *119* (49), 27639-27648.

96. Larson, S.; Zhao, Y. P., Localized Surface Plasmonic Resonance and Sensing Properties of Ag-MgF2 Composite Nanotriangles. *J. Phys. Chem. C* **2018,** *122* (13), 7374-7381.

97. Henzie, J.; Barton, J. E.; Stender, C. L.; Odom, T. W., Large-area nanoscale patterning: chemistry meets fabrication. *Acc. Chem. Res.* **2006,** *39* (4), 249-57.

98. Ebbesen, T. W.; Lezec, H. J.; Ghaemi, H. F.; Thio, T.; Wolff, P. A., Extraordinary optical transmission through sub-wavelength hole arrays. *Nature* **1998,** *391* (6668), 667-669.

99. Kelf, T. A.; Sugawara, Y.; Cole, R. M.; Baumberg, J. J.; Abdelsalam, M. E.; Cintra, S.; Mahajan, S.; Russell, A. E.; Bartlett, P. N., Localized and delocalized plasmons in metallic nanovoids. *Phys. Rev. B* **2006,** *74* (24), 245415.

100. Raether, H., *Surface Plasmons on Smooth and Rough Surfaces and on Gratings*. 1988.

101. Maystre, D., Theory of Wood's Anomalies. In *Plasmonics*, Enoch, S.; Bonod, N., Eds. Springer Berlin Heidelberg: Berlin, Heidelberg, 2012; Vol. 167, pp 39-83.

102. Hajiaboli, A.; Kahrizi, M.; Truong, V. V., Optical behaviour of thick gold and silver films with periodic circular nanohole arrays. *J. Phys. D: Appl. Phys.* **2012,** *45* (48).

103. Kim, J. H.; Moyer, P. J., Thickness effects on the optical transmission characteristics of small hole arrays on thin gold films. *Opt. Express* **2006,** *14* (15), 6595-603.

104. Genet, C.; Ebbesen, T. W., Light in tiny holes. *Nature* **2007,** *445* (7123), 39-46.

105. Degiron, A.; Ebbesen, T. W., The role of localized surface plasmon modes in the enhanced transmission of periodic subwavelength apertures. *Journal of Optics a-Pure and Applied Optics* **2005,** *7* (2), S90-S96.

106. Rodrigo, S. G., Extraordinary Optical Transmission. In *Optical Properties of Nanostructured Metallic Systems*, Springer Berlin Heidelberg: Berlin, Heidelberg, 2012; pp 37-75.

107. Selinger, J. V., Ising Model for Ferromagnetism. In *Introduction to the Theory of Soft Matter*, Springer: 2016; pp 7-24.

108. Arora, A.; Ghosh, S.; Sugunakar, V., A mirror based polar magneto-optical Kerr effect spectroscopy arrangement. *Review of Scientific Instruments* **2011,** *82* (12), 123903.

109. FDTD Solutions. https://www.lumerical.com/.

110. Li, D.; Chen, L.; Lei, C.; Menendez, J. L.; Mallada, C.; Tang, Z.; Tang, S.; Du, Y., Plasmon-enhanced magneto-optical activity in a nanostructure with circle annular arrays. *J. Opt. Soc. Am. B* **2016,** *33* (5), 922.

111. SCHOTT glass data sheets, N-BK7. www.schott.com (accessed July).

112. Yan, Y.; Deng, C.; Yan, L.; Tang, Z.; Tang, S.; Xu, X., Composition dependence of magneto-optical response in Ag/Co dimer nanodot arrays. *J. Magn. Magn. Mater.* **2016,** *419*, 553-558.

113. Maccaferri, N.; Berger, A.; Bonetti, S.; Bonanni, V.; Kataja, M.; Qin, Q. H.; van Dijken, S.; Pirzadeh, Z.; Dmitriev, A.; Nogués, J., Tuning the magneto-optical response of nanosize ferromagnetic Ni disks using the phase of localized plasmons. *Phys. Rev. Lett.* **2013,** *111* (16), 167401.

114. Banthí, J. C.; Meneses-Rodríguez, D.; García, F.; González, M. U.; García-Martín, A.; Cebollada, A.; Armelles, G., High Magneto-Optical Activity and Low Optical Losses in Metal-Dielectric Au/Co/Au-SiO2 Magnetoplasmonic Nanodisks. *Adv. Mater.* **2012,** *24* (10), OP36-OP41.

115. Meneses-Rodríguez, D.; Ferreiro-Vila, E.; Prieto, P.; Anguita, J.; González, M. U.; García-Martín, J. M.; Cebollada, A.; García-Martín, A.; Armelles, G., Probing the Electromagnetic Field Distribution within a Metallic Nanodisk. *Small* **2011,** *7* (23), 3317-3323.

116. González-Díaz, J. B.; García-Martín, A.; García-Martín, J. M.; Cebollada, A.; Armelles, G.; Sepúlveda, B.; Alaverdyan, Y.; Käll, M., Plasmonic Au/Co/Au Nanosandwiches with Enhanced Magneto-optical Activity. *Small* **2008,** *4* (2), 202-205.

117. Armelles, G.; Caballero, B.; Cebollada, A.; Garcia-Martin, A.; Meneses-Rodríguez, D., Magnetic Field Modification of Optical Magnetic Dipoles. *Nano Lett.* **2015,** *15* (3), 2045-2049.

118. Liu, K.; Xue, X.; Sukhotskiy, V.; Furlani, E. P., Optical Fano Resonance in Self-Assembled Magnetic–Plasmonic Nanostructures. *J. Phys. Chem. C* **2016,** *120* (48), 27555-27561.

119. Sun, L.; Ma, T.; Yang, S.-C.; Kim, D.-K.; Lee, G.; Shi, J.; Martinez, I.; Yi, G.-R.; Shvets, G.; Li, X., Interplay Between Optical Bianisotropy and Magnetism in Plasmonic Metamolecules. *Nano Lett.* **2016,** *16* (7), 4322-4328.

120. Atmatzakis, E.; Papasimakis, N.; Fedotov, V.; Vienne, G.; Zheludev, N. I., Magneto-optical response in bimetallic metamaterials. *arXiv preprint arXiv:1603.08481* **2016**.

121. Yu Feng, H.; Luo, F.; Arenal, R.; Henrard, L.; García, F.; Armelles, G.; Cebollada, A., Active magnetoplasmonic split-ring/ring nanoantennas. *Nanoscale* **2017,** *9* (1), 37-44.

122. Sherry, L. J.; Jin, R.; Mirkin, C. A.; Schatz, G. C.; Van Duyne, R. P., Localized surface plasmon resonance spectroscopy of single silver triangular nanoprisms. *Nano Lett.* **2006,** *6* (9), 2060-2065.

123. Jin, R.; Cao, Y.; Mirkin, C. A.; Kelly, K.; Schatz, G. C.; Zheng, J., Photoinduced conversion of silver nanospheres to nanoprisms. *science* **2001,** *294* (5548), 1901-1903.

124. Ingram, W.; He, Y.; Stone, K.; Dennis, W. M.; Ye, D.; Zhao, Y., Tuning the plasmonic properties of silver nanopatterns fabricated by shadow nanosphere lithography. *Nanotechnology* **2016,** *27* (38), 385301.

125. Jensen, T. R.; Schatz, G. C.; Van Duyne, R. P., Nanosphere lithography: Surface plasmon resonance spectrum of a periodic array of silver nanoparticles by ultraviolet− visible extinction spectroscopy and electrodynamic modeling. *The Journal of Physical Chemistry B* **1999,** *103* (13), 2394-2401.

126. Creighton, J. A.; Eadon, D. G., Ultraviolet–visible absorption spectra of the colloidal metallic elements. *Journal of the Chemical Society, Faraday Transactions* **1991,** *87* (24), 3881-3891.

127. Jain, P. K.; Lee, K. S.; El-Sayed, I. H.; El-Sayed, M. A., Calculated absorption and scattering properties of gold nanoparticles of different size, shape, and composition: applications in biological imaging and biomedicine. *The journal of physical chemistry B* **2006,** *110* (14), 7238-7248.

128. Kelly, K. L.; Coronado, E.; Zhao, L. L.; Schatz, G. C., The optical properties of metal nanoparticles: the influence of size, shape, and dielectric environment. ACS Publications: 2003.

129. Huang, X.; El-Sayed, M. A., Gold nanoparticles: optical properties and implementations in cancer diagnosis and photothermal therapy. *Journal of advanced research* **2010,** *1* (1), 13-28.

130. Shaltout, A. M.; Shalaev, V. M.; Brongersma, M. L., Spatiotemporal light control with active metasurfaces. *Science* **2019,** *364* (6441), eaat3100.

131. Zhang, S.; Zhou, J.; Park, Y.-S.; Rho, J.; Singh, R.; Nam, S.; Azad, A. K.; Chen, H.-T.; Yin, X.; Taylor, A. J.; Zhang, X., Photoinduced handedness switching in terahertz chiral metamolecules. *Nature Communications* **2012,** *3*, 942.

132. Kenanakis, G.; Zhao, R.; Katsarakis, N.; Kafesaki, M.; Soukoulis, C. M.; Economou, E. N., Optically controllable THz chiral metamaterials. *Opt. Express* **2014,** *22* (10), 12149-12159.

133. Lv, T. T.; Zhu, Z.; Shi, J. H.; Guan, C. Y.; Wang, Z. P.; Cui, T. J., Optically controlled background-free terahertz switching in chiral metamaterial. *Opt. Lett.* **2014,** *39* (10), 3066-3069.

134. Kanda, N.; Konishi, K.; Kuwata-Gonokami, M., All-photoinduced terahertz optical activity. *Opt. Lett.* **2014,** *39* (11), 3274-3277.

135. Zhu, Y.; Hu, X.; Chai, Z.; Yang, H.; Gong, Q., Active control of chirality in nonlinear metamaterials. *Applied Physics Letters* **2015,** *106* (9), 091109.

136. Kan, T.; Isozaki, A.; Kanda, N.; Nemoto, N.; Konishi, K.; Takahashi, H.; Kuwata-Gonokami, M.; Matsumoto, K.; Shimoyama, I., Enantiomeric switching of chiral metamaterial for terahertz polarization modulation employing vertically deformable MEMS spirals. *Nature Communications* **2015,** *6*, 8422.

137. Wuttig, M.; Yamada, N., Phase-change materials for rewriteable data storage. *Nature Materials* **2007,** *6*, 824.

138. Liu, M.; Hwang, H. Y.; Tao, H.; Strikwerda, A. C.; Fan, K.; Keiser, G. R.; Sternbach, A. J.; West, K. G.; Kittiwatanakul, S.; Lu, J.; Wolf, S. A.; Omenetto, F. G.; Zhang, X.; Nelson, K. A.; Averitt, R. D., Terahertz-field-induced insulator-to-metal transition in vanadium dioxide metamaterial. *Nature* **2012,** *487*, 345.

139. Wang, Q.; Rogers, E. T. F.; Gholipour, B.; Wang, C.-M.; Yuan, G.; Teng, J.; Zheludev, N. I., Optically reconfigurable metasurfaces and photonic devices based on phase change materials. *Nature Photonics* **2015,** *10*, 60.

140. Yin, X.; Schäferling, M.; Michel, A.-K. U.; Tittl, A.; Wuttig, M.; Taubner, T.; Giessen, H., Active Chiral Plasmonics. *Nano Letters* **2015,** *15* (7), 4255-4260.

141. Armelles, G.; Caballero, B.; Prieto, P.; García, F.; Cebollada, A.; González, M. U.; García-Martin, A., Magnetic field modulation of chirooptical effects in magnetoplasmonic structures. *Nanoscale* **2014,** *6* (7), 3737-3741.

142. Han, B.; Gao, X.; Shi, L.; Zheng, Y.; Hou, K.; Lv, J.; Guo, J.; Zhang, W.; Tang, Z., Geometry-Modulated Magnetoplasmonic Optical Activity of Au Nanorod-Based Nanostructures. *Nano Letters* **2017,** *17* (10), 6083-6089.

143. Armelles, G.; Cebollada, A.; Feng, H. Y.; García-Martín, A.; Meneses-Rodríguez, D.; Zhao, J.; Giessen, H., Interaction Effects between Magnetic and Chiral Building Blocks: A New Route for Tunable Magneto-chiral Plasmonic Structures. *ACS Photonics* **2015,** *2* (9), 1272-1277.

144. Feng, H. Y.; Luo, F.; Arenal, R.; Henrard, L.; Garcia, F.; Armelles, G.; Cebollada, A., Active magnetoplasmonic split-ring/ring nanoantennas. *Nanoscale* **2017,** *9* (1), 37-44.

145. Ai, B.; Luong, H. M.; Zhao, Y., Chiral Nanohole Arrays. *Nanoscale* **2020,** *12* (4), 2479-2491.

146. Larsen, G. K.; He, Y.; Ingram, W.; Zhao, Y., Hidden chirality in superficially racemic patchy silver films. *Nano Lett.* **2013,** *13* (12), 6228-6232.

147. Ohno, T.; Wadell, C.; Inagaki, S.; Shi, J.; Nakamura, Y.; Matsushita, S.; Sannomiya, T., Hole-size tuning and sensing performance of hexagonal plasmonic nanohole arrays. *Opt. Mater. Express* **2016,** *6* (5), 1594-1603.

148. Van der Molen, K.; Segerink, F. B.; Van Hulst, N.; Kuipers, L., Influence of hole size on the extraordinary transmission through subwavelength hole arrays. *Appl. Phys. Lett.* **2004,** *85* (19), 4316-4318.

149. Kondratov, A.; Gorkunov, M.; Darinskii, A.; Gainutdinov, R.; Rogov, O.; Ezhov, A.; Artemov, V., Extreme optical chirality of plasmonic nanohole arrays due to chiral Fano resonance. *Phys. Rev. B* **2016,** *93* (19), 195418.

150. Wu, Z.; Zheng, Y., Moiré chiral metamaterials. *Adv. Opt. Mater.* **2017,** *5* (16), 1700034.

151. Wu, Z.; Chen, X.; Wang, M.; Dong, J.; Zheng, Y., High-performance ultrathin active chiral metamaterials. *ACS Nano* **2018,** *12* (5), 5030-5041.

152. Sobhani, A.; Knight, M. W.; Wang, Y.; Zheng, B.; King, N. S.; Brown, L. V.; Fang, Z.; Nordlander, P.; Halas, N. J., Narrowband photodetection in the near-infrared with a plasmon-induced hot electron device. *Nat. Commun.* **2013,** *4* (1), 1-6.

153. Martín-Moreno, L.; García-Vidal, F. J.; Lezec, H. J.; Pellerin, K. M.; Thio, T.; Pendry, J. B.; Ebbesen, T. W., Theory of Extraordinary Optical Transmission through Subwavelength Hole Arrays. *Phys. Rev. Lett.* **2001,** *86* (6), 1114-1117.

154. Qin, J.; Deng, L.; Kang, T.; Nie, L.; Feng, H.; Wang, H.; Yang, R.; Liang, X.; Tang, T.; Li, C., Switching the Optical Chirality in Magneto-plasmonic Metasurfaces Using Applied Magnetic Fields. *ACS Nano* **2020,** *14* (3), 2808-2816.

155. Dutta, S., A review on production, storage of hydrogen and its utilization as an energy resource. *Journal of Industrial and Engineering Chemistry* **2014,** *20* (4), 1148-1156.

156. Abdalla, A. M.; Hossain, S.; Nisfindy, O. B.; Azad, A. T.; Dawood, M.; Azad, A. K., Hydrogen production, storage, transportation and key challenges with applications: a review. *Energy conversion and management* **2018,** *165*, 602-627.

157. Buttner, W. J.; Post, M. B.; Burgess, R.; Rivkin, C., An overview of hydrogen safety sensors and requirements. *International Journal of Hydrogen Energy* **2011,** *36* (3), 2462-2470.

158. Wadell, C.; Syrenova, S.; Langhammer, C., Plasmonic hydrogen sensing with nanostructured metal hydrides. *ACS Nano* **2014,** *8* (12), 11925-11940.

159. Ramachandran, R.; Menon, R. K., An overview of industrial uses of hydrogen. *International Journal of Hydrogen Energy* **1998,** *23* (7), 593-598.

160. Hurme, E. U.; Ahvenainen, R., A nondestructive leak detection method for flexible food packages using hydrogen as a tracer gas. *Journal of food protection* **1998,** *61* (9), 1165-1169.

161. Hitchcock, C. H. S., Determination of hydrogen as a marker in irradiated frozen food. *Journal of the Science of Food and Agriculture* **2000,** *80* (1), 131-136.

162. Shin, W., Medical applications of breath hydrogen measurements. *Analytical and bioanalytical chemistry* **2014,** *406* (16), 3931-3939.

163. Chêne, J.; Martin, F., Isotopic tracing of hydrogen transport and trapping in nuclear materials. *Philosophical Transactions of the Royal Society A: Mathematical, Physical and Engineering Sciences* **2017,** *375* (2098), 20160406.

164. Barnes, D. H.; Wofsy, S. C.; Fehlau, B. P.; Gottlieb, E. W.; Elkins, J. W.; Dutton, G. S.; Novelli, P. C., Hydrogen in the atmosphere: Observations above a forest canopy in a polluted environment. *Journal of Geophysical Research: Atmospheres* **2003,** *108* (D6).

165. Nugroho, F. A.; Darmadi, I.; Cusinato, L.; Susarrey-Arce, A.; Schreuders, H.; Bannenberg, L. J.; da Silva Fanta, A. B.; Kadkhodazadeh, S.; Wagner, J. B.; Antosiewicz, T. J., Metal–polymer hybrid nanomaterials for plasmonic ultrafast hydrogen detection. *Nature materials* **2019,** *18* (5), 489.

166. Berube, V.; Radtke, G.; Dresselhaus, M.; Chen, G., Size effects on the hydrogen storage properties of nanostructured metal hydrides: A review. *International Journal of Energy Research* **2007,** *31* (6-7), 637-663.

167. Lewis, F., The Palladium Hydrogen. *System, Academic Press, London, New York* **1967**.

168. Alekseeva, S.; da Silva Fanta, A. B.; Iandolo, B.; Antosiewicz, T. J.; Nugroho, F. A. A.; Wagner, J. B.; Burrows, A.; Zhdanov, V. P.; Langhammer, C., Grain boundary mediated hydriding phase transformations in individual polycrystalline metal nanoparticles. *Nature communications* **2017,** *8* (1), 1-10.

169. Schwarz, R.; Khachaturyan, A., Thermodynamics of open two-phase systems with coherent interfaces: Application to metal–hydrogen systems. *Acta Materialia* **2006,** *54* (2), 313-323.

170. Nugroho, F. A. A.; Darmadi, I.; Zhdanov, V. P.; Langhammer, C., Universal scaling and design rules of hydrogen-induced optical properties in Pd and Pd-Alloy nanoparticles. *ACS Nano* **2018,** *12* (10), 9903-9912.

171. Jimenez, G.; Dillon, E.; Dahlmeyer, J.; Garrison, T.; Garrison, T.; Darkey, S.; Wald, K.; Kubik, J.; Paciulli, D.; Talukder, M., A comparative assessment of hydrogen embrittlement: palladium and palladium-silver (25 weight% silver) subjected to hydrogen absorption/desorption cycling. *Advances in Chemical Engineering and Science* **2016,** *6* (03), 246.

172. Yin, S.; Cheng, G.; Chang, T.-H.; Richter, G.; Zhu, Y.; Gao, H., Hydrogen embrittlement in metallic nanowires. *Nat. Commun.* **2019,** *10* (1), 1-9.

173. Xie, D.; Li, S.; Li, M.; Wang, Z.; Gumbsch, P.; Sun, J.; Ma, E.; Li, J.; Shan, Z., Hydrogenated vacancies lock dislocations in aluminium. *Nat. Commun.* **2016,** *7* (1), 1-7.

174. Gao, R.; Tu, J.; Wang, X.; Zhang, X.; Chen, C., The absorption and desorption properties of nanocrystalline Mg2Ni0. 75Cr0. 25 alloy containing TiO2 nanoparticles. *J. Alloys Compd.* **2003,** *356*, 649-653.

175. Tittl, A.; Mai, P.; Taubert, R.; Dregely, D.; Liu, N.; Giessen, H., Palladium-based plasmonic perfect absorber in the visible wavelength range and its application to hydrogen sensing. *Nano letters* **2011,** *11* (10), 4366-4369.

176. Maeda, E.; Mikuriya, S.; Endo, K.; Yamada, I.; Suda, A.; Delaunay, J.-J., Optical hydrogen detection with periodic subwavelength palladium hole arrays. *Appl. Phys. Lett.* **2009,** *95* (13), 133504.

177. Luong, H. M.; Pham, M. T.; Madhogaria, R. P.; Phan, M.-H.; Larsen, G. K.; Nguyen, T. D., Bilayer Plasmonic Nano-lattices for Tunable Hydrogen Sensing Platform. *Nano Energy* **2020,** *71*, 104558.

178. Yip, H. K.; Zhu, X.; Zhuo, X.; Jiang, R.; Yang, Z.; Wang, J., Gold Nanobipyramid-Enhanced Hydrogen Sensing with Plasmon Red Shifts Reaching≈ 140 nm at 2 vol% Hydrogen Concentration. *Advanced Optical Materials* **2017,** *5* (24), 1700740.

179. Favier, F.; Walter, E. C.; Zach, M. P.; Benter, T.; Penner, R. M., Hydrogen sensors and switches from electrodeposited palladium mesowire arrays. *Science* **2001,** *293* (5538), 2227-2231.

180. Matuschek, M.; Singh, D. P.; Jeong, H. H.; Nesterov, M.; Weiss, T.; Fischer, P.; Neubrech, F.; Liu, N., Chiral plasmonic hydrogen sensors. *Small* **2018,** *14* (7), 1702990.

181. Duan, X.; Kamin, S.; Sterl, F.; Giessen, H.; Liu, N., Hydrogen-regulated chiral nanoplasmonics. *Nano letters* **2016,** *16* (2), 1462-1466.

182. Luong, H. M.; Pham, M. T.; Guin, T.; Madhogaria, R. P.; Phan, M.-H.; Larsen, G. K.; Nguyen, T. D., Sub-second and ppm-level Optical Sensing of Hydrogen Using Templated Control of Nano-hydride Geometry and Composition. *Nat. Commun.* **2021,** *12* (1), 2414.

183. Huang, C.-H.; Hsu, H.-S.; Sun, S.-J.; Chang, Y.-Y.; Misiuna, P.; Baczewski, L. T., Extraction of magnetic circular dichroism effects from blended mixture of magnetic linear dichroism signals in the cobalt/Scotch tape system. *Sci. Rep.* **2019,** *9* (1), 1-9.

184. Albrecht, M.; Hu, G.; Guhr, I. L.; Ulbrich, T. C.; Boneberg, J.; Leiderer, P.; Schatz, G., Magnetic multilayers on nanospheres. *Nature Materials* **2005,** *4* (3), 203-206.

185. Streubel, R.; Fischer, P.; Kronast, F.; Kravchuk, V. P.; Sheka, D. D.; Gaididei, Y.; Schmidt, O. G.; Makarov, D., Magnetism in curved geometries. *J. Phys. D: Appl. Phys.* **2016,** *49* (36), 363001.

186. Chang, P.-C.; Liu, C.-M.; Hsu, C.-C.; Lin, W.-C., Hydrogen-mediated magnetic domain formation and domain wall motion in Co 30 Pd 70 alloy films. *Sci. Rep.* **2018,** *8* (1), 6656.

187. Akamaru, S.; Matsumoto, T.; Hara, M.; Nishimura, K.; Nunomura, N.; Matsuyama, M., Magnetic susceptibility of the pd–co–h system. *J. Alloys Compd.* **2013,** *580*, S102-S104.

188. Wang, D.; Lee, K.-Y.; Luo, S.; Flanagan, T. B., The thermodynamics of hydrogen absorption/desorption by pd–co alloys. *J. Alloys Compd.* **1997,** *252* (1-2), 209-218.

189. Darmadi, I.; Nugroho, F. A. A.; Kadkhodazadeh, S.; Wagner, J. B.; Langhammer, C., Rationally-Designed PdAuCu Ternary Alloy Nanoparticles for Intrinsically Deactivation-Resistant Ultrafast Plasmonic Hydrogen Sensing. *ACS sensors* **2019,** *4* (5), 1424-1432.

190. Bradley, L.; Ye, D.; Luong, H. M.; Zhao, Y., Transition from discrete patches to plasmonic nanohole array by glancing angle deposition on nanosphere monolayers. *Nanotechnology* **2020,** *31* (20), 205301.

191. Darmadi, I.; Nugroho, F. A. A.; Langhammer, C., High-Performance Nanostructured Palladium-Based Hydrogen Sensors—Current Limitations and Strategies for Their Mitigation. *ACS sensors* **2020**.

192. Energy Efficiency and Renewable Energy (EERE), F. C. T. O., Multi-Year Research, Development, and Demonstration Plan, 2011–2020. Section 3.7 Hydrogen Safety, Codes and Standards;. Energy, U. S. D. o., Ed. 2015.

193. Bannenberg, L.; Schreuders, H.; Dam, B., Tantalum-Palladium: Hysteresis-Free Optical Hydrogen Sensor Over 7 Orders of Magnitude in Pressure with Sub-Second Response. *Advanced Functional Materials* **2021**.

194. Oh, J. R.; Moon, J. H.; Yoon, S.; Park, C. R.; Do, Y. R., Fabrication of wafer-scale polystyrene photonic crystal multilayers via the layer-by-layer scooping transfer technique. *J. Mater. Chem.* **2011,** *21* (37), 14167-14172.

195. Ngene, P.; Westerwaal, R. J.; Sachdeva, S.; Haije, W.; de Smet, L. C.; Dam, B., Polymer-Induced Surface Modifications of Pd-based Thin Films Leading to Improved Kinetics in Hydrogen Sensing and Energy Storage Applications. *Angewandte Chemie* **2014,** *126* (45), 12277-12281.

196. Koo, W.-T.; Qiao, S.; Ogata, A. F.; Jha, G.; Jang, J.-S.; Chen, V. T.; Kim, I.-D.; Penner, R. M., Accelerating palladium nanowire H2 sensors using engineered nanofiltration. *ACS Nano* **2017,** *11* (9), 9276-9285.

197. Li, G.; Kobayashi, H.; Taylor, J. M.; Ikeda, R.; Kubota, Y.; Kato, K.; Takata, M.; Yamamoto, T.; Toh, S.; Matsumura, S., Hydrogen storage in Pd nanocrystals covered with a metal–organic framework. *Nature materials* **2014,** *13* (8), 802-806.

198. Pinnau, I.; Toy, L. G., Gas and vapor transport properties of amorphous perfluorinated copolymer membranes based on 2, 2-bistrifluoromethyl-4, 5-difluoro-1, 3-dioxole/tetrafluoroethylene. *Journal of Membrane Science* **1996,** *109* (1), 125-133.

199. O'Brien, M.; Baxendale, I. R.; Ley, S. V., Flow ozonolysis using a semipermeable Teflon AF-2400 membrane to effect gas– liquid contact. *Organic letters* **2010,** *12* (7), 1596-1598.

200. Hong, J.; Lee, S.; Seo, J.; Pyo, S.; Kim, J.; Lee, T., A highly sensitive hydrogen sensor with gas selectivity using a PMMA membrane-coated Pd nanoparticle/single-layer graphene hybrid. *ACS Appl. Mater. Interfaces* **2015,** *7* (6), 3554-3561.

201. Min, K.; Paul, D., Effect of tacticity on permeation properties of poly (methyl methacrylate). *Journal of Polymer Science Part B: Polymer Physics* **1988,** *26* (5), 1021-1033.

202. ISO, ISO 26142:2010. Hydrogen detection apparatus - Stationary applications. **2010**.

203. Palm, K. J.; Murray, J. B.; Narayan, T. C.; Munday, J. N., Dynamic optical properties of metal hydrides. *ACS Photonics* **2018,** *5* (11), 4677-4686.

204. Larsen, G. K.; He, Y.; Wang, J.; Zhao, Y., Scalable fabrication of composite Ti/Ag plasmonic helices: controlling morphology and optical activity by tailoring material properties. *Adv. Opt. Mater.* **2014,** *2* (3), 245-249.

205. He, Y.; Larsen, G. K.; Ingram, W.; Zhao, Y., Tunable three-dimensional helically stacked plasmonic layers on nanosphere monolayers. *Nano Lett.* **2014,** *14* (4), 1976-1981.

APPENDIX A

Optical and Magneto-optical Constant of Ag-Co Composite Materials

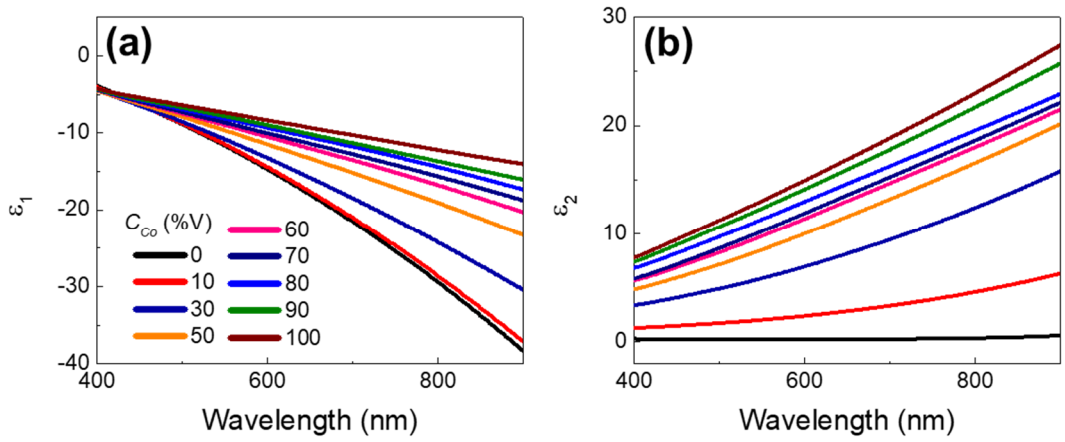

Appendix Figure A1. (a) Real part (ε_1) and (b) imaginary part (ε_2) of optical permittivity of Ag-Co composite thin films with different C_{Co} (%), determined by a spectroscopic ellipsometer.

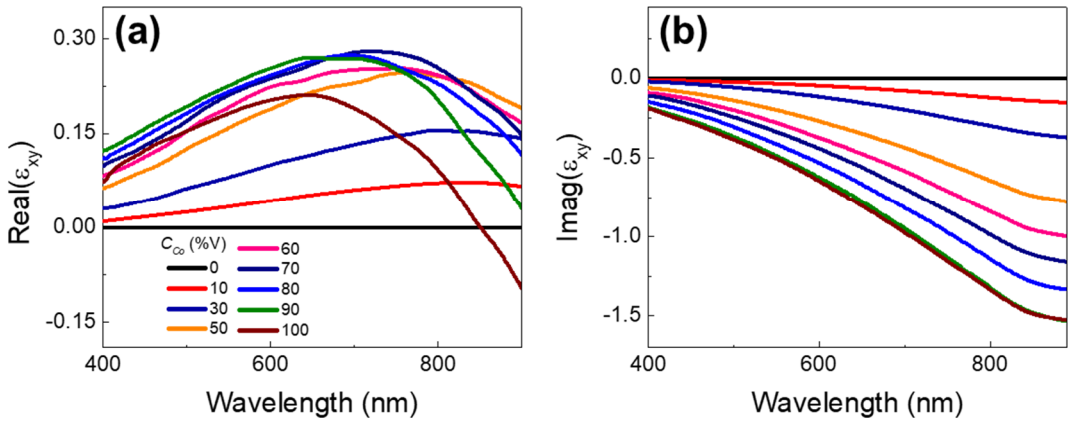

Appendix Figure A2. (a) Real part and (b) imaginary part of the off-diagonal component (ε_{xy}) of optical permittivity tensor, measured with Ag-Co composite thin films with different C_{Co} (%) by a Faraday effect spectroscopy.

APPENDIX B

Magneto-optical Properties of PdCo Thin Films

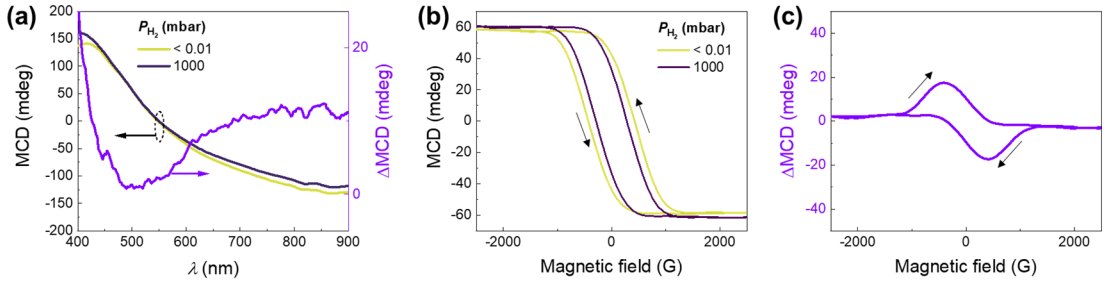

Appendix Figure B1. (a) MCD spectra $MCD_{1000\ mbar}$ and $MCD_{0\ mbar}$ of control PdCo thin film sample, measured at P_{H_2} = 1000 mbar and <0.01 mbar, respectively, and $\Delta MCD = MCD_{1000\ mbar} - MCD_{0\ mbar}$. (b) MCD hysteresis loops control PdCo thin film sample at λ = 450 nm, measured under several H_2 pressures and vacuum (before and after exposed to H_2). Arrows denote the magnetization direction. (c) ΔMCD hysteresis loop shows maxima changes of MCD. Black arrows denote the magnetization direction.

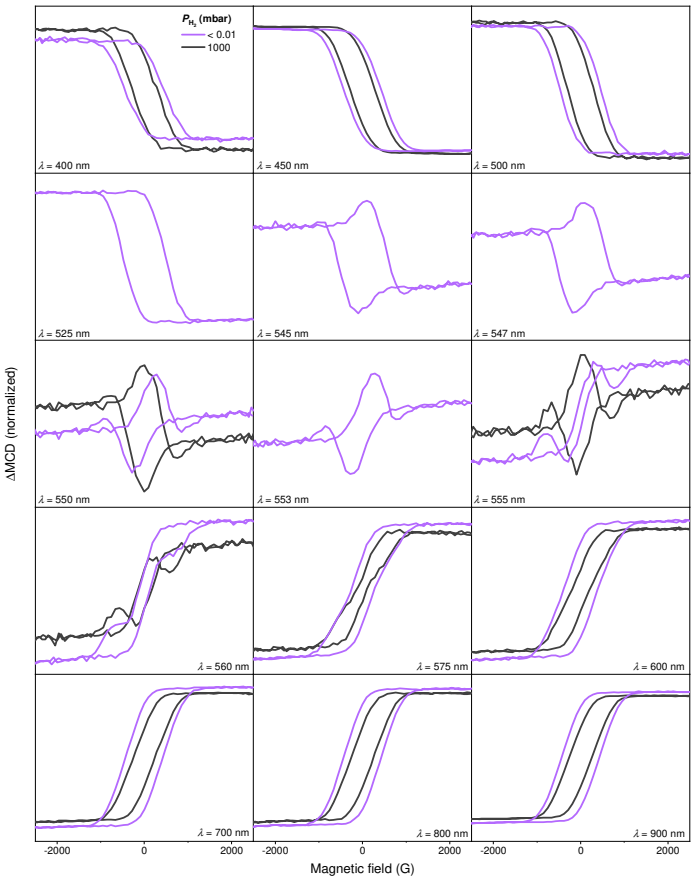

Appendix Figure B2. MCD hysteresis loops control PdCo thin film sample at different wavelength λ, measured at P_{H_2} = 1000 mbar and < 0.01 mbar.